Università degli Studi di Roma "La Sapienza"
Facoltà di Scienze Matematiche, Fisiche e Naturali
Dipartimento di Fisica

Measurement of relative branching fractions for D^0 meson Cabibbo suppressed hadronic decays, from the CDF secondary vertex trigger sample at the Tevatron collider.

Dottorato di Ricerca in Fisica, *XV ciclo*
Ph.D. in Physics

Author:
Sandro De Cecco

Tutor:
Prof. Carlo Dionisi

January 2003

Contents

Introduction **5**

1 Heavy Flavours production in $p\bar{p}$ at $\sqrt{s} = 2$ TeV **11**

1.1 General $p\bar{p}$ interactions 11

1.2 HF production processes 15

2 Beauty and Charm physics at CDF in runII **21**

2.1 CPV in the Standard Model 21

2.2 $B_s - \bar{B}_s$ system oscillations 24

2.3 Mixing and CP violation in Charm sector 29

2.3.1 $D^0 - \bar{D}^0$ mixing 29

2.3.2 CP violation 31

3 The CDF detector at Tevatron **33**

3.1 The Tevatron $p\bar{p}$ collider 33

3.2 CDF overview 38

3.3 Silicon Vertex Detector 40

3.4 The drift chamber, COT 41

3.5 Time of Flight, TOF 41

3.6 Calorimetry 42

3.7 Muon detectors 43

3.8 Trigger and DAQ system 44

3.8.1 Level 1 47

3.8.2 Level 2 47
3.8.3 Level 3 48

4 Silicon Vertex Tracker, a dedicated HF trigger 49

4.1 Introduction 49
4.2 Working principles 50
4.3 SVT commissioning 52
4.4 Two track hadronic trigger 57

5 Particle identification and flavour tagging at CDF 61

5.1 dE/dx from the drift chamber 61
5.2 The Time Of Flight detector 63
5.3 TOF calibration 66
5.4 TOF resolution 70
5.5 Perspectives for flavour tagging 72

6 Heavy mesons reconstruction in the SVT trigger sample 77

6.1 Introduction 77
6.2 Montecarlo studies 78
6.2.1 Generators 79
6.2.2 A generator level trigger simulation 80
6.2.3 Optimization of D^0 selection 84
6.3 First $D^0 \to K\pi$ signal from SVT 95
6.3.1 Beam line determination 96
6.3.2 Tracking quality checks 97
6.3.3 Data selection and first results 99
6.4 Charmed mesons $D^{*\pm}, D^{\pm}, D_s^{\pm}$ 104
6.5 SVT sample $b\bar{b}/c\bar{c}$ composition 108
6.6 Observation of $B^{\pm} \to \bar{D}^0(D^0)\pi^{\pm}$ 112
6.7 Summary 115

7 Measurement of the Relative Branching Fractions $\Gamma(D^\circ \to K^+K^-)/\Gamma(D^\circ \to K\pi)$ and $\Gamma(D^\circ \to \pi^+\pi^-)/\Gamma(D^\circ \to K\pi)$ 117

7.1 Introduction 117

7.2 Relative collection efficiencies 118

7.2.1 GenTrig parametric simulation studies 118

7.2.2 A full Geant simulation 122

7.2.3 Validation of the `svtsim` simulation 124

7.2.4 Relative acceptance determination with `svtsim` 127

7.2.5 Effect of decay in flight and hadronic interaction 129

7.3 The data sample 132

7.4 Signal reconstruction 132

7.4.1 Effect of K–π swap in the $D^\circ \to K\pi$ peak 135

7.4.2 Signal extraction and background estimates 139

7.4.3 Results 144

7.5 Systematics 146

7.5.1 Background fitting functions 146

7.5.2 Autoreflection model 147

7.5.3 Lifetime difference and DCS decays 149

7.5.4 Relative acceptance correction 150

7.5.5 Production model 151

7.5.6 Tracking 152

7.5.7 Systematics Summary 153

7.6 Summary 153

8 Perspectives for HF physics and CPV in the hadronic sample 155

8.1 Introduction 155

8.2 CDF charm physics potential 157

8.2.1 Charm yields 158

8.2.2 Limits in charm physics for CDF 160
8.3 $D^0 - \bar{D}^0$ mixing 161
8.3.1 Mixing through lifetime difference 162
8.4 CP violation in $D^0 \to hh$ decays 163
8.5 B_s^0 oscillations, Δm_s 166
8.6 $B_d, B_s \to hh$ decays 170

Conclusions **173**

Bibliography **175**

Introduction

The Tevatron collider and the CDF experiment underwent significant upgrades for the Run II data-tacking period which has started at the end of year 2001 and will continue in the next years. Before the beginning of Large Hadronic Collider era, the $p\bar{p}$ collisions at $\sqrt{s} = 1.96$ TeV produced at the Tevatron, will constitute the most promising place in which to perform measurements regarding a very large number of sectors in particle physics. Among them, the research of CP symmetry violation in heavy flavours is certainly one of the most prominent. The main objective is to test the Standard Model consistency through all possible constraints coming from CP violating observables. This is at present extensively pursued by the new generation experiments at the e^+e^- B factories.

In the Run I, with the measure of $sin2\beta$, CDF demonstrated how hadronic collider experiments can perform very high precision measurement like CP violation in the B mesons, traditionally considered possible only at e^+e^- machines. The CDF experiment implemented for Run II, strategic detector and trigger upgrades, in order to be competitive and complementary to the B factories on CP violation in beauty and charm sectors. The most important of this upgrades is the new CDF trigger device Silicon Vertex Tracker SVT which has been designed to do an on-line selection of long lived particles like B or D mesons, through a fast and high resolution tracking, allowing to select events in which there are tracks coming from vertices which are displaced from the nominal interaction point. This device makes possible to reduce the high QCD background to heavy flavour, typical of an hadronic environment, without explicitly requiring a lepton in the final state, thus allowing

to trigger directly on low BR fully hadronic decays of B and D mesons. This opens the way to high precision measurements on completely reconstructed heavy mesons decays. As an example, in the measurement of the B_s mixing frequency Δm_s, having a large sample of these decays will allow high precision proper time resolution.

Another important CDF upgrade is the new Time-of-Flight detector which will rise the particle identification capabilities, especially relevant in B flavour tagging for CP violation studies.

My thesis work, started on november 2000. I joined the CDF experiment which was at the time in the early phase of detector commissioning for Run II. The two main items on which I got involved are: the reconstruction of hadronic final states of heavy mesons in the new **SVT trigger sample**, and, the **Time-of-Flight** detector.

Both this items are main research lines of the CDF Roma group, in which I worked for the PhD. As already underlined, the SVT sample constitutes the most promising sample for HF physics. In this perspective, in the year 2001, my work focused on the reconstruction, in this sample, of fully hadronic heavy mesons final states, in the framework of the CDF collaboration B physics group. The guide-line idea was to operate an optimized selection analysis of charmed mesons D^0, D^*, D^+, D_s in order to have a sample enriched in charm, to be used as a general first step of all the analysis concerning $B \to D+X$. This was thought to be possible after optimization studies for the selection of D^0 meson operated on a Montecarlo sample of $b\bar{b}$ events which passing the SVT trigger requirements. Results and details are presented in chapter 6, a very clean selection of D mesons among generic $b\bar{b}$ event is possible thus allowing $B \to D + X$ physics sample extraction.

Pushed by this Montecarlo studies, a "D reconstruction" sub-group of CDF B physics group was created in spring 2001. In the framework of this sub-group, first HF signal on SVT data in november 2001 was seen in the $D^0 \to K\pi$ channel, see section 6.3. From the study of the first data, detector performances and reconstruction algorithms were extensively commissioned; as a by-product new silicon alignments and optimization of tracking code were given as general interest informations to the

collaboration. D mesons signals extracted from SVT data are of primary interest in the SVT trigger operation optimization and in the SVT trigger simulation validation. Examples of this relevance are given in the SVT simulation based studies, preliminary to the measurement presented in chapter 7.

Given the large yield of D mesons in the SVT sample, in particular $D^0 \to K\pi$ decay selection, is used now as an off-line monitor for reconstruction code versions validation in terms of tracking resolution and efficiency parameters, and as an on-line SVT trigger physics monitor, to understand quality of acquired data and/or trigger pathologies through the changes in D mesons trigger cross sections.

The reconstruction software developed for previous Montecarlo studies and for data analysis, with some generalization, has become an official CDF hadronic reconstruction package named **"CharmMods"** which is a general tool for HF decays analysis in the collaboration.

The optimization of tracking reconstruction obtained with D mesons analysis from the SVT trigger sample, lead the D-sub-group to become the general hadronic HF channels reconstruction group in CDF B physics group. First evidences of B mesons decays selected by SVT in the early CDF Run II data are shown in section 6.6, the signal extraction has been possible as a consequence of the detector knowledge acquired in the D mesons studies.

CDF collected useful physics data from january 2002. Results and analysis presented this thesis are based on data collected till may 2002 with SVT trigger, corresponding to an integrated Luminosity of around 10 pb^{-1}.

The work on D mesons presented in this thesis, after some general reconstruction analysis given in chapter 6, focus on two-body decays of D^0 meson in the $K\pi$, KK, $\pi\pi$ final states. Two-body HF decays topology are "golden channels" for the hadronic two track trigger SVT, since both particle tracks in the final state are SVT trigger tracks, resulting in a simple definition of trigger and detector collection efficiencies. I present in chapter 7 the measurement of the branching fractions of the Cabibbo suppressed modes $D^0 \to KK, \pi\pi$ relative to the allowed mode $D^0 \to K\pi$.

In only 10 pb^{-1} of data collected by CDF SVT trigger, around 2,000 $D^0 \rightarrow \pi\pi$, 5,000 $D^0 \rightarrow KK$ and 56,000 $D^0 \rightarrow K\pi$ were reconstructed. A relative BR measurement was performed given the uncertainties on HF production cross sections at $p\bar{p}$ interactions, thus resulting in an intrinsic limit on measuring high precision absolute BR at hadron colliders.

The results for this relative widths, given at the end of chapter 7, are already competitive with the best single measure obtained with a similar technique at the Y_{4S} with $\approx$ 10 fb^{-1} integrated luminosity by the CLEO experiment [50]. In the widths ratio many systematic effects cancels, while higher order correction are taken into account as well their systematic uncertainties. The preliminary results shows up to be already systematic dominated. Some systematic effects are for the time being estimated in a conservative way, further studies will make possible to enhance the precision of the measurement.

The reconstruction and study of KK and $\pi\pi$ CP even eigenstates modes of D^0 meson, is the starting point for promising measurements on charm physics. In particular, $D^0 - \bar{D}^0$ mixing and direct CP violation in D^0 decays topics are discussed from a theoretical point of view in section 2.3, while in conclusive chapter perspectives for this measurements at CDF are given in sections 8.3, 8.4. This measurement has been one of the preliminary physics results, based on the data collected in this early phase of Run II, that has been presented by the CDF collaboration at the summer 2002 conferences. The study of CP violation in the charm sector has become a major goal for the CDF collaboration as a consequence of very encouraging experimental results presented here.

The analysis of B mesons decays in charmed mesons like the $B_s \rightarrow D_s\pi$ with all hadronic final states, and, two light hadrons decays like $B \rightarrow hh$, are the other main issue tightly connected from the experimental point of view with the work presented in this thesis.

Highlights on Δm_s impact on CKM picture of CP violation is given in chapter 2 and the perspectives in its measurement at CDF through fully reconstructed

hadronic decays from SVT trigger, are given in section 8.5. The tight connection from the trigger and reconstruction point of views, of the D^0 mesons decays studies with the analysis of $B_{d,s} \to \pi\pi, K\pi, KK$, is detailed in section 8.6.

On the other main item on which my thesis work consisted, i.e. the **Time-of-Flight** detector, a "state of the art" chapter is dedicated (chapter 5), brief description of the new flavour tagging techniques now possible with the TOF particle identification is then given.

My work on the TOF detector consisted mainly in the responsibility in the development of an analysis oriented "off-line monitor" of TOF performances. TOF measurement is based on scintillator bars timing hits and on tracking system information, it is thus possible after event reconstruction. The monitoring, which has been developed in the framework of the CDF TOF sub-detector group, is a useful instrument in the validation of TOF reconstruction algorithms and performance control. In particular the control of TOF occupancy and efficiency, on which I am working, are part of the parameters that influence the final TOF performances.

Thesis is structured as follows:

- **Chapter 1**: Heavy flavour production at $p\bar{p}$ interaction is qualitatively discussed, together with general remarks on the issues regarding HF physics at hadron colliders.

- **Chapter 2**: Selection of topics on CP violation in charm and beauty sectors is discussed. CP violation in charmed mesons and B_s meson mixing are chosen as explained above in connection to the analysis presented in this thesis.

- **Chapter 3**: Description of the CDF detector and the Tevatron accelerator complex.

- **Chapter 4**: Silicon Vertex Tracker. Detailed description of the working principles and first performances of the CDF hadronic track trigger.

- **Chapter 5**: The CDF Time-of-Flight detector calibration and reconstruction as well as very preliminary performances in terms of particle identification are given.

- **Chapter 6**: General introductory studies on heavy mesons reconstruction based on both Montecarlo and data are reported, as well as the results of some charmed mesons decay modes extraction from the SVT trigger sample.

- **Chapter 7**: The measurement of the widths of Cabibbo suppressed D^0 decays to KK and $\pi\pi$ relative to the allowed mode $D^0 \to K\pi$ in the 2002 CDF data from SVT trigger. The analysis step are presented together with the description of the SVT trigger simulation tool that has been used and validated in this analysis. Systematic error sources studies are reported as well as results.

- **Chapter 8**: Based on the analysis presented in previous chapters, a glimpse to the CDF potential in charm physics is given in terms of prospected yields. In particular prospects and analysis strategies for D^0 mixing and direct CP violation in D^0 decays are discussed. Perspectives for B_s mixing and $B \to hh$ decays are then given together with their experimental connections to the charm analysis.

Chapter 1

Heavy Flavours production in $p\bar{p}$ at $\sqrt{s} = 2$ TeV

1.1 General $p\bar{p}$ interactions

We will recall here some basis of heavy flavour production at $p\bar{p}$ interactions, in the perspective of introducing both the hadronic collider environment and the experimental issues which characterize HF physics at CDF. Many of these issues apply to both beauty and charm physics and will be briefly discussed in this chapter

During Run II, the Fermilab Tevatron will collide proton p and anti- proton $\bar{p}$ beams at a center-of-mass energy of 1.96 TeV. Some other design parameters of the Tevatron for Run II are summarized in section 3.1.

In rough terms there are three processes which take place at this energy and which are important for the design of a B physics experiment. These are the production of $b\bar{b}$ pairs, the production of $c\bar{c}$ pairs and all of the light quark and gluon processes which contribute to the background; the cross-sections for these processes are respectively of the order of $\simeq 0.1$ mb, $\simeq 1$ mb and $\simeq 75$ mb. There are no known processes which produce a single b or a single $\bar{b}$ at a significant rate, only processes which produce pairs. Similarly for charm production.

In $p\bar{p}$ interactions there are, of course, many other interesting processes which occur, including W, Z, $t\bar{t}$ and single *top* production. Moreover new particle searches like Higgs boson and Supersymmetric particles are among the main topics for hadron colliders. The cross-sections for these processes, however, are small enough that they

do not contribute to the background to HF physics at the Tevatron.

After a $b\bar{b}$ pair is produced, it hadronizes to form pairs of b hadrons including B mesons, such as B_d, B_u, B_s, B_c, and b baryons such as Λ_b, Ω_b, etc. All of these states decay weakly, with a significant lifetime and, therefore, with a significant decay length. Excited states of these b hadrons are also produced, all of which decay strongly or electromagnetically to one of the weakly decaying b hadrons. A similar picture exists for the hadronization of $c\bar{c}$ pairs into hadrons. Therefore the route to all of b and c physics goes through the weakly decaying states. One shorthand which will be used in the following is that: $\sigma_{BG} = \sigma_{tot} - \sigma_{b\bar{b}} - \sigma_{c\bar{c}}$ which stands for the "background" cross-section; that is for the total hadronic cross-section with the $c\bar{c}$ and $b\bar{b}$ pieces excluded. The $c\bar{c}$ piece is treated separately because it is interesting to study in its own and also because it has a few critical properties which are more like b's than like background. At our current level of knowledge, $\sigma_{BG} \simeq \sigma_{tot} \simeq 75mb$ [1] at 1.96 TeV. This includes elastic $p\bar{p}$ scattering, diffractive scattering and inelastic scattering.

In the following, the z axis is defined to lie along the beam direction and quantities such as p_T are measured with respect to this axis. The variable Φ is the azimuthal angle around the z axis and θ is the polar angle relative to the z axis as well.

As recalled above the cross-section for b production is about 1.5 parts in 1000 of the total cross-section. Moreover, many of the B physics processes of interest have product of branching fractions of $O(10^{-6})$ or smaller. Therefore one is often looking for signals of a few parts per million of the total cross-section.

The signature which allows one to see B physics is given by the lifetime of the b quark. The B_d ,B_u and B_s mesons each have a lifetime τ of approximately 1.5 ps, or $c\tau = 450\mu$m. When the momentum spectrum of the B mesons is folded in, the mean decay length of all produced B mesons is of the order of a few mm. Therefore almost all B mesons decay inside the beam pipe. The resolution on the decay length varies from one decay mode to another and depends on the detector

tracking resolution. Typical values fall in the range of 50 μm to 100 μm; therefore the B decay vertices will be well resolved and will be readily separated from the $p\bar{p}$ primary interaction vertex (PV). The B_c, the weakly decaying b baryons and the weakly decaying charmed hadrons have somewhat shorter lifetimes, but most of them have a long enough lifetime that their decay vertices will also be well separated from PV.

The background processes, with their much larger cross-sections, do not produce particles which have this type of decay length signature. This brings us an important lever arm which is the presence of distinct secondary vertices allowing to extract the b and c signals from the background.

About 85 % of all weakly decaying b hadrons decay into one charmed hadron plus long lived particles. Long lived particles include pions, kaons, protons, photons, charged leptons and neutrinos, all of which are stable enough to leave tracks or energy deposit or missing energy in the detector. About 15 % of weakly decaying b hadrons decay into 2 charmed hadrons, plus long lived particles; the decay $B^0 \to D^{*+}D^{*-}$ is an example. And about 1 % of b hadrons decay into only long lived particles; the decay $B^0 \to \pi^+\pi^-$ is an example.

Therefore a typical $b\bar{b}$ event has 5 distinct vertices, all inside the beam pipe: the primary $p\bar{p}$ interaction vertex, the two secondary B decay vertices and the two tertiary c decay vertices. On the other hand, many of the most interesting decays involve charmless decays of the b and a typical event containing one of these decays has 4 vertices: the primary $p\bar{p}$ vertex, the vertex from the signal charmless b, and the b and c vertices from the other b (or $\bar{b}$) produced in the $p\bar{p}$ interaction. Similarly, a typical $c\bar{c}$ interaction has three distinct vertices inside the beam pipe: the primary vertex plus two secondary vertices, which come from the decay of the two charmed hadrons.

To be complete, one more detail must be added to the description of typical $b\bar{b}$ events. For the running conditions projected for Run II, each beam crossing will contain in mean around one interaction. At higher Luminosities, beyond the

Run II, several background interactions which contain no $b\bar{b}$ or $c\bar{c}$ pairs will be superimposed to the HF production. At present running conditions in each Tevatron bunch crossing we have a mean number of interaction which is less than 1, thus for the moment, multiple interaction in a single event is not an issue, see section 3.1 for details.

In an event containing a $b\bar{b}$ or a $c\bar{c}$ pair, the stable daughters of the b and c hadrons usually have a large impact parameter with respect to the primary vertex. Because the beam spot is very narrow in the transverse plane (R, ϕ), roughly 30 μm in diameter, these tracks will also have a larger transverse plane impact parameter with respect to the beam line. A track is considered detached if the impact parameter, divided by its error, is significant; this definition is used both for 2D and 3D impact parameters.

A powerful trigger can be made by looking for the presence of a few detached tracks. CDF have designed dedicated trigger SVT (Silicon Vertex trigger) which make an on-line detachment requirement by measuring impact parameters of tracks and cutting on them. The on-line impact parameter measure is made possible by a dedicated hardware setup which uses silicon vertex detector information in an extremely fast way, details are given in chapter 4. In addition to track impact parameter, there are other properties which can be used to identify events which contain b quarks. For example, selecting events with one or two leptons of p_T in the range between 1 and $\sim$ 20 GeV is an excellent way to select events containing $b\bar{b}$ pairs while rejecting background events. This has been the "typical" B physics trigger in all hadronic collider experiments up to now. For Run II and beyond, with SVT trigger, CDF will select all hadronic final states, this is certainly one of the major advances since Run I for HF physics.

Because of their topological similarities to $b\bar{b}$ events, $c\bar{c}$ events will also pass SVT trigger requirements. Charm events, however, have properties which are intermediate between the b events and the background events: their decay lengths are shorter, their impact parameters smaller and their stable daughters have a softer momentum

spectrum. Therefore the cuts which reduce the background to an acceptable level are much less efficient for $c\bar{c}$ events than they are for $b\bar{b}$ events. Nevertheless the size of the $c\bar{c}$ cross section, which is foreseen to be order of magnitudes bigger than the $b\bar{b}$ one, will show up in an high number of $c\bar{c}$ events selected by the SVT hadronic track trigger. Preliminary measurement of SVT sample composition in terms of $b\bar{b}$ and $c\bar{c}$ will be discussed in section 6.5.

1.2 HF production processes

At a $p\bar{p}$ collider, it is usually most convenient to describe particle production in terms of three variables, p_T , ϕ and y, where p_T is the transverse momentum of the particle with respect to the beam line which is along the z axis, ϕ is the azimuth around the beam line and where the rapidity y is a measure of the polar angle θ relative to the beam line, defined as:

$$y = \frac{1}{2} ln(\frac{E + P_z}{E - P_z}) \tag{1.1}$$

For historical reasons people sometimes work in units of pseudo-rapidity η instead of y, with:

$$\eta = -ln(tan\theta/2) \tag{1.2}$$

For mass-less particles $\eta = y$ and for highly relativistic particles η approaches y. The b production as a function of η is approximately flat in the central region, falling off symmetrically at large $|\eta|$, this is a general feature of particle production in hadronic collisions. During Tevatron Run I, both CDF and D0 studied the production of b quarks in $p\bar{p}$ collisions at a center-of-mass energy of 1.8 TeV. Both CDF and D0 have studied the central rapidity region $|\eta| < 1$ and D0 has also studied the forward region, $2.4 < y < 3.2$. Both CDF and D0 find that the $b\bar{b}$ production cross-section in the central region is underestimated by the Mangano, Nason and Ridolfi (MNR) Next-to-Leading Order QCD calculation [2] by a factor of more than two.

A property of $b\bar{b}$ production is that the cross section is concentrated in the central region and the forward going B mesons have much higher momentum than

those produced in the central region. This implies that forward B mesons have longer decay lengths. Another important property is the strong azimuthal angle correlation between b and $\bar{b}$ which are more likely to be produced back to back in azimuth, the shape of this correlation is well reproduced by the MNR model.

While the production of $b\bar{b}$ pairs is well described by perturbative QCD and by the knowledge of the structure functions of the proton, at the contrary, the hadronization, or the fragmentation, of these quarks into the final state hadrons is described by models. These models are usually realized via computer codes for event generators, the most commonly used being PYTHIA [3] and HERWIG [4]. One of the properties which must be input to the event generators is the fraction f of time that the b quark fragments into each of the allowed hadrons, B_{uds} or one of the b baryons. A recent measurement from CDF [5] gives, $f_u : f_d : f_s : f_{barions} = 0.375 \pm 0.023 : 0.375 \pm 0.023 : 0.160 \pm 0.044 : 0.090 \pm 0.029$, with the assumption that $f_u = f_d$. It is generally presumed that, except for threshold effects, the fragmentation process is independent of the production process and is roughly independent of energy. For comparison the same production fractions measured at LEP and SLD are (average values) [6]: $0 : 401 \pm 0.010 : 0 : 401 \pm 0.010 : 0.100 \pm 0.012 : 0.099 \pm 0.017$. In both of these measurements, the production of B_c mesons is too small to be significant. In the standard event generators the choice of hadron species for the b quark is independent of the choice of hadron species for the $\bar{b}$ quark. This cannot be exactly true since there is presumably some production via the $Y(4s)$ resonance, which decays only to coherent states like $B^0\bar{B}^0$ or $B^+\bar{B}^-$. If there is enough resonant production to affect the physics results, the amount of such production can be easily measured with the Run II data.

Let now briefly discuss the principal processes responsible for $b\bar{b}$ (and $c\bar{c}$) production in $p\bar{p}$ interaction, that are essentially three:

- **"Flavour Creation"**, production of a $b\bar{b}$ pair by gluon fusion or by the annihilation of light quarks via the two 2-to-2 parton sub-processes, $q + \bar{q} \rightarrow b + \bar{b}$, and $g + g \rightarrow b + \bar{b}$.

- **"Flavour Excitation"**, comes from the scattering of a b or a $\bar{b}$ quark out of the initial-state into the final-state by a gluon or by a light quark (or anti-quark) via the sub-processes: $g + b(\bar{b}) \rightarrow g + b(\bar{b})$ or $q(\bar{q}) + b(\bar{b}) \rightarrow q(\bar{q}) + b(\bar{b})$

- **"Parton Shower/Fragmentation"**, $b\bar{b}$ pair is in the final state but no heavy quarks participates the initial state interaction which is governed by light quarks and gluons. This category includes the **"Gluon Splitting"** sub-process $g + g \rightarrow g + g(g \rightarrow b\bar{b})$.

Correlations between the b and $\bar{b}$ quark are very different for the three sources and thus are a possible way to isolate the individual processes contributions.

The Leading-log Order QCD hard scattering Monte-Carlo models of HERWIG, ISAJET, and PYTHIA have been used to study the sources of b-quarks at the Tevatron [7]. The leading-log QCD Monte-Carlo model predictions have been compared with data on the b quark inclusive cross section at the Tevatron.

The production of a $b\bar{b}$ pair via **"Flavour Creation"** gluon fusion or annihilation of light quarks is easy to generate and all three QCD Monte-Carlo models (with the same structure functions) predict roughly the same cross section and similar b, $\bar{b}$ correlations from these terms. At the Tevatron all three Monte-Carlo models predict that the flavour creation contribution to b quark production is less than 35 % of the overall inclusive b quark production rate from all three sources.

The source of b quarks resulting from the scattering of a b quark or $\bar{b}$ out of the initial state into the final state by a gluon or by a light quark(anti-quark) is difficult to generate and depends sensitively on the parton distribution functions. The QCD Monte-Carlo model predictions differ somewhat, however, it seems likely that at the Tevatron the **"Flavour Excitation"** contribution to the inclusive b quark cross section is comparable to or greater than the contribution from Flavour creation.

The b, $\bar{b}$ correlations resulting from the Flavour excitation term are much different than those arising from Flavour creation. In particular, the distribution in the azimuthal angle $\Delta\phi$ between the b and the $\bar{b}$ quark peaks sharply in the "backward"

($|\Delta\phi| > 90$) region for Flavour creation, while Flavour excitation produces an approximately flat $|\Delta\phi|$ distribution as can be seen in figure 1.1. Also, the Flavour excitation terms have, on the average, a large transverse momentum asymmetry between the b and $\bar{b}$ quark, while the Flavour creation terms produce no p_T asymmetry.

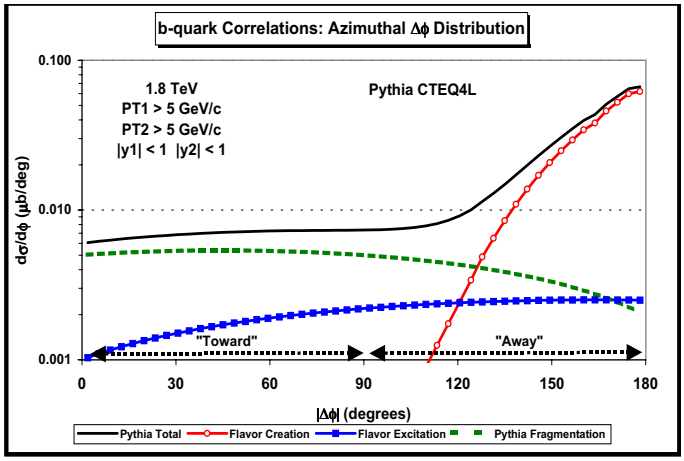

Figure 1.1: Predictions of PYTHIA 6.158 (CTEQ4L, $p_T(hard) > 0$) for the azimuthal angle $\Delta\Phi$ between a b-quark and a $\bar{b}$-quark in proton-antiproton collisions at 1.8 TeV [7]. The curves correspond to the three processes.

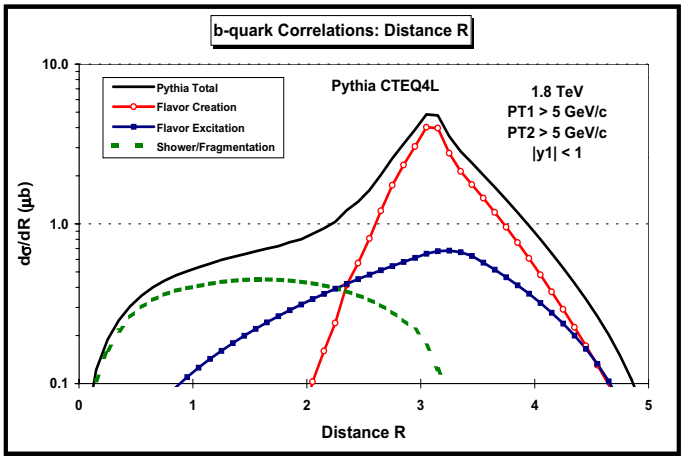

Figure 1.2: Predictions of PYTHIA 6.158 (CTEQ4L, $p_T(hard) > 0$) for the distance $R = \sqrt{\Delta\eta^2 + \Delta\Phi^2}$, between a b-quark and a $\bar{b}$-quark in proton-antiproton collisions at 1.8 TeV [7]. The curves correspond to the three processes.

The production of $b\bar{b}$ pairs within a parton-shower or during the fragmentation process of gluons and light quarks and antiquarks is an important source at the Tevatron. The QCD Monte-Carlo models predictions differ considerably for this

contribution. However, at the Tevatron the **"Parton Shower/Fragmentation"** contribution to the inclusive b quark cross section might be comparable to the contribution from Flavour creation. This source can be isolated by looking for $b\bar{b}$ pairs with $R < 1$, where R is the distance in the $(\eta;\ \phi)$ space between the b and $\bar{b}$ quark as can be seen in figure 1.2.

It seems likely that at the Tevatron all three sources of b quarks, Flavour creation, Flavour excitation, and shower/fragmentation are comparable [7]. One does not expect precise agreement from leading-log estimates. On the other hand, the qualitative agreement indicates that probably nothing unusual is happening in b quark production at the Tevatron. Furthermore, in Run II we should be able to isolate experimentally the individual contributions to b quark production by studying b, $\bar{b}$ correlations in detail.

This will be possible as a consequence of the upgrades in HF triggers, the new SVT hadronic trigger and the lower momentum thresholds in leptonic trigger, and as a consequence of wider detector acceptance, especially important for correlation studies.

The $b\bar{b}$ events topological correlation knowledge are of fundamental interest for important B physics issues at Tevatron like the flavour tagging algorithms, described in chapter 5.

Here we discuss the b quark production. For the **c quark**, the production processes involved are the same. The accuracy of QCD predictions on charm production, suffers of a strong QCD parameters set dependence in particular the charm mass m_c value. Relative weights of the three processes discussed above, are, in the charm production case, ultra-sensitive to the choice of m_c [3].

Nevertheless experimental access to new charm cross sections measurement at CDF in run II, as prospected in section 8.2, via SVT trigger selection, promises to give important new input to QCD calculations.

Chapter 2

Beauty and Charm physics at CDF in runII

In this chapter a selection of topics among the research fields of beauty and charm physics is given. The choice have been done following the theme of CP symmetry violation in the Standard Model, to which a brief resume is done in section 2.1. We selected two sectors where CP violation is searched, B_s^0 meson mixing for beauty sector and D^0 mixing and direct CP violation in charm decays for charm physics, respectively discussed in sections 2.2 and 2.3. As it has been underlined before this two topics are tightly correlated from the experimental point of view to the measurement (chapter 7) and the techniques (chapters 4,5 and 6) presented in this thesis. In the conclusive chapter 8, prospects for B_s^0 mixing and CP violation in the charm sector will be given, also tacking into account the results of this thesis work.

2.1 CPV in the Standard Model

In the Standard Model picture quark masses, flavour violation and CP violation arise all from Yukawa interactions among the quark fields and the Higgs doublet field. A representation of this phenomena is given in the Cabibbo Kobayashi Maskawa CKM matrix mechanism.

The CKM matrix V_{CKM} [8] is a unitary matrix that transforms the mass eigenstates to the weak interaction ones, giving the couplings of the W boson to $\bar{u}_i d_j$ so

that :

$$V = \begin{pmatrix} V_{ud} & V_{us} & V_{ub} \\ V_{cd} & V_{cs} & V_{cb} \\ V_{td} & V_{ts} & V_{tb} \end{pmatrix} \tag{2.1}$$

This matrix can be expressed in terms of four independent parameters which are not predicted by the standard model and have to be determined experimentally. The Wolfenstein parametrization [9] of CKM matrix is written in terms of λ, A, ρ and η as:

$$V \simeq \begin{pmatrix} 1-\lambda^2/2 & \lambda & A\lambda^3(\rho - i\eta) \\ -\lambda & 1-\lambda^2/2 & A\lambda^2 \\ A\lambda^3(1-\rho-i\eta) & -A\lambda^2 & 1 \end{pmatrix} \tag{2.2}$$

The unitarity of the matrix 2.1 leads to orthogonality relations between any pair of columns or rows, like:

$$V_{ud}V_{ub}^* + V_{cd}V_{cb}^* + V_{td}V_{tb}^* = 0 \tag{2.3}$$

Relations of type 2.3 can be represented as triangles (see figure 2.1) in the complex plane (ρ; η), where parametrization 2.2 for the V_{CKM} elements is used. Non vanishing area of this triangle is a hint of CP violation. The three angles of the "unitarity

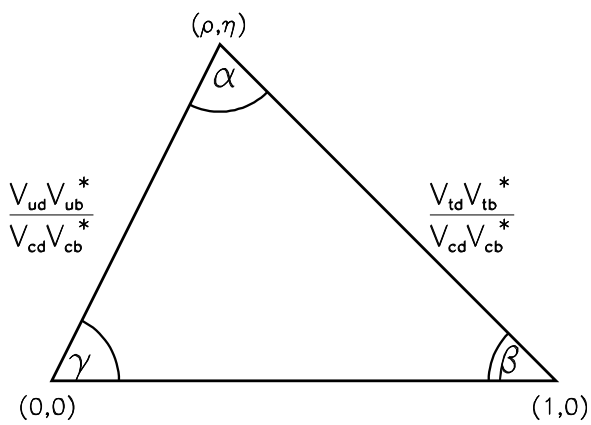

Figure 2.1:

triangle" representing 2.3 are:

$$\alpha = arg[-\frac{V_{td}V_{tb}^*}{V_{ud}V_{ub}^*}]; \beta = arg[-\frac{V_{cd}V_{cb}^*}{V_{td}V_{tb}^*}]; \gamma = arg[-\frac{V_{ud}V_{ub}^*}{V_{cd}V_{cb}^*}] \tag{2.4}$$

Measurements of weak decays of B hadrons determine the magnitudes of the sides of the triangle, while CP asymmetries observables determines the angles. V_{CKM}

elements determination have in B physics a privileged sector since B decays involve most of them. Nonetheless important information can be extracted from Kaons and from charm physics. A strong evidence for CP violation has been recently obtained at the B factories with the $sin2\beta$ measurement in $B \to J/\Psi K_s$ CP asymmetry, the 2002 average turn out to be $sin2\beta = 0.734 \pm 0.054$ [10]. This precision measurement togheter with other experimental bounds, constrain the CP violating phase η to be different from zero to accomodate observed CP violation in the Standard Model.

The goal in the next years is to overdetermine the CKM matrix to test SM consistency, or discover through CKM elements measurements new physics effects. This can result for example in a measured $\alpha + \beta + \gamma \neq \pi$ indicating violation of CKM unitarity.

CDF beauty and charm physics analysis will play a major role in this sector. In the following sections will focus on constraint to CKM mechanism from B_s oscillation frequency measurement which is unique to Tevatron (section 2.2) and on constraints on new physics contributions, possible in charmed mesons mixing and CP violation, section 2.3.

2.2 $B_s - \bar{B}_s$ system oscillations

A B_s^0 meson is made from a b-type antiquark and an s-type quark, while the $\bar{B}_s^0$ meson is made of a b-type quark and an s-type antiquark. The heavy, B_s^H, and light, B_s^L, mass eigenstates can be written as linear combinations of B_s^0 and $\bar{B}_s^0$:

$$|B_s^L >= p|B_s^0 > +q|\bar{B}_s^0 > \tag{2.5}$$
$$|B_s^H >= p|B_s^0 > -q|\bar{B}_s^0 >$$

with

$$|q^2| + |p^2| = 1 \tag{2.6}$$

In writing 2.5, we assume CPT conservation and use of part of the freedom to re-phase the meson states:

$$|B_s > \rightarrow e^{i\zeta}|B_s > \tag{2.7}$$
$$|\bar{B}_s > \rightarrow e^{i\bar{\zeta}}|\bar{B}_s >$$

The mass difference Δm_s and width difference $\Delta\Gamma_s$ are defined as follows:

$$\Delta m_s = M_H - M_L; \Delta\Gamma_s = \Gamma_L - \Gamma_H \tag{2.8}$$

so that $\Delta m_s > 0$ by definition and the Standard Model prediction is that $\Delta\Gamma_s > 0$. The average mass and width are given by

$$M_{B_s^0} = \frac{M_H + M_L}{2}; \Gamma_{B_s^0} = \frac{\Gamma_H + \Gamma_L}{2} \tag{2.9}$$

It is useful to define dimensionless ratios x_s and y_s:

$$x_s = \frac{\Delta m_s}{\Gamma_s}; y_s = \frac{\Delta\Gamma_s}{\Gamma_s} \tag{2.10}$$

The time evolution of the mass eigenstates is simple, following from the fact that they have well defined masses and decay widths:

$$|B_s^H(t) >= e^{-iM_H t}e^{-\Gamma_H t/2}|B_s^H > \tag{2.11}$$
$$|B_s^L(t) >= e^{-iM_L t}e^{-\Gamma_L t/2}|B_s^L >$$

The time evolution of the strong interaction eigenstates is complicated and obeys a Schroedinger-like equation:

$$i\frac{d}{dt}(B_s;\bar{B}_s) = (M - \frac{i}{2}\Gamma)(B_s;\bar{B}_s) \tag{2.12}$$

where M and Γ are Hermitian 2×2 matrices. The offdiagonal elements in these matrices are not invariant under the re-phasing 2.7, they transform as:

$$M_{12} \to e^{i(\bar{\zeta}-\zeta)}M_{12}; \Gamma_{12} \to e^{i(\bar{\zeta}-\zeta)}\Gamma_{12} \tag{2.13}$$

Therefore, physical parameters can only depend on M_{12}, Γ_{12} and $M_{12}\Gamma^*_{12}$. Indeed,the relations between the parameters in the mass eigenbasis and in the interaction eigenbasis can be written as follows:

$$\begin{aligned}(\Delta m_s)^2 - \frac{1}{4}(\Delta\Gamma_s)^2 &= 4|M_{12}|^2 - |\Gamma_{12}|^2 \\ \Delta m_s \Delta\Gamma_s &= -4Re(M_{12}\Gamma^*_{12}) \\ \frac{q}{p} &= -\frac{\Delta m_s + i/2\Delta\Gamma_s}{2M_{12} - i\Gamma_{12}}\end{aligned} \tag{2.14}$$

Defining $\Phi = arg(-\frac{M_{12}}{\Gamma_{12}})$ we can solve for Δm_s in terms of $|M_{12}|$, $|\Gamma_{12}|$ and Φ. Tacking into account that, for B^0 systems and B_s in this case, $|\Gamma_{12}| << |M_{12}|$ and $\Delta\Gamma << \Delta m$ are empirically satisfied, an expansion in Γ_{12}/M_{12} and $\Delta\Gamma/\Delta m$ is then a good approximation that gives for mass and widths differences:

$$\begin{aligned}\Delta m_s &= 2|M_{12}|[1 + O(|\frac{\Gamma_{12}}{M_{12}}|^2)] \\ \Delta\Gamma_s &= 2|\Gamma_{12}|cos\Phi[1 + O(|\frac{\Gamma_{12}}{M_{12}}|^2)]\end{aligned} \tag{2.15}$$

Let focus for the moment on the mass difference Δm_s. In order to calculate this oscillation parameter at the lowest order in the Standard Model one has to consider the "box" diagrams giving $|\Delta B| = 2$ transitions describing B^0 mesons mixing, see figure 2.2. The result is obtained from an effective field theory in which the interactions mediated by heavy particles are described by local operators acting in point-like vertices. The description of such theoretical tools is beyond the goal of

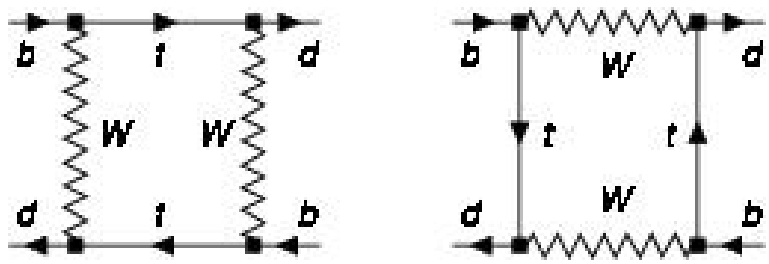

Figure 2.2: Standard Model box diagrams inducing B_d mixing. Same diagrams describes B_s mixing with the replacement of d with s quark.

this discussion. The Standard Model prediction is then:

$$\Delta m_s = \frac{< B_s^0 | H^{\Delta B=2} | \bar{B}_s^0 >}{m_{B_s}} = \frac{G_F^2}{6\pi^2} \eta_B m_{B_s} B_{B_s} f_{B_s}^2 M_W^2 S(\frac{m_t^2}{M_W^2}) |V_{tb} V_{ts}^*|^2 \tag{2.16}$$

where G_F is the fermi decay constant, m_{B_s} is the meson mass, $B_{B_s} f_{B_s}^2$ are the parametrization of the hadronic matrix element, $\eta_B S$ are the coefficient of the local operator relevant for this process in the Wylson operator expansion. The mass difference Δm_s is then proportional to the CKM element V_{ts} thus allowing information on unitarity triangle. An analogue to 2.16 relation holds for B_d^0 mesons mass difference replacing s with d.

In the case of B_d^0 the CKM element involved is V_{td} which relates with Wolfenstein parameters as:

$$|V_{td}| = A\lambda^3 R_t (1 + O(\lambda^4)) = |V_{cb}| \lambda R_t (1 + O(\lambda^4)) \tag{2.17}$$

with $R_t = \sqrt{(1-\bar{\rho})^2) + \bar{\eta}^2}$ being the lenght of one side of CKM unitarity triangle. The measurement of Δm_d defines a circle in the ($\bar{\rho}$, $\bar{\eta}$) plane centered in (1, 0). Since the hadronic uncertainties associated with Δm_d calculations are quite big the extraction of V_{td} and R_t from high precision measurement of Δm_d is diluted somehow. In the case of B_s meson mass difference Δm_s the corresponding CKM element is given by:

$$|V_{ts}| = |V_{cb}| [1 + \lambda^2 (\bar{\rho} - \frac{1}{2}) + O(\lambda^4)] \tag{2.18}$$

$|V_{ts}|$ is smaller than $|V_{cb}|$ by roughly 1 %. In the Standard Model a measurement of Δm_s directly probes the hadronic matrix element calculation. The knowledge on R_t

profits enormously from a measurement of Δm_s because the ratio of the hadronic matrix elements entering $\Delta m_d/\Delta m_s$ can be calculated with a much higher accuracy than the individual terms. In particular the quantity $\zeta = \frac{\sqrt{B_{B_s}} f_{B_s}}{\sqrt{B_{B_d}} f_{B_d}}$ is equal to 1 in the limit of exact $SU(3)_F$ symmetry, the task is then to calculate deviations from unity. The world average for ζ in the year 2000 was $\zeta = 1.16 \pm 0.05$ [11]. In the ratio of mass differences also V_{cb} drops out letting to:

$$\frac{\Delta m_d}{\Delta m_s} = \lambda^2 R_t^2 (1 + \lambda^2(1 - 2\bar{\rho}) + O(\lambda^4)) \frac{m_{B_d}}{m_{B_s}} \frac{1}{\zeta^2} \tag{2.19}$$

With the expected accuracy on Δm_s (discussed in chapter 8), a determination of R_t at the few percent level is achievable. Let now discuss the strategy which can be used to extract Δm_s. The most common way in which the B_s mass difference can be measured is by the time evolutions of initialy tagged B_s decaying as $B_s \to f$ which have non vanishing oscillatory term for example in the case of "flavour specific" final states f. By this we mean that if $B_s^0 \to f$ is allowed $\bar{B}_s^0 \to f$ is not. We define the two decay amplitudes:

$$A_f =< f|B^0 >, \bar{A}_f =< f|\bar{B}^0 > \tag{2.20}$$

In flavour specific channels f, will be $\bar{A}_f = A_{\bar{f}} = 0$ by definition, so the time evolution for B_s^0 for such a final state f and its CP conjugate $\bar{f}$ will read:

$$\Gamma(B^0(t) \to f) = N_f |A_f|^2 e^{-\Gamma t} \frac{1}{2}[cosh\frac{\Delta\Gamma t}{2} + cos(\Delta m t)] \tag{2.21}$$
$$\Gamma(B^0(t) \to \bar{f}) = N_f |\bar{A}_{\bar{f}}|^2 (1-a) e^{-\Gamma t} \frac{1}{2}[cosh\frac{\Delta\Gamma t}{2} - cos(\Delta m t)]$$

where N_f is a time independent normalization factor, $a = |\frac{\Gamma_{12}}{M_{12}}| sin\Phi$ and $\bar{A}\bar{f}$ is the CP conjugate of A_f. Flavour specific decays can be used to measure Δm_s via the asymmetry in decays from mixed and unmixed B_s:

$$A(t) = \frac{\Gamma(B^0(t) \to f) - \Gamma(B^0(t) \to \bar{f})}{\Gamma(B^0(t) \to f) + \Gamma(B^0(t) \to \bar{f})} \tag{2.22}$$

If there is no direct CP violation (in decay amplitude), $|\bar{A}\bar{f}|$ and $|A_f|$ are equal, and the mixing asymmetry reads:

$$A(t) = \frac{cos(\Delta m t)}{cosh\Delta\Gamma t/2} + \frac{a}{2}[1 - \frac{cos^2(\Delta m t)}{cosh^2\Delta\Gamma t/2}] \tag{2.23}$$

where $\Delta\Gamma$ is allowed to have non zero value. In practice $\Delta\Gamma$ is very small from present bounds and a can be set to zero. Applying this approximation we could have a simpler expression for mixing asymmetry that will be proportional to oscillating term with frequency Δm_s. We do not treat here the topic concerning B_s mesons width difference $\Delta\Gamma_s$ which will be of interest for CDF after the Δm_s measurement.

2.3 Mixing and CP violation in Charm sector

2.3.1 $D^0 - \bar{D}^0$ mixing

Within the Standard Model, the processes which mediate the decays of charmed quarks and antiquarks can change the "charm" quantum number by one unit, $\Delta C = \pm 1$. On the other hand, the mixing of D^0 and $\bar{D}^0$ necessitates changing a charm quark, c, into an anti-charm quark, $\bar{c}$, i.e., the "charm" quantum number must change by two units. This can be arranged in the SM only at one loop level and, therefore, is naturally suppressed. However, new physics (beyond Standard Model) contributions can generate $\Delta C = \pm 2$ interactions as well. It is for this reason that neutral meson-antimeson mixing can provide important information about both the Standard Model and new physics beyond the SM. The $D^0 - \bar{D}^0$ system is particularly interesting in this respect as it is the only system that is sensitive to the dynamics of bottom-type quarks. The motivation most often cited in searches for $D^0 - \bar{D}^0$ mixing is the possibility of observing a signal from new physics which dominates the signal from the Standard Model. The low energy effect of new physics particles can be naturally written in terms of a series of local operators of increasing dimension generating $\Delta C = \pm 2$ transitions. These operators, along with the Standard Model contributions, generate the mass and width splittings for the eigenstates of $D^0 - \bar{D}^0$ mixing matrix defined as:

$$|D_{12}>= p|D^0> \pm q|\bar{D}^0> \tag{2.24}$$

with complex parameters p and q determined from the phenomenological (CPT-invariant) $D^0 - \bar{D}^0$ mass matrix. It is convenient to normalize the mass and width differences and define two dimensionless variables x and y:

$$x = \frac{m_2 - m_1}{\Gamma}; y = \frac{\Gamma_2 - \Gamma_1}{2\Gamma} \tag{2.25}$$

where $m_i(\Gamma_i)$ is the mass (width) of the corresponding state, D_i. Clearly, y is constructed from the decays of D into physical states, and so it should be dominated by the SM contributions. If CP-violation is neglected, then $p = q$ and $|D_{12}>$ become

eigenstates of CP. To set up a relevant formalism, let us recall that in perturbation theory, the element ij of the $D^0 - \bar{D}^0$ mass matrix can be represented as

$$[M - i\frac{\Gamma}{2}]_{ij} = m_D\delta_{ij} + \frac{1}{2m_D} < D_i^0|H_W^{\Delta C=2}|D_j^0 > + \frac{1}{2m_D}\Sigma_l \frac{< D_i^0|H_W^{\Delta C=1}|I >< I|H_W^{+\Delta C=1}|D_j^0 >}{m_D^2 - E_I^2 + i\epsilon} \tag{2.26}$$

Here the first order correction term in Equation 2.26 comes from the local $\Delta C = 2$ (box and dipenguin) operators. These operators would give contributions to the dispersive part of M, i.e. only affect x. They are expected to be small in the Standard Model [12], [13], [14]. It is therefore natural to expect that this part of Equation 2.26 might receive contributions from the effective operators generated by new physics interactions. The second order correction term of Equation 2.26 includes bilocal contributions which are induced by the insertion of two Hamiltonians changing the charm quantum number by one unit, i.e., built out of $\Delta C = 1$ operators. This class of terms contributes to both x and y and is believed to give the dominant SM contribution to mixing due to various nonperturbative effects [15]. Some enhancement due to $\Delta C = 1$ operators induced by new physics is also possible, but unlikely given the strong experimental constraints provided by data on D meson decays. Most theoretical estimates suggest that x and y are very small: $x, y \leq 10^{-3}$. The mass and width differences x and y can be measured in a variety of ways, for instance in semileptonic $D \to Kl\nu$ or nonleptonic $D \to KK, K\pi$ decays. The simplest measurement involves counting the "wrong sign" final states, like l^- or π^- in the decay of a meson initially tagged as D^0. This procedure unambiguously measures the mixing rate $r = (x^2 + y^2)/2$ for semileptonic final states, while for the $K\pi$ final state it is complicated by the presence of the double-Cabibbo suppressed (DCS) amplitudes $A_{K\pi}$. It is possible to separate DCS amplitudes from the mixing contribution by performing time-dependent studies of $\Gamma(D \to K\pi)(t)$ [16]. Another powerfull technique for D mixing parameter y measurement, based on lifetime difference between CP eigenstates and CP mixed states, is reported in chapter 8 togheter with the CDF reach expectations on D^0 mixing.

2.3.2 CP violation

While CP violation was first observed in the neutral kaon system and has recently been observed in neutral B mesons, the Standard Model predicts very small effects in both charged and neutral charm mesons. Therefore, the Standard Model background to any non-Standard Model physics for charmed mesons is much smaller than in the B and K systems, making charm an excellent venue to look for new physics using CP violation as a probe. In addition to indirect (in mixing) CP violation mentioned in the previous section, both SM and new physics effects can induce different contributions to the decay amplitudes of D meson. This phenomenon can be traced back to the appearance of complex-valued couplings (CKM parameters) in the $\Delta C = 1$ Lagrangian that mediates D decays and leads to CP-violating difference between decays rates of CP-conjugated states. Studies of direct CP violation usually require two different amplitudes having non-trivial weak and strong phase difference to reach a given final state. Final state hadron dynamics must provide non-zero strong phase shifts. Unfortunately, in charm decays, the impact of the final state hadronic rescattering cannot be described accurately in perturbative QCD. Various models can be called upon, but the predictions are not robust. Let us consider a decay of a charmed meson. If there are two different amplitudes A_1 and A_2 with associated strong phases δ_1 and δ_2, then the decay amplitude for $D \to f$ is given by:

$$A_f = A_1 e^{i\delta_1} + A_2 e^{i\delta_2} \tag{2.27}$$

For the CP conjugate reaction, $\bar{D} \to \bar{f}$ the weak phases change but the strong phases stay the same

$$\bar{Af} = A_1^* e^{i\delta_1} + A_2^* e^{i\delta_2} \tag{2.28}$$

The CP violating asymmetry is given by:

$$A_{CP} = \frac{|A_f|^2 - |\bar{Af}|^2}{|A_f|^2 + |\bar{Af}|^2} = \frac{2Im(A_1^* A_2) sin(\delta_1 - \delta_2)}{|A_1|^2 + |A_2|^2 + 2Re(A_1^* A_2) cos(\delta_1 - \delta_2)} \tag{2.29}$$

As discussed above, one selects final states that can be reached from at least two different routes. In charmless B decays the two different weak amplitudes are typ-

ically associated with the tree and penguin transitions. As follows from Eq. 2.29, A_{CP} is directly proportional to the sine of the strong phase difference. While the theoretical status of FSI phases in B decays is not yet settled, in charm decays FSI have been observed. Moreover, final state rescattering effects are appreciably large in the D meson system due to the fact that its mass lies in the middle of the region populated by the light quark resonances [17], [18], [19]. Therefore, the final state phase is not in itself a problem for the observation of direct CP violating effects in charmed meson decays. Small expected values for A_{CP} arise in the Standard Model, because the Cabibbo part of the CKM matrix is "almost" unitary, i.e., weak phase effects in charmed decays are tiny, that makes the observation of CP violating effects problematic. However, new physics can vastly enhance charm CP violating asymmetries, thus making charm a very good place for new physics searches [20]. As argued above, A_{CP} is indeed difficult to predict because of the hadronic uncertainties in the amplitudes and strong phases. We note that CP violation is bound to be larger in Cabibbo suppressed decays than in non-suppressed decays. But how large A_{CP} can be? It's been argued that for Cabibbo suppressed decays it cannot be larger than 10^{-3}. This is based on the rephasing-invariant quantity, or Jarlskog invariant:

$$J = Im[V_{ij}V_{kl}V_{ik}^{*}V_{jl}^{*}] \tag{2.30}$$

where any choice of $i \neq j$ and $j \neq k$ is allowed. Using current approximate values for the CKM elements and taking $sin(\delta_1 - \delta_2)$ equal to one, then for Cabibbo suppressed decays the asymmetry can be as large as 10^{-3}. This is indeed a small asymmetry. Nevertheless, searches for CP violation in charm decays have been going on for quite some time but have reached accuracies of only several percent [21], [22]. The $D_s^{\pm}$ decays present another situation. Detailed calculations by Buccella et al. [23] have some asymmetries in rare decays as large as $3 \cdot 10^{-3}$ and in $D^{\pm}$ decays the largest prediction is $8 \cdot 10^{-3}$. In section 8.4 of chapter 8 we will focus on CDF strategy for CP violation in D mesons decays.

Chapter 3

The CDF detector at Tevatron

3.1 The Tevatron $p\bar{p}$ collider

The Tevatron proton-antiproton collider is the highest-energy particle collider currently operational in the world. To exploit this unique tool fully, and to meet the goals of CDF and D0 experiments research program, an upgrade of the Fermilab accelerator complex has been done [24]. The initial Run II goal, called Run IIa, is to achieve a luminosity of $5 \cdot 10^{31} cm^{-2} sec^{-1}$ and an integrated luminosity of 2 fb^{-1}. It is thought that the ultimate potential of the Run II upgrades is to achieve luminosities up to $2 \cdot 10^{32} cm^{-2} sec^{-1}$, Run IIb, and order 10 fb^{-1} of integrated luminosity. The Run II luminosity goals are about a factor of 100 increase over the original $1 \cdot 10^{30} cm^{-2} sec^{-1}$ design goal of the Tevatron Collider. The energy in the center of mass of the colliding beams is increased up to 2 TeV, from 1.8 TeV in the Run I. Currently in november 2002, Tevatron reached a peak Luminosity of $3.8 \cdot 10^{31} cm^{-2} sec^{-1}$ at a $\sqrt{s} = 1.96$ TeV.

Both increased Luminosity and center of mass energy, togheter with detector acceptances upgrades, will provide a major increase in the reconstructed physics sample size.

Luminosity L of $p\bar{p}$ in the ideal case of head-on collisionwithout a crossing angle and optimal allignment at the Tevatron, is given by:

$$L = \frac{f B N_p N_{\bar{p}}}{2\pi(\sigma_p^2 + \sigma_{\bar{p}}^2)} F(\frac{\sigma_l}{\beta^*}) \tag{3.1}$$

where f is the revolution frequency, B is the number of bunches in each beam, N_p

and $N_{\bar{p}}$ are the number of protons and anti-protons in each bunch, σ_p and $\sigma_{\bar{p}}$ are the transverse beam sizes r.m.s. (around 30 μm) at the interaction point, and F a form factor that depends on the ratio of longitudinal rms size of the beam σ_l and the beta function at interction point β^*, which accounts for beam emittance.

The most signficative improvements to Luminosity are obtained by increasing the number of bunches per beam, from 6 in Run I to 36 and later to 108 in Run II, as can be seen in figure 3.1. Figure 3.1 shows also the principal limitation in the choice

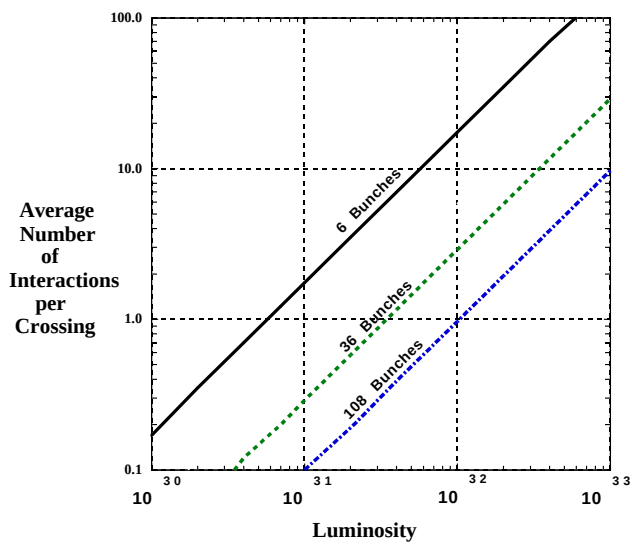

Figure 3.1: Average number of interactions per crossing as a function of Luminosity and of the number of bunches.

of accelerator parameters which is the superposition of multiple elementary proton anti-proton interactions within the same bunch crossing. At high luminosities this superposition increases the complexity of the event in terms of tracks multiplicity and pile-up in the detector elements, making the events selection for the trigger systems and the reconstruction of the events more difficult. At current operations the mean number of interaction per bunch crossing is slightly less than one.

In figure 3.2 the sequence of accelerator steps from p and $\bar{p}$ production to the Tevatron, is shown in sketch. We recall in the following the principal characterists of each step.

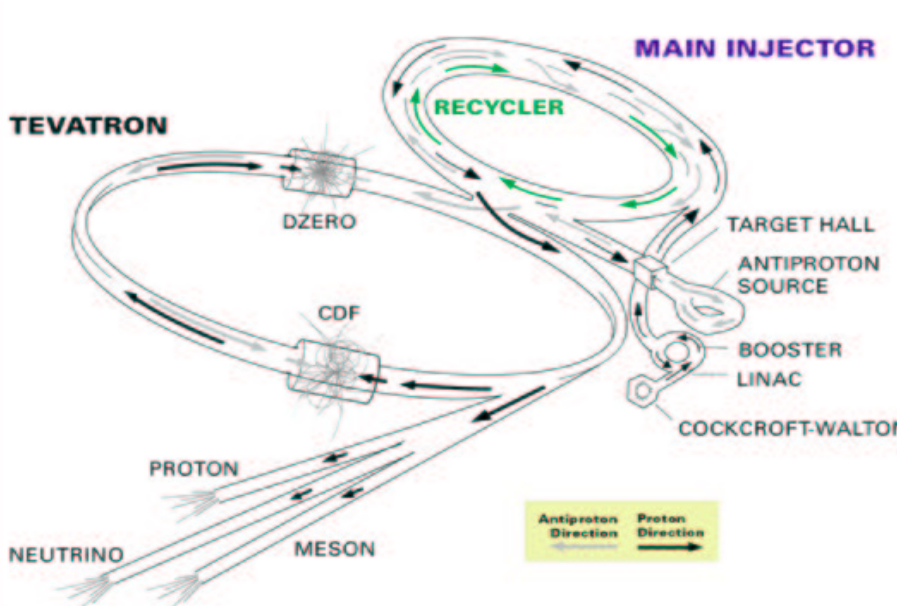

Figure 3.2: Sketch of Fermilab accelerators complex, from p and $\bar{p}$ production, initial acceleration in the booster, the main injector and finally the Tevatron.

Proton production and the Booster

The process begins with a **Cockcroft-Walton** accelerator, which feeds negative hydrogen ions to a 150 m linear accelerator **Linac** having 400 MeV energy. Protons enter then in the **Booster**, a synchrotron whose diameter is about 150 m, where they reach the kinetic energy of 8 GeV. Linac and Booster togheter are able to provide pulses of $5 \cdot 10^{12}$ protons for antiproton production every 1.5 s, or $6 \cdot 10^{10}$ protons per bunch in series of 5 to 7 bunches repeated 36 times every 4 seconds. After leaving the Booster protons are transferred to the Main Injector.

Main Injector

The Main Ring was originally built to provide 400 GeV protons to Fermilab experiments; later on, it was converted to act as an injector to Tevatron. The **Main Injector** is now a 3 km lenght circular accelerator, which brings protons and antiprotons from a kinetic energy of 8 GeV to a total energy of 150 GeV. The maximum beam size $3 \cdot 10^{13}$ particles divided into up to504 bunches of $6 \cdot 10^{10}$ (anti)protons. The Main Ring can be used in several operation modes: antiproton production, p

and $\bar{p}$ boosting before the injection into Tevatron and anti-proton deceleration, in order to recover unused anti-protons after Tevatron collision runs.

Anti-proton production

To produce anti-protons, a pulse of $5 \cdot 10^{12}$ protons at 120 GeV is extracted from the Main Injector and focused on a nickel target. A lithium lens collects the $\bar{p}$ produced in the collision, with a wide acceptance around the forward direction, at energies close to 8 GeV. The anti-proton bunches are then moved to a "Debuncher Ring", where they are transformed to a continuous beam and stochastically cooled and then to the "Accumulator" where they are further cooled. The anti-proton stacking rate is . When a sufficient number of anti-protons (up to 10^{12}) is available, stacking is suspended and the antiprotons are transferred to the anti-proton Recycler Ring.

Recycler Ring

The **Recycler Ring** lies in the same enclosure as the Main Injector, it is built with permanent magnets, which allow a stable running conditions for anti-proton storing. Bunches of $\sim 2 \cdot 10^{11}$ anti-protons are trasferred to the Recycler Ring from the Accumulator about every half an hour. The anti-protons remaining in the Tevatron collider after a store can be slowed down through the Main Injector to an energy of 8 GeV, and then stored in the recycler where they are cooled and stored for next Tevatron store. A factor of 2 of increase in L is expected to be reached by "recycling" in this way, a fraction up to 2/3 of antiprotons still circulating in Tevatron after store end.

Tevatron

The Tevatron is a 6 km circular accelerator, where protons and antiprotons rotating inside the same beam pipe in opposite directions, are accelerated from 150 GeV up to 1 TeV. Super-conducting magnets producing a magnetic field $B \simeq 5.7$ are positioned along the beam orbit. During collider store istant Luminosity slowly decreases. In the early stages of the store the most important cause of this is intra-

beam scattering, some hours later the depletion of anti-protons during collisions become more relevant. This trend can be seen in figure 3.3, corresponding to a november 2002 tipical Tevatron store.

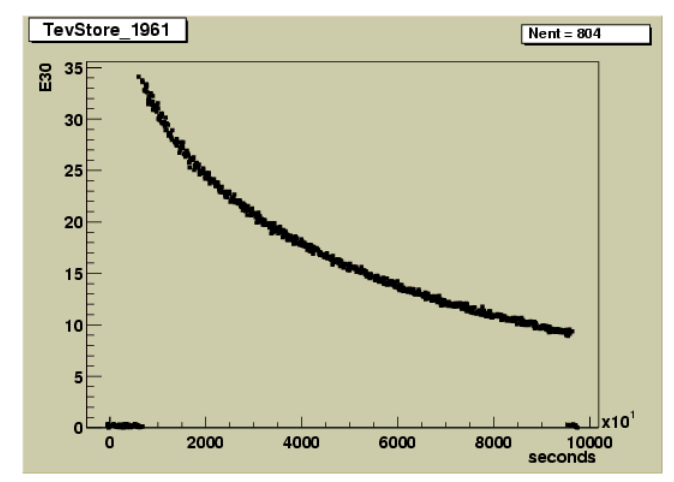

Figure 3.3: Tipical Tevatron store Luminosity shape versus time (seconds). This plot corresponds to Tevatron store 1961 taken in november 2002, the duration of the store is around 25 hours, initial istantaneous Luminosity is $3.5 \cdot 10^{31}$. Luminosity decreases to $1/e$ of its initial value after around 15 hours.

3.2 CDF overview

The **CDF** detector is general purpose for several physics topics in the Tevatron Run II data tacking (as a general reference for this chapter see ref [25]). The two main research fields are: the **high Pt physics** including top quark measurements, Higgs and beyond the standard model searches and **low Pt physics** regarding beauty and charm physics as well as CP violation studies.

Major detector and trigger system upgrades has been done since Run I in order to cope with the high Luminosity and higher collision rate of Run II. Actually as described in previous section the increase in the number of p and $\bar{p}$ bunches (36×36 at the moment) leads to a inter-bunch crossing time of 396 ns (2.4μs in Run I); this condition was the motivation to completely redesign the trigger and data acquisition systems.

Efforts were also made to extend detector acceptance in order to collect large data sample of low cross section physics like *top* quark and Higgs events. For the B physics point of view the two main upgrades which makes today CDF an HF experiment are the brand new **SVT** trigger (based on new Silicon Vertex detector **SVXII**) designed to select, with high efficiency, events containing $b\bar{b}$ pairs among the huge QCD background, and a new **Time of Flight** detector with which B flavour tagging CDF capabilities will substantially increase thus allowing high precision $B - \bar{B}$ system oscillation. This two items are discussed in detail respectively in chapters 4 for SVT and chapters 4 for TOF.

In the following sections we give a short description of the CDF detector subsystems, a general view of CDF is shown in figure 3.4. Sections 3.3 and 3.4 are devoted to the systems for charged particles tracking, section 3.5 to the TOF, section 3.6 to the CDF calorimetry system, section 3.7 to muon detectors and section 3.8 to the CDF trigger system. Figure 3.5 subdetectors positions can be seen.

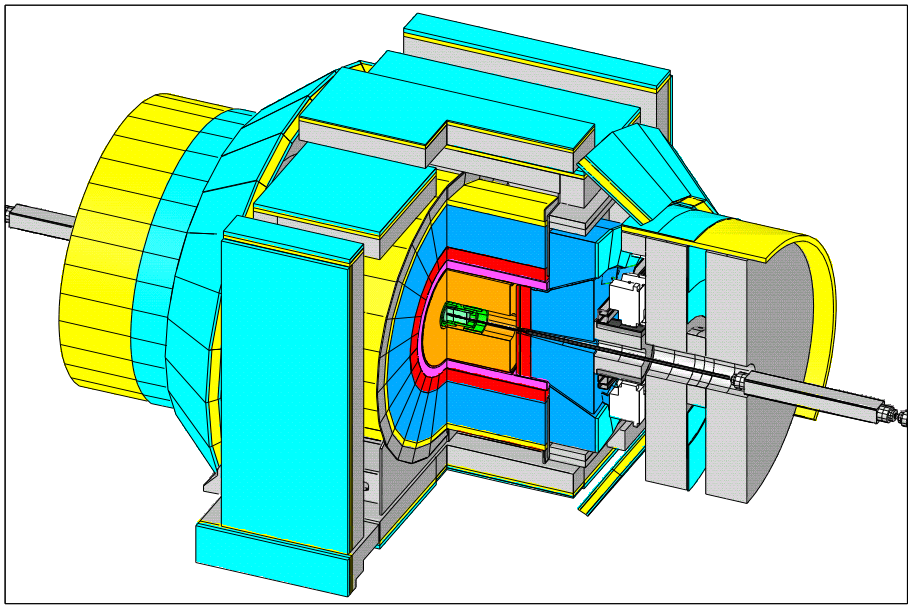

Figure 3.4: Isometrical view of the **CDF** detector. The cut let see the internal subdetectors.

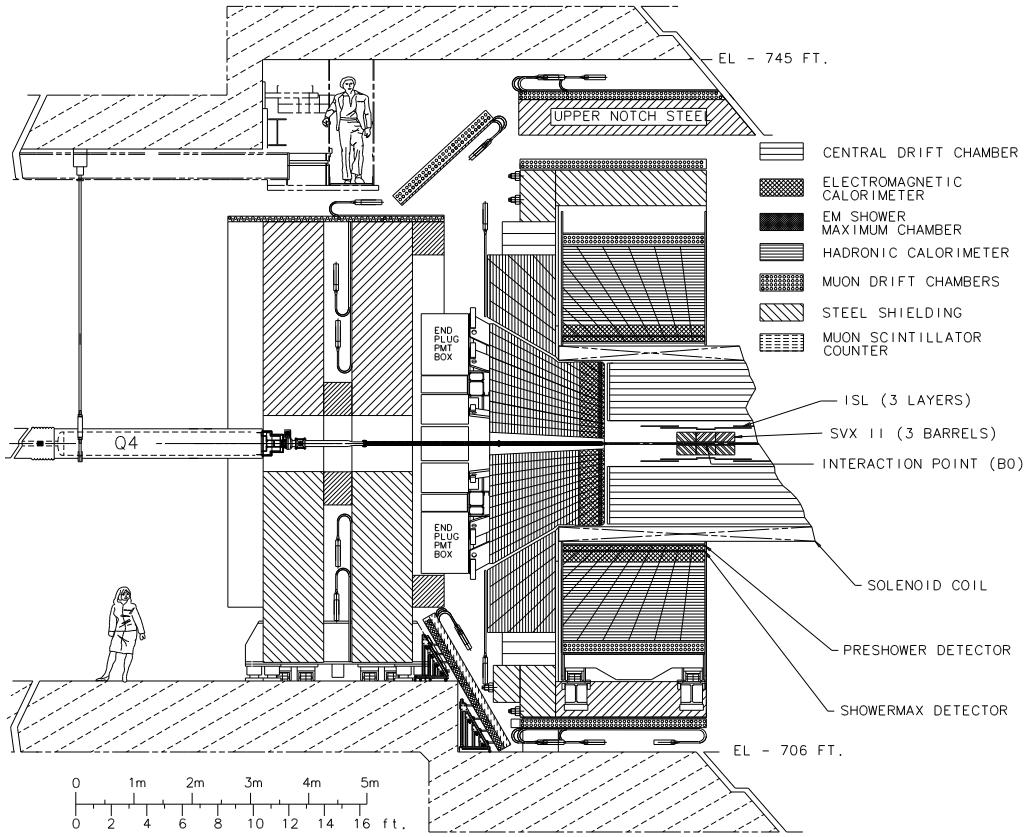

Figure 3.5: Elevation view of one half of the *CDF* II detector.

3.3 Silicon Vertex Detector

CDF make use of three concentric silicon detectors, starting from the nearest to the beam pipe to the outer one: the "Layer 00" **L00** [26], the "Silicon Vertex Detector" **SVXII** and the Intermediate Silicon Layers **ISL**.

$SVXII$ is composed of three cylindrical barrels with a total length of 96 cm. Each barrel is radially divided into 12 mechanical *wedges* and longitudinally divided into two *electrical barrel*. Each $SVXII$ barrel supports five layers of double sided silicon wafers (*ladders*). One side of each wafer provides measurement in the transverse plane (axial strips); the other side strip deliver 3D information. $SVXII$ extends radially from 2.45 to 10.6 cm and along z up to 45 cm on both side of nominal interaction point. Readout and signal digitization is embedded on the detector, which contains readout hybrids directly at the end of each electrical ladder.

The ISL consists of a double sided silicon layer similar to those in $SVXII$, placed at $R = 22$ cm in the central η region, and of two forward layers between $1 < |\eta| < 2$ respectively at 20 and 28 cm from the beam line. Togheter with $SVXII$, ISL makes possible to reconstruct tracks in the forward region, beyond the acceptance of the Central Outer Tracker COT. In the central region tarcks will have up to 7 precision points in the silicon layers for transverse plane fitting.

$L00$ is the most recent upgrade of the CDF tracking system. It is a single sided, radiation hard silicon layer, placed immediately outside the beam pipe at $R \simeq 1.5$ cm. Being so close to the interaction point $L00$ will improve noticeably the impact parameter off-line resolution. The impact parameter resolution for $1GeV/c$ tracks from roughly $50\mu m$ to $\approx 25\mu m$. The improvement of impact parameter resolution at low momenta leads to a substantial increase in b-tagging efficiency, discussed in chapter 5. Moreover, the expected improvement of the vertex-finding resolution will lower the proper time resolution on b hadron decays and thus enhance CP violation and B_s mixing measurements, see Chapter 8.

Silicon Vertex Detector has much wide acceptance than in Run I and it is also

able to provide "stand alone" tracking information, without using the COT.

3.4 The drift chamber, COT

The main detector on which the Run II CDF tracking system relies, is the "Central Outer Tracker". The COT is a large open cell drift chamber for charged particle reconstruction in the central region $|\eta| < 1$. COT lies at a distance from the beam between 40 and 138 cm. tracks with a transverse momentum af at least 300 MeV are reconstructed by the COT. It is composed of eight superlayers of cells consisting of twelve layers of sense wires each, alternating with field-shaping wires. The four axial superlayers alternate with four stereo superlayers thus providing up to 48 axial and 48 stereo measurement for each track. There are 30,240 readout channels for the entire detector. Typical drift times are less than 100 ns by using small cell sizes (the maximum drift distance is ≈ 0.9 cm) and a fast gas mixture composed by $Ar - Ethane - CF_4$. The complete chamber is roughly 1.3% of a radiation length at normal incidence.

Magnet

The tracking system is enclosed in a superconducting solenoid, which provides a uniform magnetic field of 1.41 T. The solenoid is built of Al-stabilized NbTi superconductor operating at liquid helium temperature, with a current of around 4500 A corresponding to $\simeq 1100 A/m$ of current density.

3.5 Time of Flight, TOF

A system capable of identifying pions, kaons and protons has been proposed and approved as "beyond the baseline" part of CDF upgrade for Run II [26]. This is especially relevant in B physics, where particle identification can help increasing the efficiency of flavour tagging alghoritms, especially those based on Kaons identification.

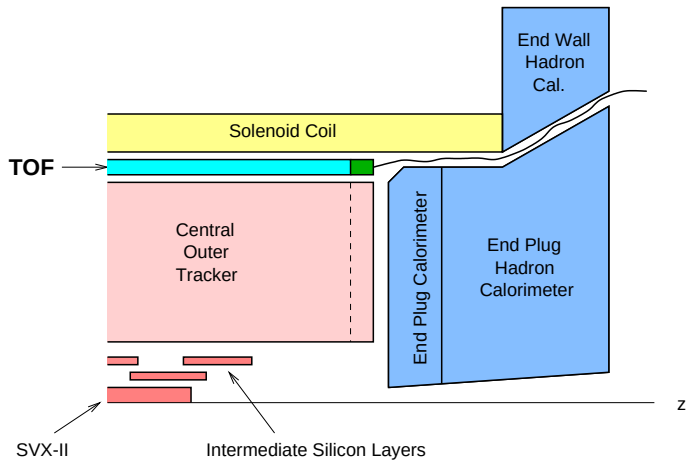

Figure 3.6: Side view of half CDF detector inside coil, with TOF system. Signal cables from TOF bar phototubes are also visible.

At this purpose a cylindrical array of scintillating bars has been inserted between the COT and the solenoid in order to measure, by integrating tracking information from COT, the **Time of Flight** of charged particles. Given that TOF bars are at 1.4 m from the beam (see figure 3.6) and that TOF hits are measured with a design resolution of 100 ps, this will allow a K/π separation at 2 σ level for $p_T < 1.6$ GeV. TOF detector and flavour tagging perspectives are discussed in detail in chapter 5.

3.6 Calorimetry

CDF using scintillator sampling calorimeters, divided into separate sections for electromagnetic and hadronic energy measurements, providing a total coverage for $|\eta| < 3.64$. The entire calorimeter is segmented into projective towers. Each tower consists of alternating layers of passive material, lead for the e.m. section ($\sim 21X_0$) and iron for hadronic compartements ($\sim 7\lambda_I$), and scintillating tiles. The signals from the tiles is read through wave-lenght shifters embedded in the scintillators, and then driven to photo-multiplier tubes. The central ($|\eta| < 1.1$) and end-wall calorimeters CEM and $CHA - WHA$ were recycled from Run I, while for $1.1 < |\eta| < 3.64$ the **Plug** calorimeters (originnally implemented with drift chambers, now scintillators) are completely new, see figure 3.7.

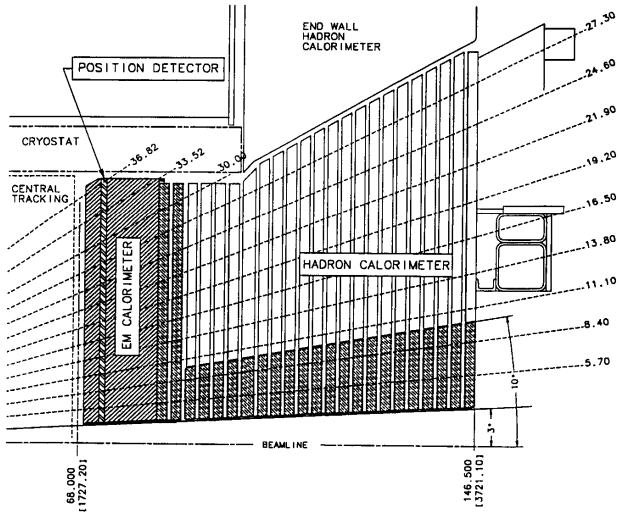

Figure 3.7: Side view of the new CDF End Plug calorimeters.

Just between the solenoid and the electromagnetic calorimeter a preshower detector **CPR** is inserted. Moreover a finer strip structure layer of calorimeter CES (Central Electromagnetic Strip detector) is inserted in the electromagetic section CEM at a dept of around 6 X_0 in order to measure electromagnetic shower maximum. These two detectors allow a good electron and photon identification, important both in B physics to select $B \to e + X$ decays (with an efficiency of $\sim 80\%$) and in jet physics to determine the electromagnetic fraction in the jet.

Calorimeter segmentation in terms of $\Delta\eta \times \Delta\Phi$ varies from 0.1×7.5^o to 0.64×15°. Energy resolutions for e.m. and hadronic components are expected to be respectively $\sigma_E/E = 16\%/\sqrt{E} \oplus 1\%$ and $\sigma_E/E = 80\%/\sqrt{E} \oplus 5\%$.

3.7 Muon detectors

The outermost component of CDF is a set of scintillators, drift tubes and absorbers used for the detection and identification of muons.

Muons in the region up to $|\eta| < 2$ are identified in the CMU (Central Muon chambers), in the CMX (Central Muon Scintillator extension) for $|\eta| < 1$ and in the IMU (Intermediate Muon Chambers) for $1 < |\eta| < 2$. Muon momentum is

measured with high resolution (minimum Multiple scattering) in the central trackers, $SVXII + COT + ISL$ for $|\eta| < 1$ and $SVXII + ISL$ only for $1 < |\eta| < 2$.

Even if drift times of the muon chambers ($\sim 1\mu$s) are big with respect to the bunch crossing, fast scintillator response is used to associate muon stubs to the appropriate event.

3.8 Trigger and DAQ system

Since the collection rate in hadron collider experiments is well beyond the imaginable storage rate, background excess is a general plague of hadronic experiments. The well known cure is a DAQ system intelligent enough to select and discard events on the basis of the information available from the detectors.

In the case of CDF II the collision rate is effectively equal to the crossing rate of $7.6MHz$, while tape writing speed is less than $50Hz$. The role of the trigger is that of efficiently extract the most interesting physics events from the large number of *minimum bias* events: for example the total $b\bar{b}$ production cross section is approximately 6 orders of magnitude smaller than the minimum bias one.

The CDF II trigger system, see figure 3.8, inherits the 3 level architecture of CDF I. At each trigger level more accurate information from the detectors is available and more complicate calculations can be implemented: **Level 1** is based on limited resolution calorimetry and tracking, **Level 2** uses full tracking resolution and calorimetric clustering then evaluating the event interest with a set of programmable processors, **Level 3** uses a full detector reconstruction in a commercial processor farm to take the final decision on the processed events. Given the complexity and size of the information acquired at the various stages, and evaluated the processing time necessary to make a decision based on the available information, we can define the maximum processing rate for each trigger stage.

Assuming that accept rates for each level are well tuned enough, a pipelined architecture can be implemented with the various trigger stages: detector data is

stored in buffers deep enough and shifted. The buffer depth is chosen so that the traveling time of a single detector acquisition through the buffer is greater or equal to the mean time needed by the corresponding trigger stage to process the event and come to a decision.

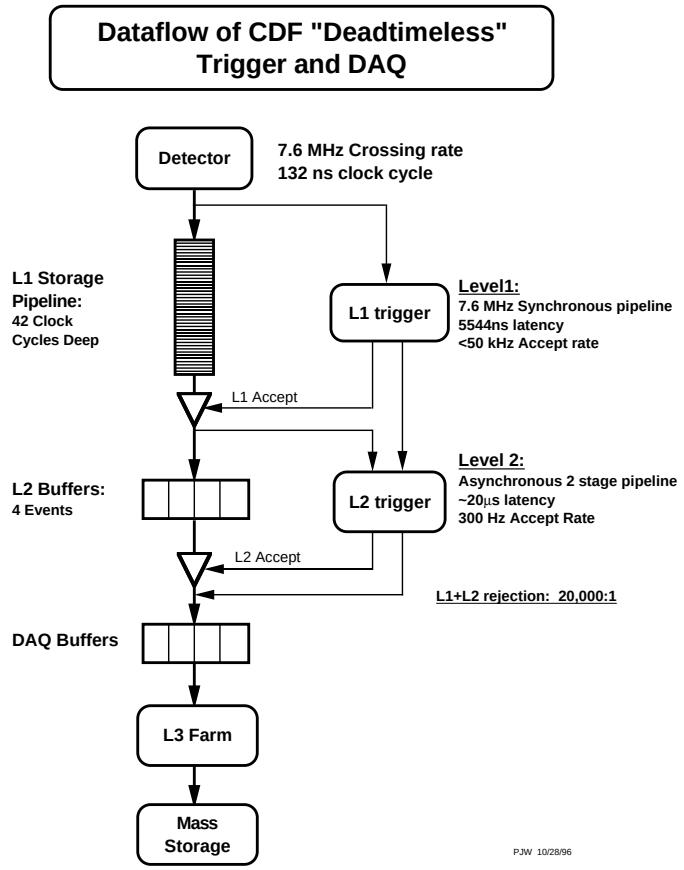

Figure 3.8: General architecture of CDF Data Acquisition and Trigger systems.

Let see what the rates and rejection ratios required at each trigger stage are. The initial constraint is of course that of reducing the $7.5MHz$ event rate into the sustainable output rate ($50Hz$).

The proposed CDF II implementation breaks up the needed rejection in three distinct layers, with processing times of $5.5\mu s$, $20\mu s$ and $10ms$. The choice of this time break up comes from many interplaying constraints. First of all the particle physics under investigation defines the rate of desirable events. On the opposite side, bare technicalities define the maximum achievable storage rate: detector granularity,

occupation, and technological limits in IO throughput towards storage devices. Half way between these two are the technical limitations coming from the specific detector design: readout electronics dead time in particular.

Dead time varies among detector parts, thus making certain parameters available earlier or later in the trigger chain.

The need of building a deadtimeless device drives the grand design of the DAQ system, and brings us to the choice of having the trigger chain splitted in levels of increasing information accuracy and complexity. We describe now these Levels one by one, the trigger structure is shown in figure 3.9.

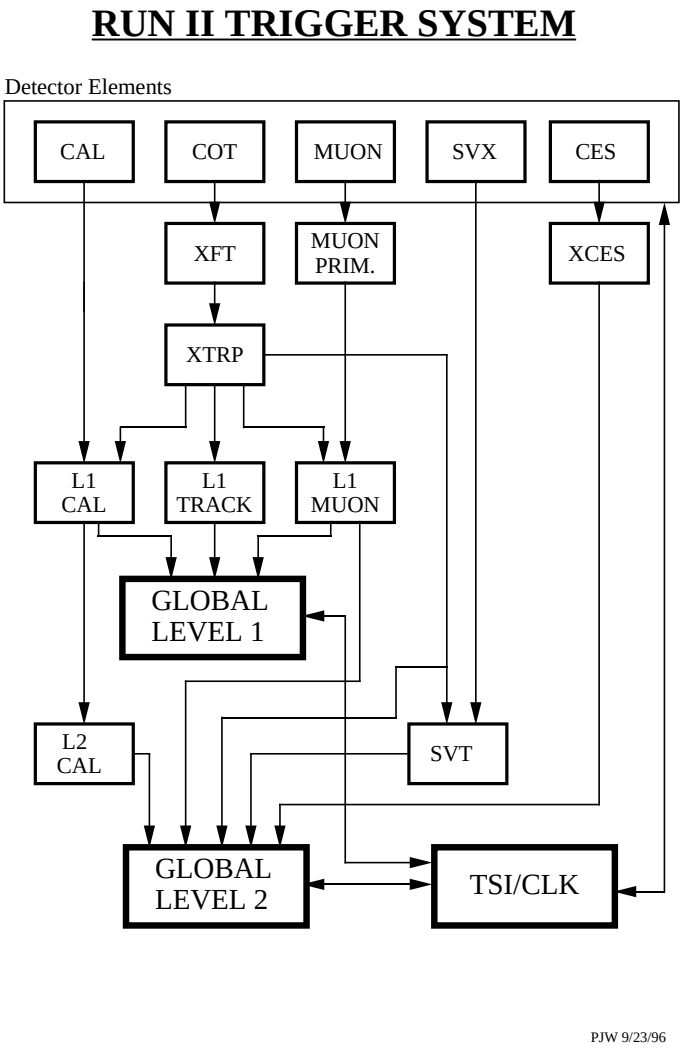

Figure 3.9: The CDF Trigger system.

3.8.1 Level 1

The **Level 1** trigger processes in parallel calorimetry information (L1CAL), muon detector information (MUOM PRIM-L1MUON), and hits from the Central Outer Tracker (XFT XTRP-L1 TRACK). Tracks fitted on these hits are also sent to the calorimeter and muon section of the trigger, in order to implement a better particle recognition.

L1CAL identifies two categories of events: object triggers (e^-, γ and $jets$) and global triggers (total transverse energy ΣE_T and missing transverse energy $\not{E}_T$). The object triggers are formed by applying thresholds to individual calorimeter towers and eventually matching the calorimetric hits with tracks from the XFT. The global triggers are done applying a threshold to the weighted sum of individual tower readouts.

The muon section identifies tracks in the muon chambers ($Stubs$) and hits in the scintillator. $Stubs$ are then eventually matched (at a coarser resolution than offline) with COT tracks and muons with various characteristics are thus flagged.

COT information is translated in fitted tracks parameters by the XFT system, which makes them available for $Level1$ and $Level2$ processing.

XFT reconstructs tracks parameters using COT hits and ignoring z information: XFT tracks are 2-dimensional and at low tracking resolution (the SVX is not exploited). The track-finding efficiency of this device is greater than 96%, the momentum resolution is $\Delta P_t/P_t^2 \approx 2\%$ and the ϕ_0 (azimuth of the track on the z axis) resolution is better than $6mrad$. The minimum track P_t is $1.5GeV/c$.

3.8.2 Level 2

This trigger level can be pictured as divided in two parts: the first stage operates event building, while the second implements algorithms on dedicated CPUs in order to take trigger decisions based on joined $Level1$ and $Level2$ outputs. Each of these stages takes half of the total processing time for $Level2$.

Event building is done in parallel: L2CAL processes the calorimeter data and

implements the clustering algorithm needed to correctly identify hadronic jets. Simultaneously the track processor **SVT** integrates COT information with $SVXII$ readouts producing quasi-offline resolution 2D (in the transverse plane) track parameters.

Customized algorithms can be developed specifically for each trigger channel and are distributed on a set of four CPUs (Level-2 processors). Chapter 4 is dedicated to SVT hadronic track trigger device, on which HF physics analysis presented in this thesis are based.

3.8.3 Level 3

The third trigger level trigger is implemented in a farm of commercial processors, running under the Linux operating system. The purpose of this farm is that of reconstructing the event at full resolution, distributing the information to the online monitoring and data logger programs and feeding it to the trigger algorithms, which are in charge of making the decision of storing the event. At the same time event integrity is checked.

The reconstruction at full resolution is implemented using lower trigger levels to drive the algorithm: when the lower trigger levels generate an accept signal for that event, the level 3 farm calls the reconstruction routines needed to verify at full detector resolution the presence of that triggering event, this is in some sort a confirmation of the trigger decision.

Selected events are finally output to tape, with a maximum rate of about $50Hz$ (which means $12.5MB/sec$ or $250nb$ at $\mathcal{L} = 2 \cdot 10^{32} cm^{-2}\, s^{-1}$).

Chapter 4

Silicon Vertex Tracker, a dedicated HF trigger

4.1 Introduction

The CDF detector upgrades which are relevant for the SVT are the new tracking system formed by COT and SVXII described in chapter 1. We recall here some highlights of the new silicon detector on which SVT is based. The CDFII silicon vertex detector (SVXII and Layer00) covers the region from 1.5 to 10 cm from the beamline and about 2 units in pseudorapidity. SVXII is made of 5 layers of double-sided ($r - \Phi$ and $r - z$ readout) microstrip sensors arranged in a 12-fold azimuthal geometry and segmented in 6 longitudinal barrels (3 mechanical units, each read out at both ends) along the beam line (CDF z-axis). Layer00 is made of one layer of radiation hard silicon microstrips ($r - \Phi$ readout) placed just outside the beam pipe ($r = 1.5$ cm).

The SVT trigger installation has been made possible by a completely new general trigger architecture. The CDFII trigger actually consists of three levels. Its challenging task is to reduce the 5 MHz level 1 input rate down to a Level 3 output rate of 50 Hz for data storage and analisys. Levels 1 and 2 are completely hardware implemented while level 3 is software implemented and runs on a PC farm. The most relevant Level 1 device is the eXtremely Fast Track finder processor XFT which reconstructs 2-D tracks (in the $r - \Phi$ plane, transverse to the beam line) using the hits in the central drift chamber COT. The SVT is part of the level 2 trigger.

It receives the list of COT tracks (p_T and Φ coordinates) from the XFT processor on one hand and the digitized pulse heights on the silicon layers ($\sim 10^5$ channels) on the other hand and reconstructs tracks with quasi-offline quality. The expected resolution for SVT tracks is: $\delta\Phi \sim 1$ mrad, $\delta p_T \simeq 0.003 \cdot p_T^2$ GeV/c and $\delta d_0 \simeq 35\mu m$ respectively for azimuthal angle, transverse momentum and track impact parameter i.e. the distance of closest approach of the particle trajectory helix to the z-axis of the CDF reference system.

By providing a precision measurement of the impact parameter SVT allows triggering on events containing long lived particles. B hadrons in particular have a decay length of the order of 500 μm and tracks which come out of the B decay vertices have an impact parameter on average greater than 100 μm. This novel feature, available for the first time at a hadron collider experiment, greatly enriches the CDF heavy flavour physics program. In particular it provides direct access, by triggering on themself, to rare purely hadronic B decays like $B \to \pi\pi$ and $B_s \to D_s\pi$ with $D_s \to$ hadrons, which are extremely interesting respectively for CP violation and Bs mixing.

In section 4.2 the working principles and basic ideas of SVT system are described while in section 4.3 first results and performance of SVT trigger on 2001 CDF commissioning data taking period are given. Section 4.4 defines the two track trigger selection as it is performed at present running conditions.

4.2 Working principles

The SVT has a very short time to perform its task (on average ~ 20 μs per event) to keep up with the 50 KHz level 1 accept rate. In order to speed up operations SVT has a parallelized design: it is made of 12 identical azimuthal slices ("wedges") which work in parallel. Moreover tracks are reconstructed in 2-D only (stereo information from SVXII is dropped) and only with P_T above 2 GeV/c. Track reconstruction is performed in two steps: in the pattern recognition step, candidate tracks ("roads")

are searched among a list of precalculated low resolution patterns; in the subsequent track fitting step the full resolution fit of the hit coordinates found within the roads is performed using a linearized algorithm. The pattern recognition step is performed in a completely parallel way by the Associative Memory system which uses full custom VLSI chips (AMchips) [27].

The Associative Memory system compares the SVT input data with the set of precalculated patterns. A pattern is defined as a combination of five bins ("SuperStrips"): four SuperStrips correspond to the position coordinates of the particle trajectory on four silicon layers which can be chosen among the five SVXII layers and Layer00, the fifth SuperStrip corresponds to the azimuthal angle of the particle trajectory at a distance $r = 12$ cm from the beam line. This distance was found to maximize average pattern coverage. The output of the AM system is the list of patterns ("roads") for which at least one hit has been found on each SuperStrip. Each SVT wedge uses $\sim$ 32K patterns which cover more than 95% of the phase space for $pT > 2$ GeV/c. Simulation studies have shown that SVT performance is optimized, in terms of processing time and final resolution, by choosing a SuperStrip size of about 250 μm on the silicon layers and 5° for the Φ angle measured by XFT. The track fitting method is based on linear approximations and principal component analysis [28]. The analytical relationship between the track parameters and the 6 measured hit coordinates (hit positions on 4 silicon layers, curvature and azimuthal angle of XFT track) can be expressed in terms of 6 equations:

$$P_j = P_j(\vec{x}) = \vec{F_j} \cdot \vec{x} + Q_j \tag{4.1}$$

where, $\vec{x}$ is the vector of hit coordinates and $\vec{P} = (P_1, P_2, ..., P_6) = (d, c, \Phi, \chi_1, \chi_2, \chi_3)$ is a vector consisting of: the impact parameter d, the curvature c, the azimuthal angle Φ at the point of closest approach to the $z-$axis, and three independent constraints (χ_1, χ_2 and χ_3) which all real tracks must satisfy within detector resolution effects.

F_j and Q_j are constants which depend only on the detector geometry and on the

magnetic field. Once pattern recognition has been performed, each track candidate is confined within a road and hit coordinates can be referred to the SuperStrips edge ($\vec{x_0}$); equation 4.1 becomes:

$$P_{0j} + \delta P_j = \vec{F_j} \cdot (\vec{x_0} + \delta\vec{x}) + Q_j \tag{4.2}$$

where, $P_{0j} = \vec{F_j} \cdot \vec{x_0} + Q_j$ is a constant which depends on the road, while δP_j is the correction which depends on the precise hit positions inside the road. The P_{0j} coefficients which correspond to the track lying exactly on the road edge, are calculated in advance and stored in RAMs. Therefore the track fitting task reduces to a fast computation of simple scalar products (done by FPGA chips):

$$\delta P_j = \vec{F_j} \cdot \delta\vec{x} \tag{4.3}$$

The output list of high precision tracks is sent to the global level 2 processor for the final trigger decision. SVT is made by over one hundred VME boards housed in 8 crates. The installation has been completed and the system has been fully operational since the beginning of 2001.

4.3 SVT commissioning

The first evidence that SVT finds good tracks is the plot of the correlation between the impact parameter d and the azimuthal angle Φ in a sample of candidate tracks (see figure 4.1 up left). If the position of the interaction vertex in the transverse plane is (x_0, y_0), displaced from the nominal one (0,0), the relationship between d and Φ for primary tracks is:

$$d = -x_0 sin\Phi + y_0 cos\Phi \tag{4.4}$$

A t of the $d - \Phi$ scatter plot measures the (x_0, y_0) coordinates with an accuracy of few microns. A beam displacement of fewmillimetres is the present typical running condition for CDF. This is a potential problem because unphysical large impact parameters erroneously affect the level 2 trigger decision. The problem has been

solved in the following way: a process running on one of the SVT VME crate controllers performs the fit of the $d-\Phi$ correlation of the SVT tracks independently, for tracks in each one of the six SVXII $z-$barrels. The beam offset is subtracted online:

$$d' = d + x_0 sin\Phi - y_0 cos\Phi \tag{4.5}$$

and physical impact parameters, measured with respect to the actual beam position, are actually output by the SVT. Figure 4.1 illustrates the effect of beam offset subtraction (down left) and the online d' distribution (right). The gaussian shape and the width of the d' distribution originate from the convolution of the actual transverse beam profile with the impact parameter (I.P.) resolution. A gaussian fit gives: $\sigma \simeq 69\mu$m.

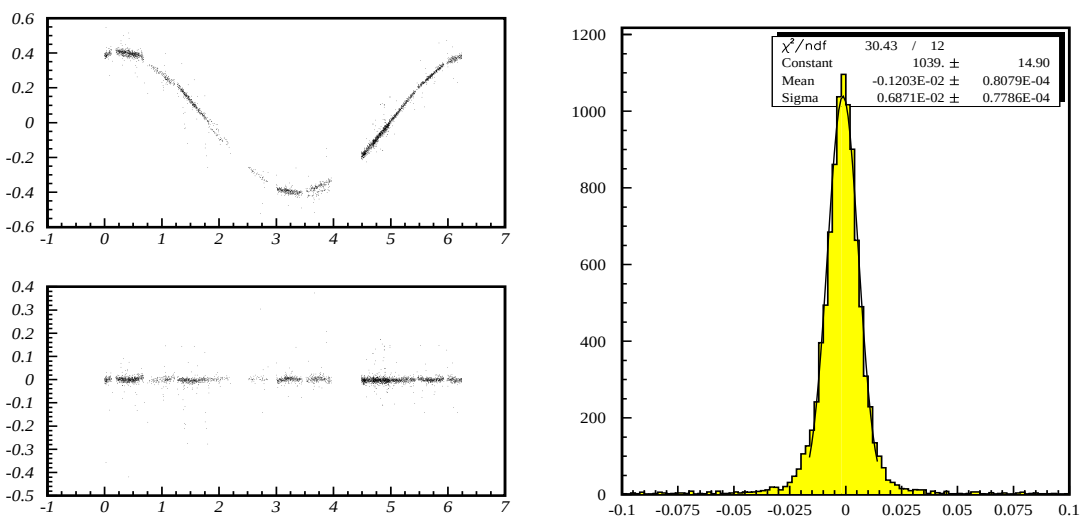

Figure 4.1: Left: $d-\Phi$ correlation for SVT tracks before (top) and after (bottom) correcting for the beam offset. The measured beam position in the transverse plane is $x_0 = 0,0995$ cm and $y_0 = -0.3895$ cm with aprecision of $\sim 3\mu$m. The regions without points are due to missing SVXII wedges. The scale on the x axes is radians, the scale on the y axes is cm. Right: Distribution of the online impact parameter (in cm) corrected for the beam offset.

A big effort has been put in understanding the various factors contributing to the impact parameter resolution with the aim of possibly improving it. In fact, as the resolution degrades the trigger rate increases and the background contamination

in the data samples selected by impact parameter cuts is larger. The potentially most relevant contribution to the impact parameter resolution arises from the $z-$tilt of the beam with respect to the detector. The effect of a z-misalignment ($m_x = \delta x/\delta z, m_y = \delta y/\delta z$) shows up as a residual Φ modulation in the impact parameter after correcting it for the beam offset:

$$d' = -m_x z_0 sin\Phi + m_y z_0 cos\Phi \tag{4.6}$$

where z_0 is the $z-$coordinate of the point of closest approach of the particle trajectory to the $z-$axis. Since SVT does not measure z_0, a beam tilt along z results in an irreducible widening of the impact parameter distribution. In order to make this spread small compared to the natural beam width, SVT requires the detectors and the beam line to be all parallel within 100 μrad. Assembly of the SVXII barrels met (even exceeded) this specification, the z-alignment of the beam orbit is unfortunately more challenging. During the April-October 2001 CDF commissioning data taking the beam slope was found to be significantly large: $m_x \simeq 600\mu$rad, $m_y \simeq 100\mu$rad, well beyond the SVT specifications.

The effect of the $z-$misalignment on the impact parameter distribution was estimated using data of a special run taken with an approximately null beam tilt. A gaussian fit to the online impact parameter distribution gives $\sigma \simeq 59\mu$m.

In addition to the beam tilt, there are two more major contributions to the impact parameter resolution. One is the relative misalignment of the SVXII wedges. This can be easily corrected by performing the beam offset fit and subtraction independently in each wedge. The size of this correction to I.P. resolution is approximately 6 μm. The second major contribution to I.P. resolution is a consequence of the linear approximation used in the SVT track fitting method, which assumes a first order power expansion centered on the nominal beam position. Since during the April-October 2001 data taking the beam was very far from its nominal position ($\sim$ 4 mm away) the effect of non linearity was significantly large: it degraded I.P. resolution by approximately 5 μm. This effect can be corrected in two steps: first the fit

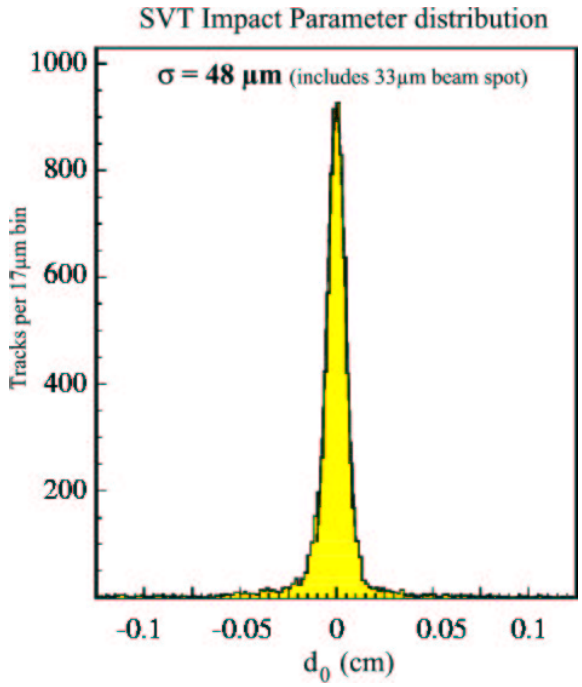

Figure 4.2: Distribution of SVT measured impact parameter in a 2001 run (n.127844), in a single wedge (b3, w3), after subtracting the beam position. There are no corrections for internal detector misalignments.

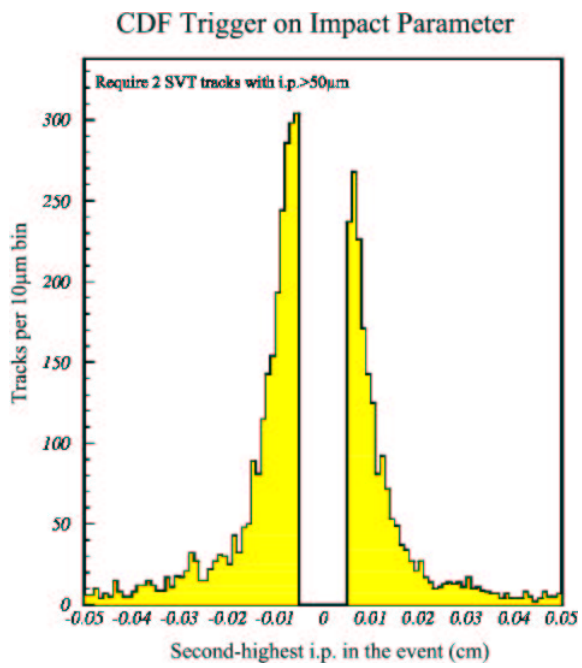

Figure 4.3: The trigger in 2001 commisioning run 127562 required at least two tracks with I.P. greater than 50 μm. This is the distribution of the second-highest I.P. in each event

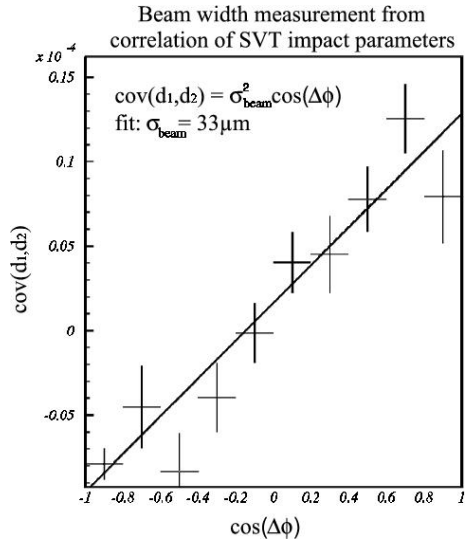

Figure 4.4: There are two primary contributions to the impact parameter resolution: the Tevatron beam width and the SVT resolution. These two contributions can be disentangled in real data. This plot shows the impact parameters correlation vs $\Delta\phi$ which is proportional to σ_{beam}. Fitting the plot gives a Tevatron beam width of $\sigma_{beam} \simeq 33\mu$m; this number, combined with the 48 μm above yields an estimated SVT impact parameter resolution of $\sim 35\mu$m.

constants in equation 4.2 are recalculated centered on the measured beam position; second, the beam position fit is done on each wedge separately using a linear $d - \Phi$ relationship. With these corrections applied the impact parameter distribution was found to have a gaussian shape with a sigma of 48 μm in a run taken with the beam aligned in the z direction, I.P. distribution shown in figure **??**. All these corrections can be implemented in the SVT and applied online. But the best SVT performance relies on the accelerator capability to provide an alligned beam.

Using a sample of events in which at least two good ($\chi^2 < 10$) SVT tracks were found we have been able to calculate the true beam transverse size (σ_B). The result of this study for a run with negligible beam tilt is $\sigma_B = 33 \pm 1\mu$m (see figure **??**). Deconvolving this beam width from the above 48 μm we obtain $\sigma(d) \simeq 35\mu$m for the SVT I.P. resolution, in agreement with the design value.

In October 2001 the first trigger tests using SVT have been done. A Level 2 trigger was implemented requiring at least 2 SVT tracks with $\chi^2 < 25$, $p_T > 2$

GeV/c, $|d| > 50\mu$m and a Level 1 prerequisite of at least 2 XFT tracks. Figure 4.3 shows the distribution of the second largest impact parameter in the event. The early analysis on those data is described in detail in chapter 6, section 6.3 where first heavy flavour signal $D^0 \to K\pi$ from SVT data was extracted.

4.4 Two track hadronic trigger

The two track trigger is a combination of Level 1 and Level 2 requests. Level 1 request are operated on the Extremely Fast Tracker (XFT) tracks based on Fast COT tracking, the standard **Level 1** cuts are:

- Each track has $p_T > 2$ GeV.
- The two tracks have opposite charge.
- $p_{T1} + p_{T2} > 5.5$ GeV.
- $\Delta\Phi < 135^o$.

XFT Level 1 tracking has a measured track finding efficiency of more than 95 % for $p_T > 2$ GeV/c and a p_T resolution of $\Delta p_T/p_T^2 = 1.65\%$ GeV/c as it is shown in figure 4.5.

As described in previous section XFT information is used as an input to SVT Level 2 processing. SVT selection was designed to reduce the trigger rate coming from Level 1 to an acceptable value without loosing all the long lived heavy flavour signal. In particular the so called **"Two-body"** SVT trigger path was optimized to trigger on $B \to \pi\pi$ decays in which, given the $p_T(B)$ spectrum and the B life-time, the daughter particle tracks have an impact parameter of the order of 100 μm. The two tracks are also expected not likely to be back to back. The **"Multibody"** SVT trigger path, is optimized for B decays to more than two body. These are the main trigger paths with which SVT is operating at present conditions, the **Level 2** two track trigger cuts are listed in table 4.1. SVT trigger most important selection is

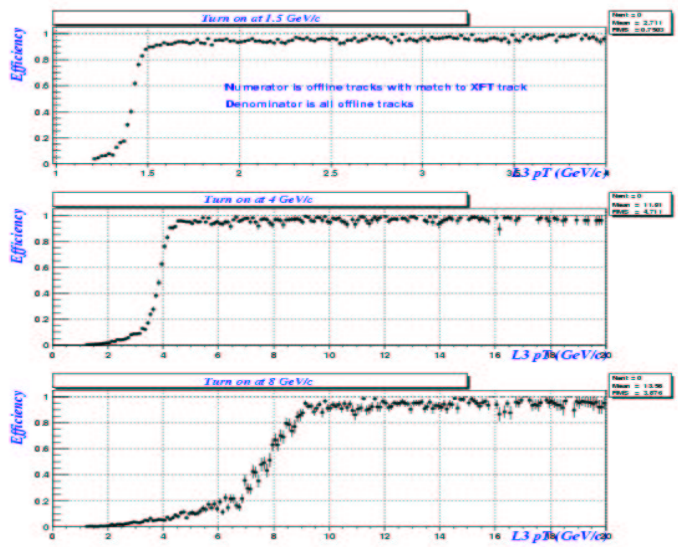

Figure 4.5: The three plots show the efficiency versus momentum of the XFT for three different momentum thresholds: 1.5 GeV/c, 4.0 GeV/c and 8.0 GeV/c. The shape of the turn-on provides a measure of the XFT momentum resolution. The momentum resolution is measured to be $\Delta p_T/p_T^2 = 1.65\%$ GeV/c, which is better than the 2 % GeV/c specified in the Run II TDR. The angular resolution is measured to be 5.1 mrad, better than the specified 8 mrad resolution specified in the TDR.

operated on the impact parameter (d_0) of the tracks after that Level 1 requests for two track trigger have been confirmed at Level 2.

Two Body ($B \to \pi\pi$)	Multybody (B_s)
L1 cuts confirm	L1 cuts confirm
$100\mu m < \|d_0\| < 1mm$	$120\mu m < \|d_0\| < 1mm$
$20^o < \Delta\Phi < 135^o$	$2^o < \Delta\Phi < 90^o$
$d_0(B) < 140\mu m$	–

Table 4.1: Cuts applied in the Level 2 SVT trigger paths, the Two track trigger is the "OR" of the two paths.

The SVT tracking efficiency, depending on the optimization of operating conditions described in previous sections, have been measured by matching SVT trigger tracks with off-line tracking. Results for the data which have been used for the measurement presented in this thesis are given in section 7.2, while very recent upgrade of this optimization is reported in section 8.2.

In order to give a qualitative idea of the SVT capabilities in the selection of tracks coming from long lived particle decays, we report here a study on $K_s \to \pi\pi$ decays which have been reconstructed with pairs of SVT tracks satisfying trigger conditions. Figure 4.6 shows the K_s peak when the quantity $L_{xy} = \vec{X_V} \cdot \vec{P_T}(K_s)$ is positive or negative, where X_V is the K_s vertex distance (in the transverse plane) from the primary vertex. In the first case ($L_{xy} > 500\mu$m) the "forward-going" tracks are selected showing a clear peak, while in the second case ($L_{xy} < -500\mu$m) "backward" tracks, constituting non-peaked background, are selected.

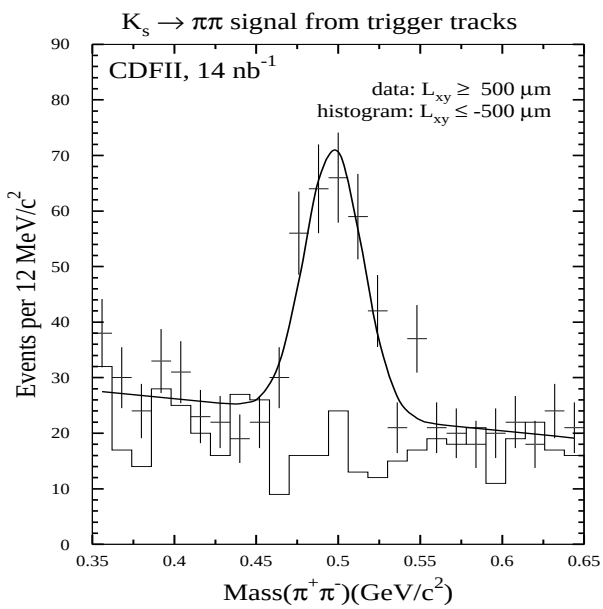

Figure 4.6: A clear K_s peak is visible at positive L_{xy} while for negative values of the transverse decay distance projected on the K_s flight direction no signal is present. It can be noted that despite the high K_s production the SVT intrisic limitation for $d_0 < 2$ mm, reduces the acceptance to K_s. This study has been done on the october 2001 SVT commissioning runs.

At **Level 3**, for the two track trigger, the confirmation of Level 2 cuts with better tracking is required to clean up the sample. In particular the matching between the two SVT trigger tracks and the corresponding Level 3 COT tracks is required in terms of azimuthal angle Φ, curvature and χ^2. A cut on the forward-going vertex variable $\vec{X_V} \cdot \vec{P_T}$ is also done, requiring it to be positive or even greater than some optimized value at which heavy flavour signal selection efficiency is not affected, like

200 μm.

At present conditions, as shown in section 3.1, CDF is tacking data at Luminosity of few units in 10^{31}. With the cuts given above the Level 1 rate is $\sim$ 3 KHz and the Level 2 rate is $\sim$ 50 Hz for the Two track trigger. At Level 3 the hadronic two track trigger send events to the DAQ system at a rate of $\sim$ 1 Hz. For higher Luminosities, some possible trigger scenarios have been studied; the main lever arm to control the trigger cross section will be to rise up the cuts on the transverse momenta.

Chapter 5

Particle identification and flavour tagging at CDF

Particle identification at CDF is based on two indipendent measurements on charged particle tracks: the dE/dx energy loss by ionization measured in the drift gas chamber COT, and the Time of Flight of the particles measured in the new "ad hoc" detector inserted between the COT and the solenoid.

Here we describe the CDF potential in particle identification given by this two methods; more details are given about TOF detector.

We do not discuss here, the CDF lepton identification which is based on a complex of shielding material and sensitive chambers in the external part of CDF for muons and on electromagnetic calorimeter for electron. These devices are shortly described respectively in sections 3.7 and 3.6.

At the end of this chapter, in section 5.5, we give a description of "Flavour tagging" techniques, based on dE/dx and TOF particle identification, which will be implemented at CDF in order to extend B-flavour CDF capabilities.

5.1 dE/dx from the drift chamber

The average total energy loss per unit lenght dE/dx can be described by the famous Bethe-Bloch formula:

$$\frac{dE}{dx} = \frac{4\pi N e^4}{mc^2\beta^2} z^2 (ln \frac{2mc^2\beta^2\gamma^2}{I} - \beta^2) \tag{5.1}$$

Apart from details which can be found in literature (for example [**?**]), we want to underline here that dE/dx depends on the medium parameters like Ionization potential I, density of electrons to which N (or Z) is proportional, and particle velocity β. It is then clear that through momentum measurement, dE/dx is a tool for particle (mass) identification.

In the case of COT the medium is the gas mixture (see section 3.4) and the measurement of dE/dx for a reconstructed track is operated through the measure of the charge collected by the COT sense wires along the track. A charged particle ionising the COT gas leaves ion-electron pairs along the track path in the cell, the number of this pairs, then drifting to field wires of the cell, is proportional to specific ionization of the particle. The electrons arriving to the anode wire after multiplication given by gas gain at operating High Voltage, forms the signal pulse used for tracking. The deposited charge of this signal is in principle proportional (if the gain regime is so) to the energy loss by ionization of the charged particle.

The analog signal of each sense wire is readout by an $ASDQ$ (Amplifier, Shaper, Discriminator and Charge) circuit which is embedded in the COT front-end electronics. The output of this circuit is a digital pulse whose leading edge gives the timing information and whose width is related to the amount of charge collected by the wire. A charged particle track can have up to 96 hits in the COT cells on which charge is measured; this hits are a sample of dE/dx measurements providing that the appropriate corrections to each hit is properly done. Examples of this corrections, for quantities that affects the dE/dx measurement are: the angle between the track and the drift field, the z position along the wire, correction for gas pressure in the chamber, etc. Basically, the charge deposit has to be normalized to the effective path of charged track in the cell which depends on the crossing angle, the position along the cell and the cell form. Other corrections depends on gas gain differences coming for example from High Voltage settings.

Once this corrections are done, it will be possible to have a K/π statistical separation power of 1.3 σ for $p_T > 2$ GeV with dE/dx. Expected separation power

from dE/dx measurement as a function of p_T is shown in figure 5.1, togheter with the TOF expectations. The particle identification through dE/dx is in its testing phase at this moment, preliminary results are expected soon. All along this thesis, dE/dx has not been used.

5.2 The Time Of Flight detector

Following the successful RunI from 1992 to 1996, the CDF detector has undergone a major upgrade [25] for the RunII which begun in March 2001. The approval for the addition of a Time-of-Flight detector was granted in January 1999. The installation of the TOF detector was completed in August 2001 and its data has been included in the CDFII readout since then.

The primary physics motivation for TOF is to complement and enhance the particle identification capability provided by the central drift chamber (COT) since it distinguishes $K^{\pm}$ and $\pi^{\pm}$ in the momentum region of their cross-over in dE/dX. With a design time-of-flight resolution of 100 ps, the TOF system will be capable of identifying charged kaons from pions by their flight time difference with at least two standard deviation separation up to kaon momenta of 1.6 GeV/c. Such an addition results in an enhancement of the b flavor identification power, crucial to improve the statistical precision in CP violation and B_s mixing measurements.

Particle identification with TOF is performed by measuring the time of arrival of a particle at the scintillator with respect to the collision time t_0. The particle mass m can then be determined from the momentum p, the path-length L, measured by the tracking system, and the time-of-flight t measured by the TOF:

$$m = \frac{p}{c}\sqrt{\frac{c^2t^2}{L^2} - 1} \tag{5.2}$$

In figure 5.1 are shown the time-of-flight difference between K/π, p/K and p/π and the separation power assuming a resolution of 100 ps. The TOF improves the K/π separation in the momentum region of $p < 1.6$ Gev/c by 2σ or better.

The CDFII TOF detector [29],[30], consists of 216 bars (279 cm long and with a

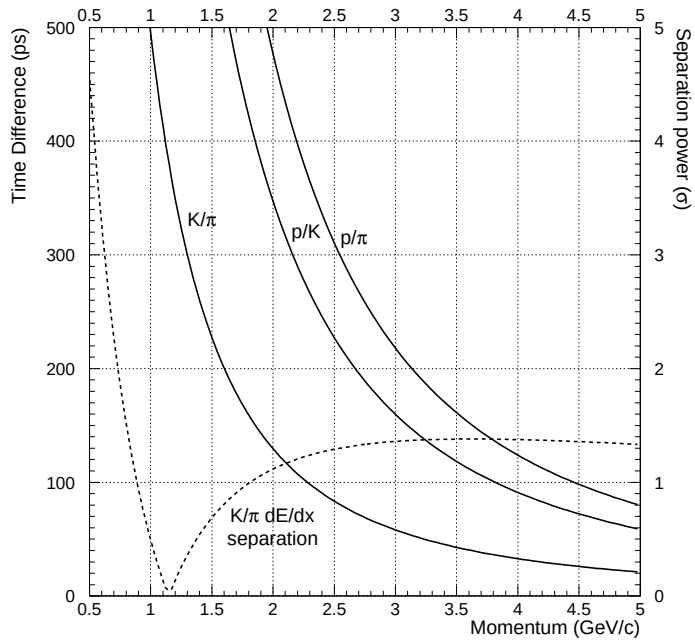

Figure 5.1: $K/\pi, p/\pi$ and K/p time difference as a function of momentum over a path of 140 cm, expressed in ps and separation power, assuming a resolution of 100 ps. The dashed line shows the K/π separation power from dE/dX measurement in the COT.

square section of about $4 \times 4cm^2$) of Bicron BC-408 plastic scintillator. The bars are installed at a radius of $\sim$ 138 cm from the beam line in the 4.7 cm of radial space available between the cylindrical outer wall of the central drift chamber (COT) and the inner wall of the cryostat of the super-conducting solenoid, covering a pseudo-rapidity region of roughly $|\eta| < 1$.

A nineteen-stage fine mesh photomultiplier tube (PMT), Hamamatsu R7761, with a diameter of 1.5 inches is attached to each bar end, for a total of 432 PMTs in the system. These operate in the 1.4 Tesla solenoidal magnetic field with an average gain reduction of 500 from the nominal gain of 10^6. The optical connection between the PMT and the scintillator is provided by a compound parabolic concentrator. The PMT in turn is directly attached to a custom designed HV divider base which also connects to a preamplifier card for the readout. A schematic view of a TOF bar can be seen in figure 5.2.

Differential signal from the anode and the last dynode of the PMT is fed to the preamplifier, and drives, over $\sim$ 12 m of shielded twisted pair cable, front-

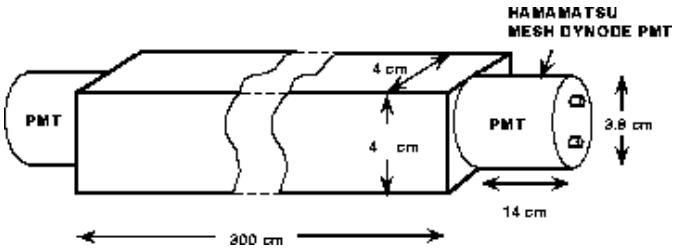

Figure 5.2:

end electronics that reside in a VME crate mounted outside the detector. A block diagram of TOF front-end is given in figure 5.3. The front-end signal is split into two: one for timing measurement and the other for pulse height measurement. The timing

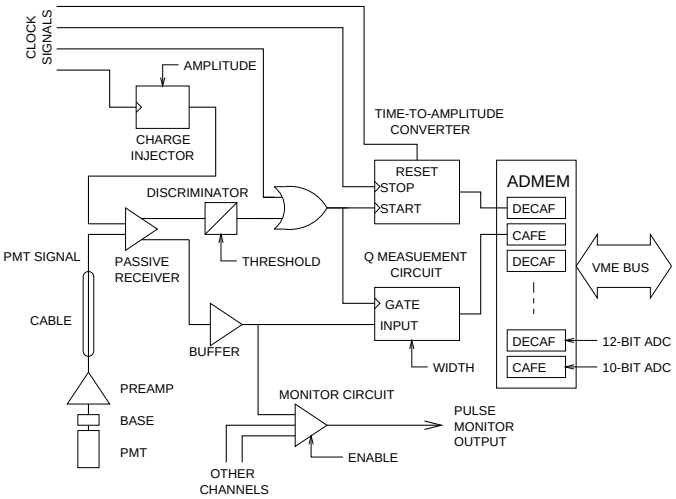

Figure 5.3:

path enters a leading edge discriminator with an adjustable threshold, whose output serves as the start signal for the Time-to-Amplitude Conversion (TAC) circuit [31]. The TAC ramp is terminated by a common stop clock edge, that is synchronized with the $p\bar{p}$ bunch crossing, and fanned out to all electronics channels with a designed jitter of less than 25 ps. The voltage output from the TAC is sampled by a 12-bit ADC, characterized by a least count of roughly 17 ps over a dynamic range of about 60 ns. TAC response has shown an excellent stability since the commissioning of the electronics, with a residual variation, after the calibrations, of less than 17 ps.

The primary purpose for measuring the charge of PMT signals is to perform a

correction for the dependence of the discriminator on signal amplitude. The charge measurement is done by a charge sensitive ADC [31]. The current driver is switched on by a gate of adjustable width, and is initiated by the discriminator output, so that only the charge due to the pulse that fired the discriminator is integrated.

5.3 TOF calibration

The output of the TDC is in principle a linear function of the time difference between the start, in each TDC channel, and the common stop. Since non linearities have been observed, an on-line channel by channel calibration is performed by sending a series of pulses, with known time differences w.r.t. common stop, from a digital delay generator. Moreover, due to cross-talks with the TAC, the ADC pedestals can exibit a time dependent shift. This is also taken into account in the on-line TOF calibration which is embedded in the CDF data aquisition system [**?**].

Being time of flight measurement possible through the external COT tracking system, a finer calibration of TOF response is performed off-line with the use of reconstructed tracks.

It is necessary for the TOF system to be aligned with respect to COT in order to extrapolate correctly the tracks to the corresponding hitted TOF bar(s). To ensure this a geometrical photogrammetric survey was performed on TOF bars positions after detector installation. The positions of the bars in the transverse plane i.e. in the Φ angle were also measured independently with the COT tracks. By looking to raw TDC and ADC data an hitted TOF bar was defined so if the two PMT had fired and if the ADC signal were significantly over the pedestal values; the Φ position of the bar was defined as the Φ corresponding to the bar center as measured in the survey.

COT tracks were selected, extrapolating them to the TOF and requiring them to match an hitted bar; Φ from those tracks were calculated at TOF mean radius.

The result of this study, shown in figure 5.4, allowed a finer TOF geometrical

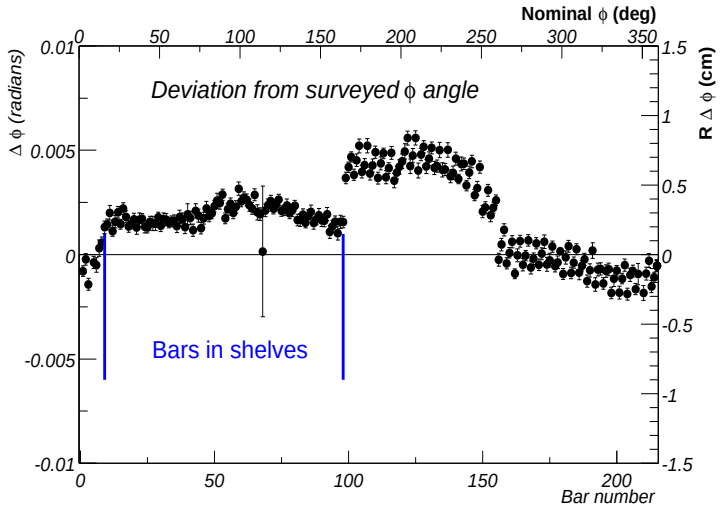

Figure 5.4: Difference in Φ-angle of the bars from survey an that measured by the COT tracks.

model correction to be implemented. This correction is taken into account in the following.

The time at which a PMT pulse is registered after the nominal $p\bar{p}$ bunch crossing time, can be modeled in the general from:

$$t = c + t_0 + tof + (L/2 \pm z)/s - S(Q) \tag{5.3}$$

where c is a constant offset describing the propagation delays in the cables, t_0 represents the time at which the $p\bar{p}$ interaction occurred, tof is the particle's time-of-flight, the bar of scintillator length is L, s is the effective speed of light in the scintillator, and the last term describes the time-walk effect introduced by the leading edge discriminator i.e. the measured time dependence on the charge Q. The z coordinate is measured along the length of the bar by the tracking chamber, the positive and negative sign of the term proportional to z corresponds to a PMT in the west or east end of the detector, respectively.

However these terms are not completely independent since the average charge measured depends on the z coordinate of the track due to the finite attenuation lenght of the bar scintillator material, see figure 5.5. This effect can introduce a correlation between the "velocity" and the $S(Q)$ terms in equation 5.3.

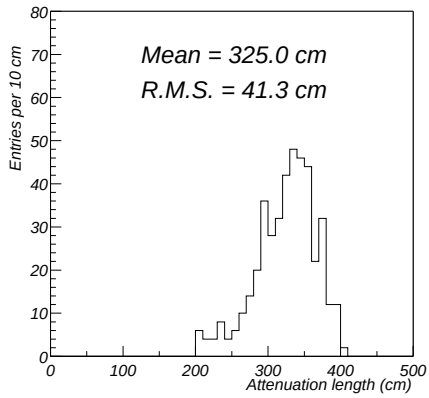

Figure 5.5:

When a single charged particle enters a bar, the time difference between signals reaching the east and west ends is essentially a linear function of the track entrance point along the bar, z. A typical distribution of the time difference plotted as a function of z is shown in Figure 5.6. The effective speed of light in the bar can be derived from the fitted slope. From the distribution of the residuals of this fit a

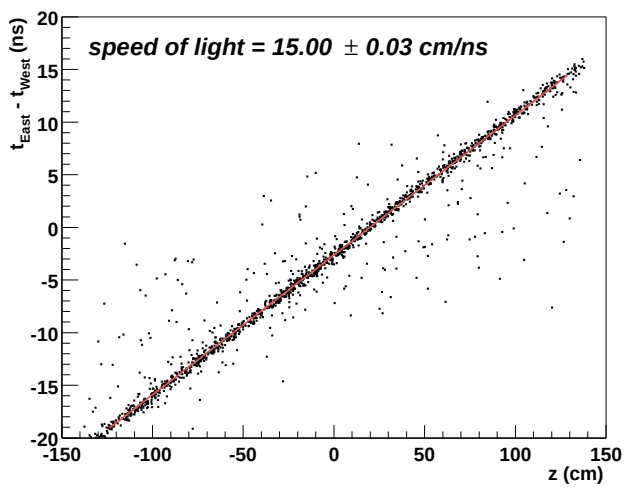

Figure 5.6: Distribution of the time difference, $t_{east} - t_{west}$, plotted versus the entrance point, z of a track. The scattered points far away from the fitted line are due to multiple tracks hitting the bar.

first indication of the timing resolution of each PMT, can be obtained. This rough indicator of the time difference resolution averaged over all bars is typically 250 ps or better. This is larger by approximately a factor two than the resolution of a mean

time measurement, indicating that the TOF resolution is not far from our design goals. Since systematics effects can cancel in the time difference measurement, this estimate represents only an indication of the capabilities of the TOF detector. The ADC response was studied with a sample of tracks, matching hitted TOF bars, corrected for the path done in the scintillator, as a function of the z position. The main dependence on z, is exponential and gives as a result the attenuation lenghts shown in figure 5.5. An additional exponential dependence on z^2, probably due to reflections at the bar ends, gives a correct description of $Q(z)$ shown in figure 5.7 The dependence of the pulse height on the measured time and the parameterization

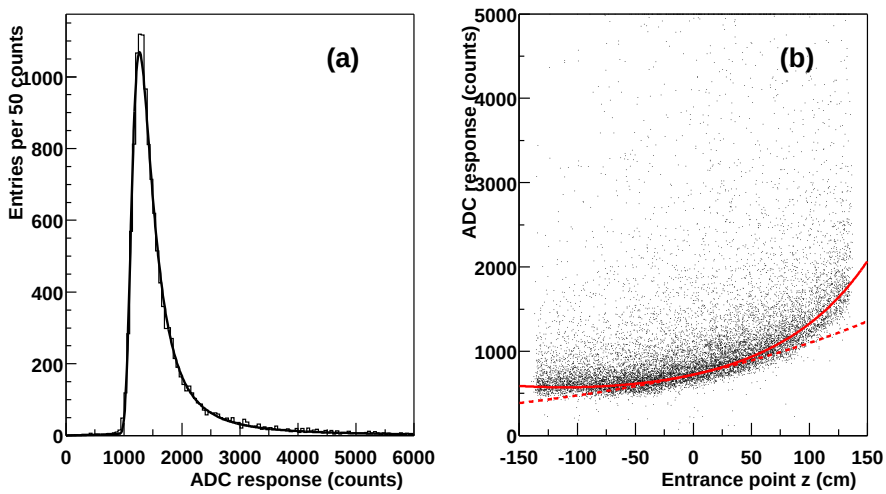

Figure 5.7: ADC response for TOF channel 53, in store 860 (december 2001), which has a large z^2 attenuation component (right). Charge distribution is fitted by a Landau function (left).

of the time slewing (or time walk correction) effect $S(Q)$ (in equation 5.3) have been studied using a sample where each track passes through two adjacent bars of scintillator. Depending on the path length in each bar, a range of ADC responses is obtained on the two channels at the same end of the bar and at the same time, since the track entrance point in each bar is similar and anyway under the TOF resolution power. Time walk $S(Q)$ has been parametrized in a second order polinomial in the variable $log(Q/Q(z))$ which are adapted to the description of correlation between the

amount of light generated by a track and the time (i.e. z) at which the discriminator fires.

The time difference between the two channels depends mainly on time walk effects. Due to finite attenuation length in the bars ($\sim$ 325 cm) the pulse height depends on the entrance point of the track, z. For this reason the slewing correction introduces a linear dependence in the time difference $T_{east} - T_{west}$ versus z, resulting in a biased effective speed of light determination. After the time slewing correction the width of the speed of light distribution for all the PMTs is significantly reduced (figure 5.8, right) and observed low-side tail in the distribution in figure 5.8 (left) disappeared.

Constant term c in equation 5.3 was studied in the $T_{east} - T_{west}$ offsets on a bar by bar basis.

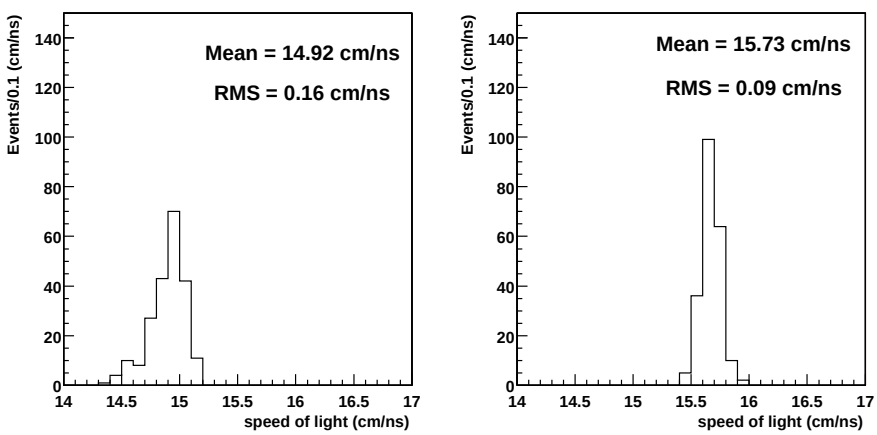

Figure 5.8: Speed of light is measured from slope of $T_{east} - T_{west}$ vs z. Left plot is without applying a walk correction while the right plot is with a walk correction applied

5.4 TOF resolution

Applying the calibrations explained in previous section the time of flight of a particle can be measured. The production time t_0 (in equation 5.3) of the tracks in an event can be measured accurately using the reconstructed tracks provided the

multiplicity of the primary vertex is high enough. Figure 5.9 shows the possibility of the TOF in discriminating between 3 superimposed interactions in the same bunch crossing. each interaction has a multiplicity of charged tracks around ten.

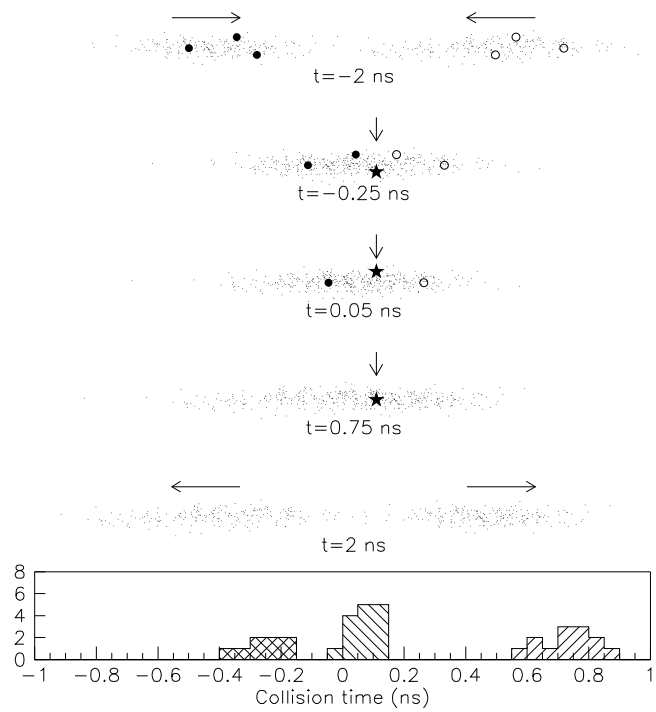

Figure 5.9: This plot shows how three interactions can happen at the same point in z and yet still be identified as being distinct using TOF. 2 ns is the typical bunch crossing time spread.

The resulting uncertainty on t_0 scales with $1/N_{tracks}$ so t_0 can be measured with a resolution smaller than that on the Time of flight on a single track. The t_0 measurement is operated by reconstructing the primary vertex with the tracks and measuring the TOF of all tracks in the event with particle mass hypothesis weighted with the expected particle relative fractions (mostly pions).

After all calibrations, corrections and event t_0 measurement were done, the timing resolution of a given channel can be estimated by comparing the measured TOF for a track with the expected TOF under the pion mass hypothesis Figure 5.10 shows the distribution of the resolution obtained with this procedure. It shows a mean value of 110 ps with an RMS of 15 ps, which is already very close to the design goals.

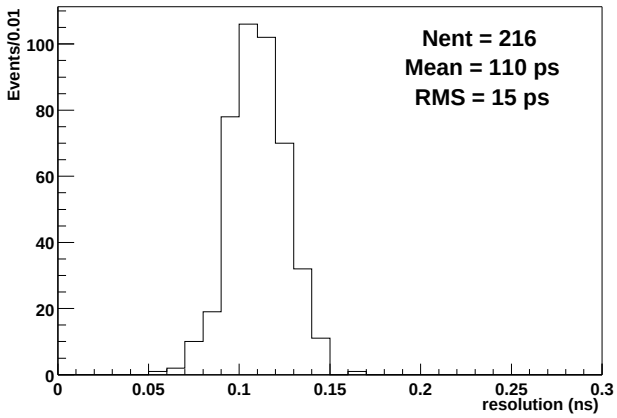

Figure 5.10: Time-of-flight resolution (at the PMT face) for all bars of the CDFII TOF detector.

In figure 5.11 the mass-momentum scatter plot computed using eq. 5.2 for low momentum tracks, is shown. Three clear "clouds" corresponding to pions, kaons and protons can be seen.

Actual realistic performance of the entire TOF system can be obtained by analyzing the $\phi \rightarrow K^+K^-$ signal in a sample of events recorded by CDFII. The ϕ candidates are selected from all pairs of oppositely charged tracks by assuming the kaon masses, with the only constraint that the two tracks originated from the same vertex. Both tracks are required to have a transverse momentum less than 1.5 GeV/c and valid reconstructed TOF informations. Figure 5.12 shows the invariant mass distributions obtained before and after applying TOF kaons particle identification. A clear signal peak in the distribution appears in the latter case, corresponding to a factor 20 background reduction and 80% signal efficiency [33].

5.5 Perspectives for flavour tagging

The primary purpose of the TOF detector is to identify charged pions, kaons and protons. In the context of B physics, particle identification is useful both for reconstructing B decays and for b flavor tagging. In particular the CDF TOF detector was designed to substantially improve the statistical precision in the measurement

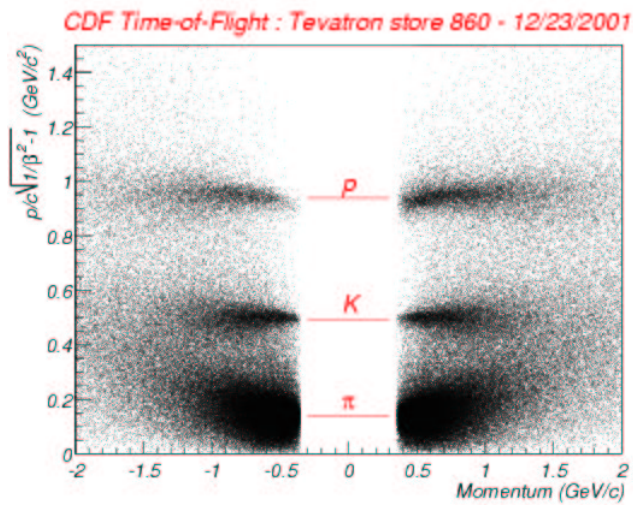

Figure 5.11: TOF reconstructed mass versus momentum for positive and negative tracks. The three horizontal lines correspond to nominal p, K and π masses.

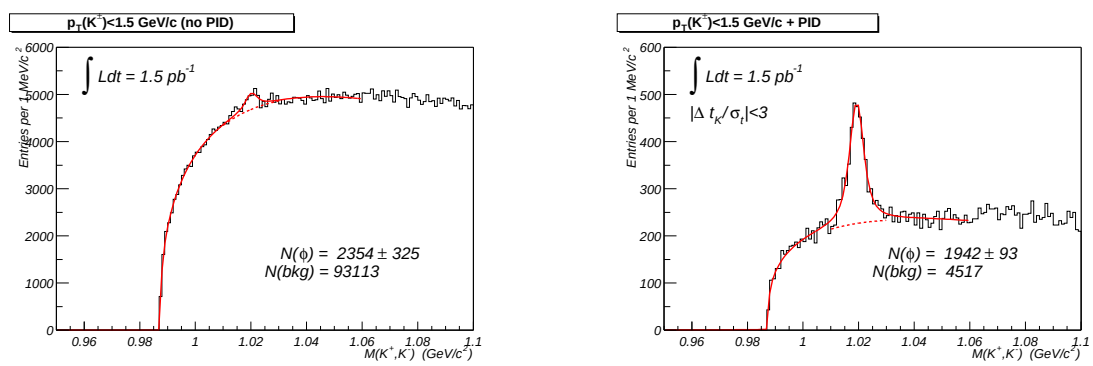

Figure 5.12: K^+K^- invariant mass distribution for $p_T(K^\pm) < 1.5\ GeV/c$, without (left) and with (right) TOF particle ID.

of CP violation, as well as the sensitivity in measuring B_S^0 oscillations.

By the term "b flavour tagging" we mean the ensemble of procedures and algorithms which act to determine the flavour of the B meson when it was produced. The figure of merit for a b flavour tagging method is its "total tagging effectiveness", ϵD^2. The efficiency ϵ accounts for the fact that we can apply a flavour tag only to a fraction $(0, 1)$ of the B candidates. The dilution D is related to the fact that sometime the obtained tag is wrong. If we call P the probability that the tag is correct, the dilution is then defined as $D = 2P - 1$, so for a perfect tag we will have $D = 1$, and for a random tag $D = 0$. The total tagging effectiveness ϵD^2 determines the

effective statistical power of the sample, so that, for example, the statistical error on the determination of a CP asymmetry A with N total candidates is proportional to $\delta A \sim \sqrt{\frac{1}{\epsilon D^2 N}}$. An additional flavour tagging method that would increases ϵD^2 by a factor of two would lead to a reduced statistical error on A by $\sqrt{2}$.

The methods of b flavour tagging can be divided in two categories: "opposite-side" tagging (OST) and the "same-side" tagging (SST). The former relays on the fact that the dominant production mechanism of b quarks in hadron collisions generates $b\bar{b}$ pairs. To identify the flavour of a reconstructed B meson of interest, we identify the flavour of the second B hadron in the event and infer the flavour at production of the primary one. The same-side flavour tag exploits instead the correlation between b flavour and the charge of the particles accompanying the reconstructed B. In particular, a π^+ is expected to be produced in association with a B^0 meson, and a π^- with a $\bar{B}^0$.

The CDFII TOF can be used to enhance both opposite-side and same-side b flavour tagging. The decays of $\bar{B}$ hadrons will contain more likely a K^- than a K^+ in the final state due to $b \to c \to s$ week decays. Therefore identifying a charged kaon from the B-decay can be used as an opposite-side b flavour tag. In Figure 5.13 the Montecarlo momentum spectrum of kaons from the opposite-side B decay to the $B^0/\bar{B}^0 \to J/\psi K^0_S$ signal is shown. More than 50% of the available kaons are in a momentum range where the CDFII TOF can give a 2σ separation power from charged pions. The CDFII potential for the opposite-side flavour kaon tag using the TOF has been estimated with a Montecarlo simulation, assuming the design resolution of 100 ps. This gave $\epsilon D^2 = (2.4 \pm 0.2)\%$, which is more than a factor two higher than the typical values obtained in RunI.

The TOF can be used for same-side tagging as well. In the hadronization process when a B^0_S meson is produced an $s\bar{s}$ pair must be popped from the vacuum during fragmentation. The remaining s or $\bar{s}$ quark can join a $\bar{u}$ or u quark to form a charged kaon. The charge of the kaon thus depends on the flavour of the B^0_S meson at production. A factor four increase on ϵD^2 has been obtained, using Montecarlo

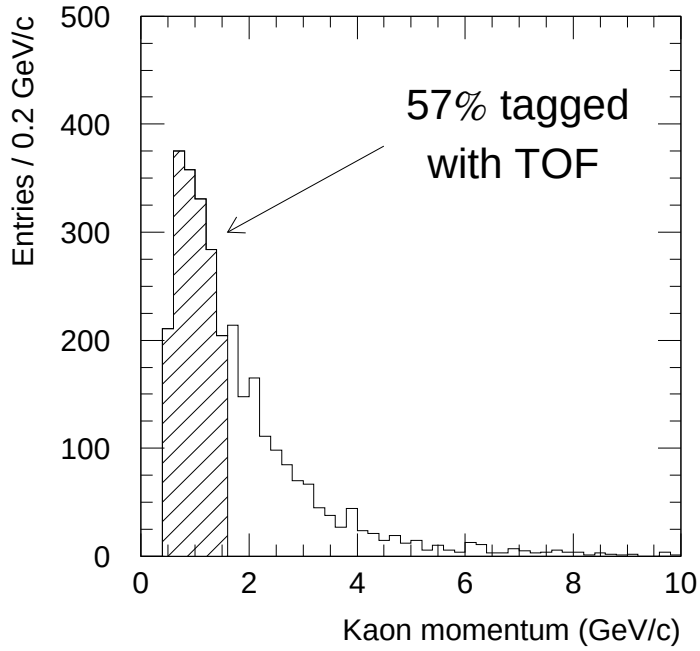

Figure 5.13: Momentum spectrum of kaons from B decay opposite to reconstructed $B^0 \to J/\psi K_S^0$ decay obtained from Montecarlo simulation. The region at $p < 1.6\ GeV/c$, for which a 100 ps TOF resolution yields a better than 2σ $K - \pi$ separation, is hatched.

simulations, for same-side tagging of B_S^0 using TOF informations (from 1.0% to 4.2%).

Combining all the b flavour tag methods available in RunII, CDFII has estimated a total ϵD^2 of 11.3% for B_S^0 mesons using TOF for particle identification. This large effectiveness will greatly increase the sensitivity for the measurement of the B_S mixing parameter x_S, one of the unique measurement of Tevatron during the RunII, see discussion in section 8.5.

Chapter 6

Heavy mesons reconstruction in the SVT trigger sample

6.1 Introduction

Tacking into account the large fraction of B mesons decaying to D's, $B \rightarrow D + anything$ ($\sim$ 99 %), the role of finding the D mesons in the generic event is to be the first step for most of B mesons channels analysis.

In particular we think here about mainstreams in B physics like B_s mesons mixing requiring, as described in previous chapters, a very good decay time resolution for the high oscillation frequency they have. Hence, completely reconstructed decays like pure hadronic ones are the best sample for mixing measurements. These decays for B_s tipically involves a D_s in the final state. For $B_{d,u}$, D^0 D^* $D^{\pm}$ are typically concerned.

The charmed meson selections is then fundamental step to work on charm physics. In particular, given the new two track trigger, it is possible to trigger and select directly on pure hadronic D mesons decays, which are relevant for the study of CP violation in charm sector as will be discussed in detail in the next chapters.

The studies presented in this chapter have been done in order to have for CDF a selected sample enriched in D mesons; in particular working on the events selected by SVT. Preliminary studies on generated heavy flavour events passing the trigger requirements have been done on Montecarlo to optimize the selection criteria (see

6.2). The optimization have been developped initially for the very probable decay in two track $D^0 \to K\pi$, which has been the first heavy flavour signal extracted from new CDF SVT hadronic trigger since the very first commissioning runs in fall 2001 (see section 6.3).

For this purpose a "fast" simulation of the detector and of the two track trigger has been used (section 6.2) as long as it reproduces the basic kinematical biases and features that are relevant to implement an optimized D meson selection. A more detailed simulation composed by full simulation of detector response based on GEANT and a "bit by bit" emulation of the trigger will be used for the measurement presented in this thesis; the full simulation is described in the next chapter as well as a preliminary cross check of it with data.

For the others charmed mesons ($D^*, D^{\pm}, D^s$) reconstructed in this first data tacking period similar studies on Montecarlo have been performed; we report in section 6.4 the signal peaks reconstructed from SVT data.

A preliminary study on data collected by CDF till the summer 2002 that has been performed on the SVT sample to understand its composition in terms of heavy flavour contents using the D mesons reconstructed in this trigger is described in section 6.5.

Finally very preliminary results on the fully hadronic decays of B mesons, triggered by SVT is shown in section 6.6.

6.2 Montecarlo studies

In the perspective of the selection of charmed mesons in the SVT trigger sample, Montecarlo samples of heavy flavours produced in $p\bar{p}$ interacion have been generated and simulated in the detector. Different samples like $b\bar{b}$, $c\bar{c}$ events have been used. In particular the interesting situation that was reproduced was the so called generic $b\bar{b}$ event, in which both b quarks are free to hadronize in the different B mesons or b-hadrons and then decay into every possible final state. The hadronization frac-

tions were taken from best world knoledge PDG as well as for the decay Branching fractions. These inputs for the Montecarlo are all contained in the "QQ" table an upgraded version for CDF of the analog tool used by the CLEO collaboration containing around 400 decays. Specific B decays like $B \to D^0\pi$ have been generated and simulated to study trigger efficiency and biases to the tipical B physics event used for our analysis plans. The detector response and resolution on tracking is taken into account by convoluting track parameters with realistic smearings, this fast detector simulation is then described. The two subdetectors that were relevant in this case are the two components of CDF tracking system: the drift chamber COT and the silicon vertex detector SVXII. For the two track trigger simulation we used a fast parametric simulation GenTrig [38] which starting from generator level final state tracks of the events, operates the principal actions of Level 1 (XFT) and Level 2 (SVT) track trigger. In the following with more detail each of these steps are described, giving at the end the baseline for D mesons selection we agreed in CDF. After this study an official selection software package for the collaboration, named "CharmMods", as been produced as a result [42].

6.2.1 Generators

Basically three generators has been used: Pythia, Bgenerator and FakeEvent. Pythia is a general purpose generator program conceived to produce various kind of events starting from a nucleon-nucleon collision. It takes into account structure functions of colliding hadrons and the more relevant hard scattering processes between quarks and gluons are implemented. We recall flavour creation, flavour ecxitation and gluon splitting as the LO procecesses which as been described in chapter 1 with their different contributions to $b\bar{b}$ production cross section. We used it in order to produce at parton level $b\bar{b}$ and $c\bar{c}$ pairs that are then hadronized following the Lund string model which is embedded in Pythia. B hadrons are then interfaced to the table QQ for decay.

To focus on specific decays another generator tool Bgenerator as been used.

Bgenerator creates a single quark following inclusive transverse momentum distribution $p_T(b)$ from NDE [Nason, Dawson and Ellis] as well as $b\bar{b}$ pairs with spectra coming from MNR [Mangano, Nason, Ridolfi] calculation. In the NDE generator the input to the single quark is a two-dimensional histogram of the correlation between quark transverse momentum and rapidity (y). In the case of MNR generator the inputs are correlation histograms between the two quarks variables p_T, azimuthal angle Φ, and rapidity y.

6.2.2 A generator level trigger simulation

Two track trigger as been simulated with "GenTrig" program, a package of CDF collaboration especially developped from the B physics group to understand the yelds of heavy mesons coming from SVT. This simulation reproduced all the rings of two track trigger: the eXtremely Fast Tracker XFT, the track eXTRaPolator XTRP both based on drift chamber position measurement, the Level 1 track trigger logic, the Silicon Vertex Trigger SVT based on silicon detector hits information and the Level 2 track trigger logic. I will now discuss in their main features all the chain.

Interaction point

Starting from events coming from one of the previously discussed generators, first step is to smear their primary collision vertex around the nominal CDF interaction point. In particular while in transverse plane (x,y) IP has a well known position ($\sigma_x, \sigma_y \simeq 25\mu m$), along the z direction, i.e. the beam line, due to large spatial dimensions of proton bunches, IP shows up to be distributed mostly gaussian which width is around 30 cm.

This gaussian smearings are applied to the IP of the events. the one along the z direction is particulary important because it affects the fiducial volume of the tracking system on which the trigger (L1 and L2) itself is based. Since it is convenient to use pseudorapidity η for the fiducial volume specification, the η limit is translated to a limiting z position where a track produced at the nominal interaction point,

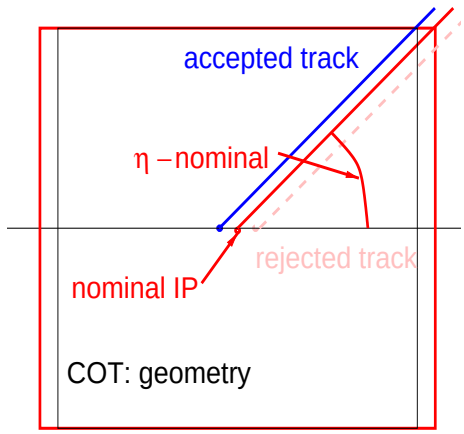

Figure 6.1: The COT fiducial volume, indicated in bold lines, is defined by using the nominal value of η for a track coming from the nominal interaction point IP. For tracks coming from a different z position the track is tested whether it falls within that fiducial volume or not.

with limiting η leaves the COT tracking volume. Each track is then required while traced to be fully contained in the COT; the z coordinate of the track at the outer radius of the COT should be less than the limiting z position. This definition of fiducial volume is then translated in nominal η limit as shown in figure 6.1.

XFT and XTRP simulation

At the lowest trigger level, tracking information is obtained from the XFT which reports two values for each track: the track p_T and the track angle Φ as measured at superlayer 6 of the COT (Φ_6). The momentum threshold of XFT is 1.5 GeV. For Level 1 timing constraints the XFT divides the COT into bins of 1.25^o in Φ_6 and only the highest momentum track in a given bin will be reported. The resolution with which the XFT measures the transverse momentum is better than $\sigma(P_T)/P_T^2 = 0.015 GeV^{-1}$ and it measures the Φ_6 angle with a resolution of 1.5 mrad. Track momenta and angles are smeared according to those resolutions. The XFT is assumed to have a track finding efficiency of 97%, this is implemented as an overall efficiency factor. The XTRP is the unity which reports the XFT track informations to the global Level 1 trigger. At this step COT is divided into 15° bins. the two outermost XFT tarcks with respect to Φ_6, which pass th 2 GeV threshold in p_T, are

reported from each XTRP bin.

Level 1

At Level 1 trigger the selection is operated on the information coming from XTRP board. The logic of Level 1 track trigger is based on a set of kinematic cuts developped originally for two body decays of B mesons like $B \to \pi\pi$. Therefore it is based on track pairs, an event is triggered at Level 1 if it has a pair of XTRP tracks which satisfies the following conditions:

- Each track has $p_T > 2$ GeV.
- The two tracks have opposite charge.
- $p_{T1} + p_{T2} > 5.5$ GeV.
- $\Delta\Phi < 135^o$.

Events with more than 7 XTRP tracks pass automatically Level 1 track trigger in order to avoid time consuming for Level 1 boards which will turn on a high dead time. The transverse momenta cuts rejects large part of the background from inelastic collisions. The additional requirement of opposite charge further reduces random combinations of tracks while maintaining most of heavy flavour physics, moreover HF are produced with significative boost and their deacy products have qualitatively a small angle between them.

SVT

At the second level of trigger, tracking information from the silicon detector SVXII is available through the SVT. The SVT receives a list of hits from the SVX readout and a list of tracks from the XFt as input. Each XFT track, specified by its momentum and Φ_6 angle is used as a starting point to reconstruct SVt tracks by searching for tracks in Φ_0 roads of ± 17 mrad around the given XFT starting value. The Φ_6 angle measured in the XFT is extrapolated to the vertex to match the angle measured by

the SVT. Only tracks that have hits in the innermost silicon layer are accepted by SVT. For this simulation a simplified model of the SVX which takes into account cracks in the z direction is implemented, tracks which pass through crack regions at some fixed radii are rejected. The radii are chosen so that they coincide with the distance of the different silicon layers to the beam line, the crack regions are symmetric in z around the nominal primary interaction point. Tracks reconstructed using SVT have better resolutions than XTRP tracks: $\sigma(P_T)/P_T^2 = 0.013 GeV^{-1}$ and $\sigma(\Phi_0) = 1.5$ mrad. The level 1 selection creteria are then repeated using the new SVT tracks, only once the events pass this selection, Level 2 criteria are applied. The SVT is assumed to have a hit finding efficiency of 98 % per silicon layer and a pattern recognition efficiency of 95% per track. Requiring hits in 4 silicon layers thus results in an overall efficiency $\epsilon = 0.98^4 \cdot 0.95 \simeq 87\%$ per track which is implemented in an overall efficiency considering each track of the event uncorrelated with the others, this effect will be discussed later. The SVT reconstruction of the tracks give the track impact parameter d_0 through the associative memories patterns described in chapter 4. The impact parameter resolution is near to the complete offline reconstruction at online SVT trigger level, wich means an intrinsic SVT d_0 resolution of 35 μm which convoluted with the beam spot in the transverse plane will show up in a impact parameter distribution with a width of around 50 μm. To the impact parameter of the tracks at generator level a corresponding smearing of 35 μm is then applied. This will be shown later on to be the SVT d_0 resolution seen also in the data.

Level 2

Finally the Level 2 selection creteria are applied. These have been divided into two path optimized for two body $B \to hh$ decays and multybody B_s decays, also called respectively "high mass" and "low mass" two track trigger paths.

Level 2 selection cuts are reported in table 6.1, for the two trigger path. Summaryzing all quantities previously described, on which the trigger selection is done, are smeared with appropriate resolution values.

$B \to hh$	multybody B_s (scenario A)
L1 cuts	L1 cuts
$100\mu m < \|d_0\| < 1mm$	$120\mu m < \|d_0\| < 1mm$
$20^o < \Delta\Phi < 135^o$	$2^o < \Delta\Phi < 90^o$
$d_0(B) < 140\mu m$	–

Table 6.1: Cuts applied in the Level 2 track trigger paths.

6.2.3 Optimization of D^0 selection

Here we will focus on particular D^0 decay to $K\pi$ (BR = $3.80 \pm 0.09\%$). This has been chosen because D^0 mesons are the most common decay products of the b quark decay chain $c \to c+X$ coming from direct c quark hadronization into D^0 or through the c quark hadronizing to D^* decaying then to a D^0 meson. Neutral D mesons are also the most probable hadronization of one on the c quarks in a $c\bar{c}$ pair produced at $p\bar{p}$ interaction. Given the secondary vertex request of second level trigger SVT implemented as it has been described in an impact parameter cut on the trigger tracks, the generic QCD event in $p\bar{p}$ interaction is strongly rejected by SVT because particles coming from such an event are more likely to have null impact parameter. Given that, it has been chosen to study the $D^\circ \to K\pi$ signal extraction from two kind of events $b\bar{b}$ and $c\bar{c}$ generated with Pithya and simulated through the detector and the trigger with the generetor level simulation described in previous section. In those processes long lived B and D mesons and their decay product have a non negligible probability to satisfy SVT trigger requests. In $b\bar{b}$ events D mesons come from secondary vertex of b decay so they are likely to have a kink with respect to the B meson direction while in direct D production from $c\bar{c}$ events their reconstructed direction is pointing to the interaction point in which c quark has been produced.

Our analysis rely on two track trigger selection and on offline detector reconstruction of charged particles tracks in solenoidal field using complete CDF tracking system information coming from drift chamber COT and silicon vertex detector SVXII.

In both $b\bar{b}$ and $c\bar{c}$ cases we start from a situation in which most of the back-

ground to the selection of our $D^\circ \to K\pi$ two track signal comes from all possible combinations of track pairs in the event which can be: hadronization tracks coming from interaction point or heavy mesons decay tracks themself.

For the rejection of the background coming from the first family of tracks the request of a high transverse momentum and a significative impact parameter is used while for the second family of background an invariant mass selection on the candidate D^0 decay tracks and angular correlations between them are the essentials simple selection steps.

The statistic of Montecarlo samples on which this study has been done are reported in table 6.2 in which number of events after SVT multibody trigger path requirements also called "scenario A" trigger is shown in first column and number of $D^\circ \to K\pi$ in those events contained in the fiducial volume of CDF tracking system is shown in second column. For the $c\bar{c}$ sample the statistic is very poor due to high generation inefficiency of these events passing through SVT trigger thus resulting in a very long generation time for this events. Nonetheless principal kinematical characteristics of this sample are picked up from this sample. For a more detailed discussion of $c\bar{c}$ production processes see chapter 1.

Table 6.2: Montecarlo Sample.

MC Type	Number of events (after Trigger)	Number of $D^0 \to K\pi$ (after Trigger and in the FV)
$b\bar{b}$ generic	20000	1098
$c\bar{c}$ generic	500	70

The signal reconstruction is performed on events which has passed the trigger "scenario A" requests (see table 6.1). Frist of all $K-\pi$ candidates are picked requiring the combinations to be neutral in charge. Both possible mass assignments are performed and taken as possible candidates. The invariant mass of the pair is then measured applying the request that both tracks are coming from the same secondary vertex. This is implemented by fitting the two tracks helices in the transverse plane thus giving as a result a vertex position in the (x,y) plane.

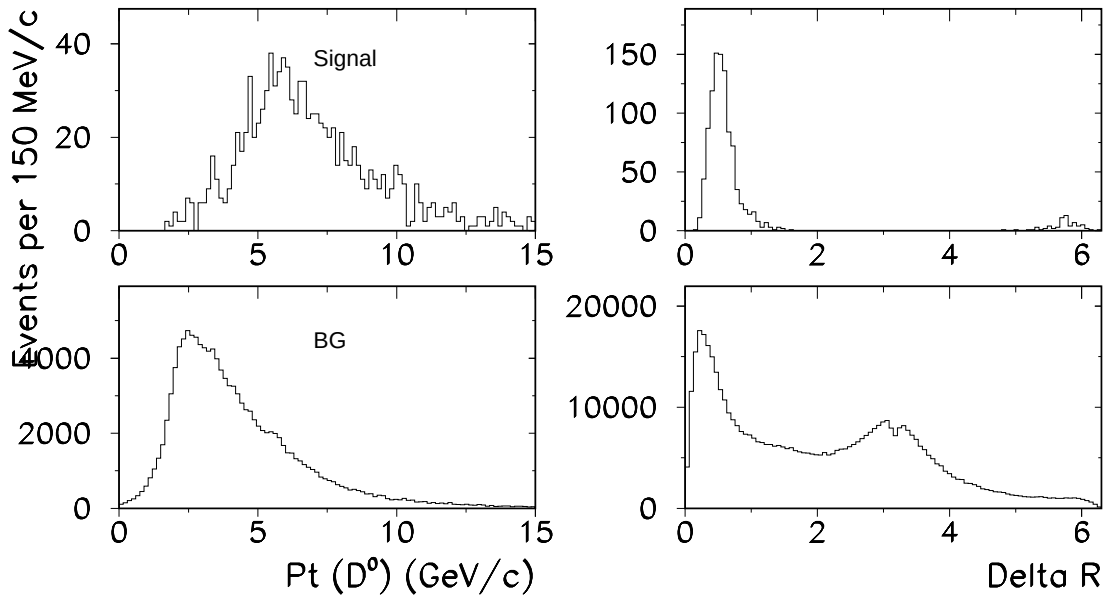

Figure 6.2: Some discriminants between the D° signal (top row) and the $b\bar{b}$ background (bottom row) are $P_t^{D^\circ}$ (left) $\Delta R_{K\pi}$ (right).

No use of vertex χ^2 probability coming from correlation matrix element calculation from the fit is done for the moment for two reasons: this study is based on parametric simulation of detector so resolutions wont by definition take into account all possible correlations coming in real data from detector and also because vertexing probability is strongly dependent from detector allignments and are as a consequence relyiable only in an alligned detector framework which was not the case at the time of SVT commisionig, see section 6.3 ahead in this chapter.

Selection criteria are optimized on the generic $b\bar{b}$ montecarlo, maximizing the S/B ratio on the simulated data. Discriminants are selected studying qualitatively the distributions of several candidate observables for the $D^\circ \to K\pi$ signal as opposed to the simulated background after the scenario-A trigger selection. Figures 6.2 and 6.3 show the behavior of some of the most discriminating observables which have been picked and optimized. In particular we can see that the P_T of the D^0 meson is steef with respect to the combinatorial background of generic $b\bar{b}$ and that the angular

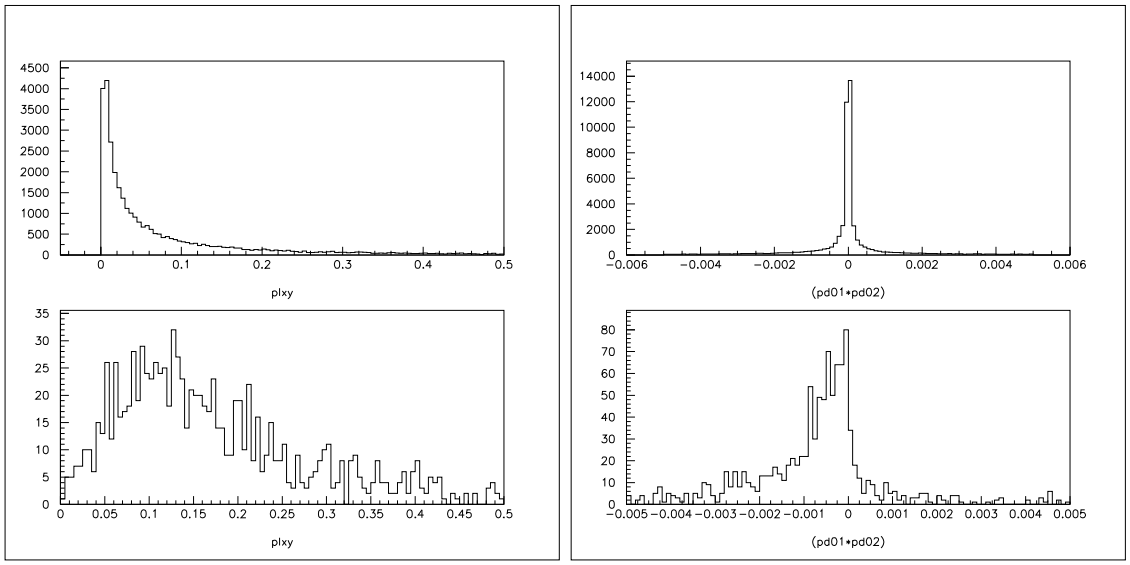

Figure 6.3: D° signal (bottom row) and the $b\bar{b}$ background (top row), projected D^0 flight distance L_{xy} (in cm) on the left and product of D^0 daughters (K and π) impact parameters $d_0(K) \cdot d_0(\pi)$ (in mm^2) on the right.

separation $\Delta R_{K\pi} = \sqrt{\Delta\Phi^2_{K\pi} + \Delta\eta^2_{K\pi}}$ between the kaon and the pion decaying from the D^0 meson is thight with respect to background due to the D^0 boost in the laboratory frame. The projected flight distance of D^0 candidate is then defined as $L_{xy} = \vec{X_V} \cdot \vec{P_T}(D)$ where $\vec{X_V}$ is the decay vertex position vector of the D meson with respect to primary vertex of $p\bar{p}$ interaction and $\vec{P_T}(D)$ is the transverse momentum of the D meson candidate reconstructed from $\vec{P_T}(K)$ and $\vec{P_T}(\pi)$ transverse momenta of its decay products. This quantity is related to the lifetime of D meson candidate and to the impact parameter of the decay tracks. We can see from figure 6.3 (left) that the shape of L_{xy} is peacked to higher value with respect to that of the background, this last is mostly zero-lifetime two track combinations coming from hadronization tracks at the primary vertex. Product $d_0(K) \cdot d_0(\pi)$ between impact parameters of the two daugthers of D meson candidate for $D^{\circ} \rightarrow K\pi$ signal as well as for generic $b\bar{b}$ background.

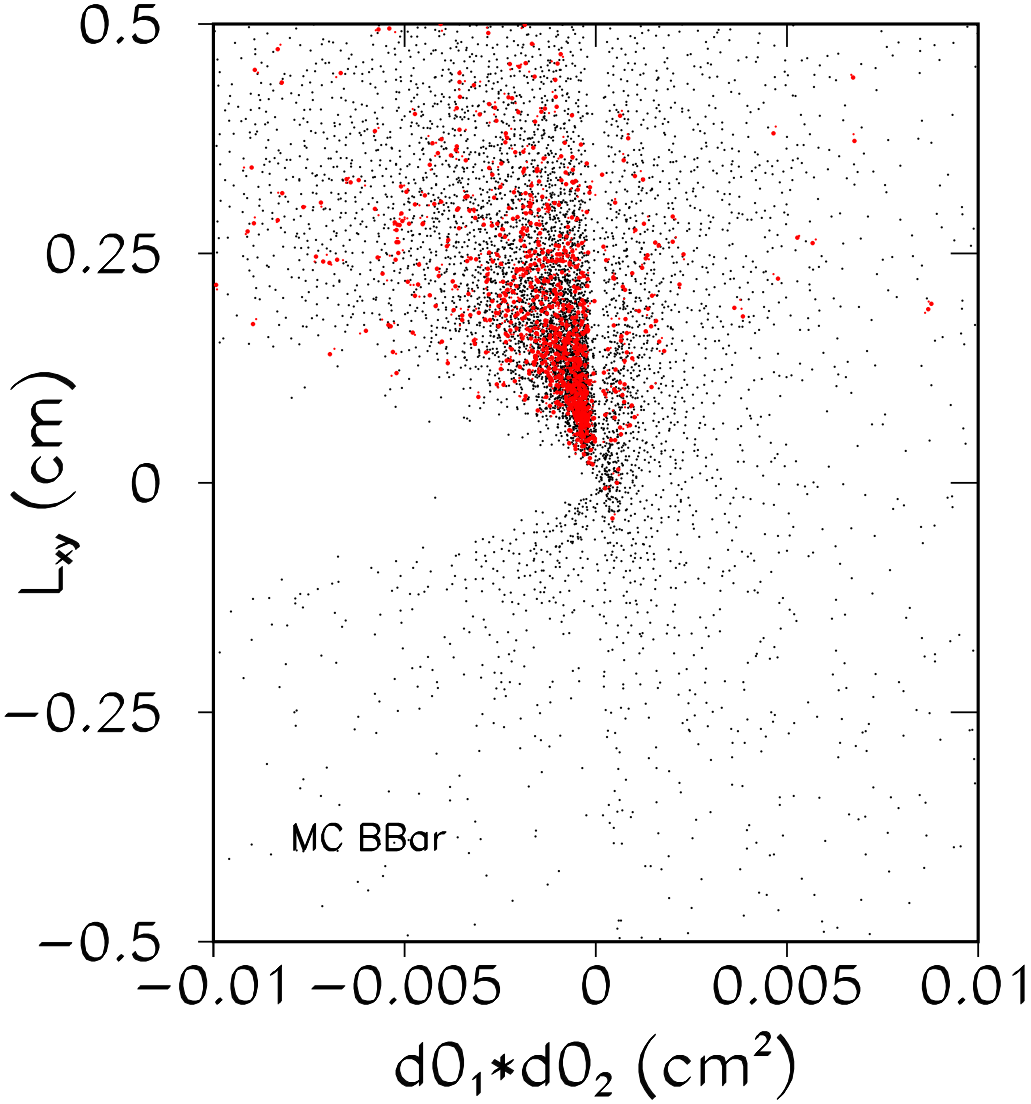

Figure 6.4: This histogram reports the correlation between L_{xy} (y axis) and $d_0^K \cdot d_0^\pi$ (x axis). The black dots are for $b\bar{b}$ background, while red dots are for the $D^\circ \rightarrow K\pi$ signal. The histogram is uniformly populated by random track pairs from the background, while track pairs produced in a particle decay are concentrated in the top left quadrant. Empty regions are byproducts of the trigger bias.

This quantity is relied to the pointing direction of the D meson and will be discussed in detail in section 6.5 it is anyway clear that D mesons coming from B are boosted and have only slight kink from B direction thus the product of I.P. of its daughters is mostly negative in sign; combinatorial background is instead equally positive or negative in sign as a consequence that the distribution of this quantity is only affected from I.P. resolution effects for primary vertex tracks. It is then instructive to look to the correlation between L_{xy} and $d_{01} \cdot d_{02}$ shown in figure 6.4 in which i red we have our $D^\circ \to K\pi$ signal in $b\bar{b}$ events while black points are the combinatorial background. We can see that hadronization tracks from primary vertex are uniform distributed while long-lifetime candidates have a positive L_{xy} and mostly negative $d_{01} \cdot d_{02}$. The complete set of kinematic cuts for $D^\circ \to K\pi$ selection at the end of this study on $b\bar{b}$ events is shown in table 6.3.

Variable	Cut
$\left\|P_t^K\right\|, \left\|P_t^\pi\right\|$	$\geq 1.5\, GeV/c$
$\left\|d_0^K\right\|, \left\|d_0^\pi\right\|$	$100\, \mu m \leq x \leq 1\, mm$
$d_0^K \cdot d_0^\pi$	$\leq 0\, cm^2$
$\Delta\phi_{K\pi}$	$\leq 1.5\, rad$
$\Delta R_{K\pi}$	≤ 2
$\Delta z_0^{K\pi}$	$\leq 5\, cm$
$P_t^{D^\circ}$	$\geq 3\, GeV/c$
$L_{xy}^{D^\circ} = \vec{X}_v \cdot \hat{P}_t$	≥ 0

Table 6.3: Discriminating variables for the $D^\circ \to K\pi$ signal with the requirements as optimized on the $b\bar{b}$ simulation.

This study have as result a baseline set of variables on which operate for the preliminary analysis of charmed mesons on SVT data resumed in the next sessions and the starting point of the measurement presented in this thesis and discussed in chapter 7.

Charmed Reflections

The characterization of the background coming from heavy flavour physics is performed using the montecarlo samples introduced in section previously. Among these backgrounds since no particle identification was available at this early stage of the CDF experiment, we have the effect of mismatching the mass of the K and π in the real $D^\circ \to K\pi$ signal: we will take care of thoroughly understanding this contribution.

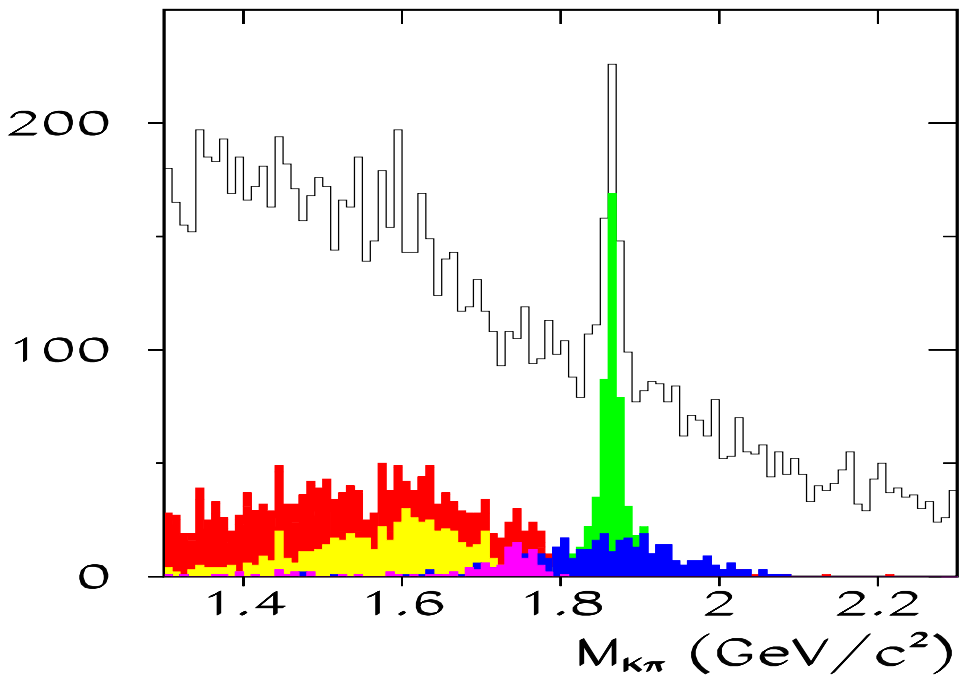

Figure 6.5: Contribution to the $b\bar{b}$ invariant mass spectra from different D° decays: correct $K\pi$ assignement on D^0 decay in green, reversed assignement (here called "reflected peak") in blue, $D^\circ \to KK$ in magenta, partially reconstructed $D^\circ \to K\pi + X$ decays in red, $D^\circ \to \rho^0 K$ decay in yellow. The solid line is the total candidate spectrum composed by the contribution listed here and the combinatorial background.

First of all we look at the invariant mass distribution of all vertices passing the analysis cuts and having both trigger tracks generated from a $D^0 \to h^+h^- + (X)$ (rather than $D^0 \to K\pi$). The contribution of this kind of events to the kinematic region of our signal is negligible with respect to combinatorial backgrund as ap-

parent in Fig. 6.5. The largest background contribution from charm decays come from $D^0 \to \rho^0 K$ as well as $D^0 \to K^+K^-$. In the former, a π^0 from the ρ is not reconstructed and the two remaining charged pions give a broad peak centered at about 1.6 GeV. Once again this distribution has negligible tails under the region of the $D^\circ \to K\pi$ peak. The $D^0 \to K^+K^-$ peaks at 1.76 GeV/c^2 when one of the kaons is assigned the mass of a pion. This peak is however narrow enough to give a negligible contribution in the signal region.

A more important issue is the interference to the signal peak from real signal events in which the K and π masses are mismatched: this distribution peaks exactly at M_{D^0} but has a considerably larger width. Its shape is well described by a gaussian with a width of order 100 MeV: approximately $\times 10$ the width of the peak obtained with the right mass assignments. We take this effect into account by fitting the background plus signal shapes in the MC with:

$$F(M_{K\pi}) = G(M_{K\pi}, \mu, \sigma_S) + G(M_{K\pi}, \mu, \frac{\sigma_R}{\sigma_S} \cdot \sigma_S) + B(M_{K\pi}) \tag{6.1}$$

where $B(M_{K\pi})$ is a first order polynomial to keep into account the combinatorial background and $G(M_{K\pi}, \mu, \sigma_S)$ is a gaussian with mean value μ and r.m.s. σ_S. This fit is shown in figure 6.6.

The first gaussian models the narrow width of the peak for the correct mass assignment while another gaussian with the same normalization and mean ($G(M_{K\pi}, \mu, \frac{\sigma_R}{\sigma_S} \cdot \sigma_S)$) parameterizes the broader peak of the reversed mass assignment. Fitting the MC distribution we get a value for $\frac{\sigma_R}{\sigma_S} = 11.4 \pm 0.5$. Since the width of the reflected peak is significantly larger than the true signal, the contribution of these events to the signal region (f_R) is small. From MC we estimate this fraction to be $f_R \approx 10 - 15\,\%$. The MC samples allow also the measurement of the fraction of background events showing up in the nominal signal region both with the right and wrong mass assignments. ($f_B = 6\%$ in a $\pm 1\sigma$ region). A cross check of the whole procedure is performed selecting candidates in the signal region and inverting the mass assignment: the histogram of the resulting $M_{K\pi}$ is shown in fig. 6.7

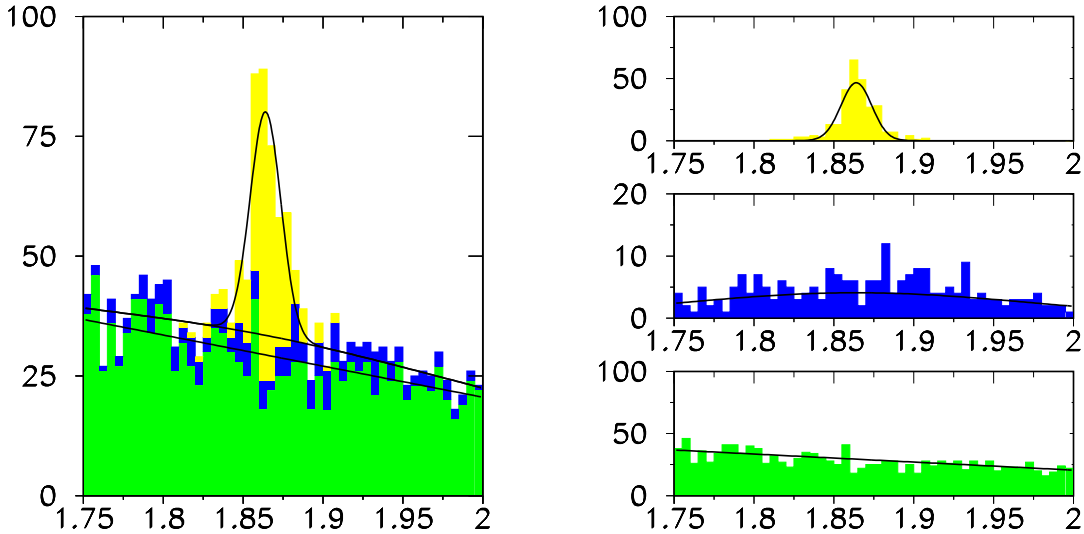

Figure 6.6: Left: $M_{K\pi}$ from $b\bar{b}$ generic MC with the separate contribution from eq. 6.1 superimposed Right: The same distribution for the signal with the correct assignment, the reflected peak and the background

superimposed to the original $M_{K\pi}$ plot.

The shape of the invariant mass distribution obtained with this method is well reproduced by the following function:

$$F_R(M_{K\pi}) = f_R \cdot G(M_{K\pi}, \mu, \sigma_S) + 0.68 \cdot G(M_{K\pi}, \mu, \frac{\sigma_R}{\sigma_S} \cdot \sigma_S) + f_B \cdot B(M_{K\pi}) \quad (6.2)$$

where the parameters of the gaussian and background functions are the ones derived from the original fit. This confirms the interpretation of the underlying broader peak in the invariant mass distribution as a "reflection" of the original signal.

Resulting Performance

The performance of the optimized analysis has been tested both on $b\bar{b}$ and $c\bar{c}$ simulations. Table 6.4 reports the results of this study in terms of the number of events in the initial sample after trigger selection (N_{tot}), signal (S), background (B) and reflected signal (R) for both simulations. The distributions for the signal candidates in both simulations are reported in figure 6.8. The resulting signal efficiency defined as $\epsilon_{Ana} \equiv \frac{S}{N_{tot}^{D^\circ}}$, where $N_{tot}^{D^\circ}$ is the fraction of the N_{tot} events containing a $D^\circ \to K\pi$.

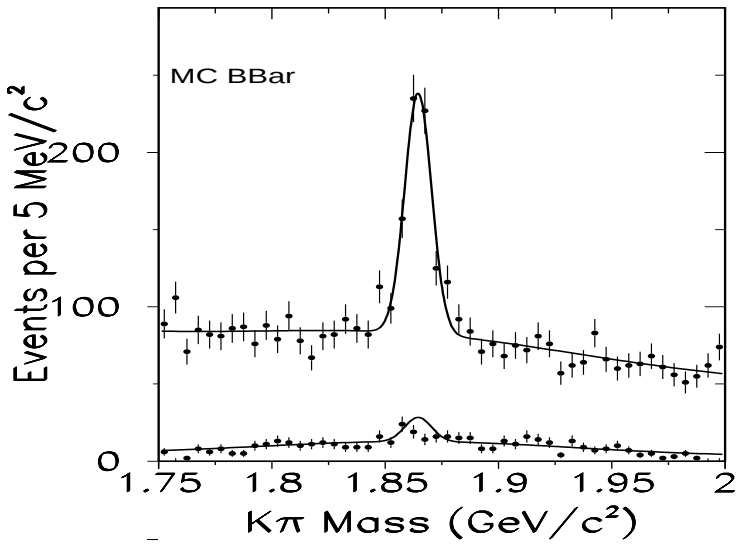

Figure 6.7: $M_{K\pi}$ from $b\bar{b}$ generic MC and the same variable for events falling inside a $\pm 1\sigma$ region around the peak when mass assignment is reversed (see text).

Sample	N_{tot}	$N_{tot}^{D^\circ}$	S	B	R	ϵ_{Ana}	$\frac{S}{B}$
$b\bar{b}$	20000	1098	738	784	154	0.67	0.94
$c\bar{c}$	500	70	37	5	8	0.53	7.4

Table 6.4: Yields for the optimized cuts applied to $b\bar{b}$ and $c\bar{c}$ simulated events. We report the number of events in the initial sample after trigger selection (N_{tot}), signal (S), background (B) and reflected signal (R).

We can see that even in a complicated environment like a $b\bar{b}$ event it is possible through this simple analysis to select $D^\circ \to K\pi$ with a Signal to Background ratio near to 1. This will be a possible lever arm for B meson decays impling a D^0 in the final state and gives the situation in terms of background of any heavy meson hadronic decay analysis. For the $c\bar{c}$ case the S/B is much better given the straightforward fact that there is less long-lived background in those kind of event than in a $b\bar{b}$ one.

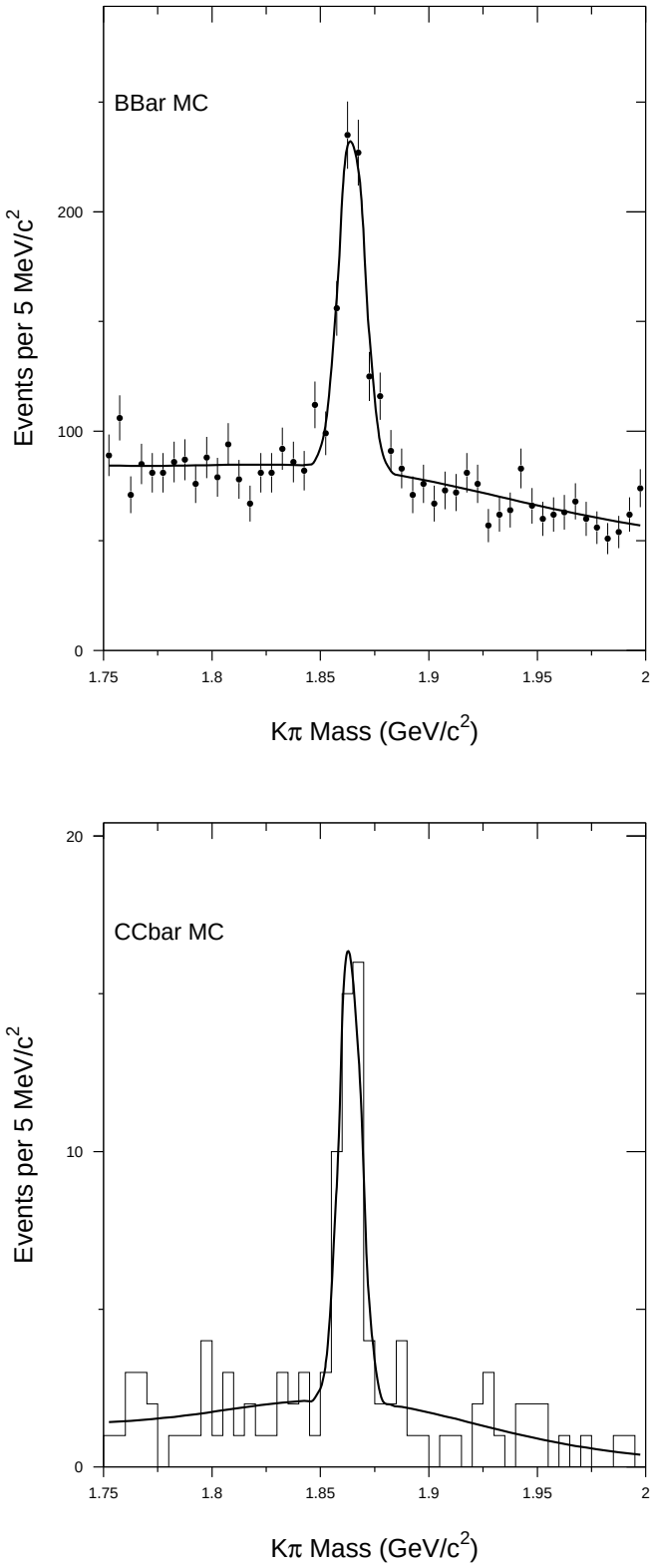

Figure 6.8: $M_{K\pi}$ from $b\bar{b}$ (left) and $c\bar{c}$ (right) generic MC after application of all the trigger and analysis cuts.

6.3 First $D^0 \to K\pi$ signal from SVT

SVT had demonstrated its ability of reconstructing tracks with high precision since the early Commissioning Run of Nov 2000, but what was still needed was evidence that we could use this device as a b (and c) tagger. This further step was achieved using the first runs in which SVT was used as a trigger.

Throughout this exercise a validaton of SVT trigger and of detector offline reconstruction in tracking was achieved in particular for which regards silicon detector misalignment. So, offline tracks with full SVX II reconstruction were used to search for D^0 decaying to $K^{\pm}\pi^{\mp}$ using the results of preliminary montecarlo study described in previous section.

The data used in this analysis was collected by CDF during the Tevatron runs taken in September and October 2001, during the detector commissioning period. We restrict our analysis [34] to the so called "SVT special runs", where the L2 SVT trigger was actively selecting events even if not in the standard trigger table configuration. The L1 two track trigger configurations of these samples are different: the whole set of runs taken was with the `Physics_0_01 [43,207]` trigger table, but with different prescaling factors for the `L1_TWO_TRK2_PS1K` ("two tracks") and the `L1_TWO_TRK2_OPPQ_DPHI135_SUMPT5.5_PS250` ("scenario A") Fred bits. The number of collected events for each run used, together the prescaling factors and the integrated luminosities are listed in table 6.5.

The total integrated luminosity collected by CDF for these runs is 70.12 nb^{-1}, corresponding to an effective integrated luminosity of 17.3 nb^{-1} once the L1 trigger prescale factors are taken into account.

After correction for the beam offset and slope have been performed as reported in section 6.3.1 possible effect of internal misalignment of SVX have been spotted that required an ad-hoc correction as explained in sec. 6.3.2. After this preliminary procedure the D^0 selection was applied to the sample as detailed in section 6.3.3.

Table 6.5: Data sample composition: for each special run we report the total number of events, the total integrated luminosity, the prescale factors and the effective luminosity as obtained rescaling the integrated luminosity by the prescale factors.

Run Number	Events	$\mathcal{L}$ $[nb^{-1}]$	Two-Tracks PS	Scenario-A PS	$\mathcal{L}$ PS $[nb^{-1}]$
127844	81403	11.836	5	250	2.367
128048	85659	8.178	5	250	1.636
128350	383907	33.691	5-7	250	5.058
128442	102700	7.126	1000	2	3.563
128446	29974	2.135	1000	2	1.068
128449	100915	7.154	1000	2	3.577

Run number	X^0_{beam} [cm]	Y^0_{beam} [cm]	S_x [μrad]	S_y [μrad]
127844	-0.0947	0.4080	-135	124
128048	-0.1077	0.3906	625	-381
128350	-0.1038	0.3887	648	-353
128442	-0.1019	0.3927	654	-323
127846	-0.1027	0.3920	626	-363
127849	-0.1024	0.3928	638	-335

Table 6.6: Beam line parameters from BeamFitModule as used in the analysis

6.3.1 Beam line determination

Since the beam line data was not available directly in the DataBase (as it is automatically at present in CDF) for the runs we were interested in we simply used a primary veterxing algorithm using all reconstructed tracks each event of a run to determine the average beam position in the transverse plane and the slope in the longitudinal direction z for each of the run in this analysis. The primary vertex fitter "BeamFitModule" allows to compute the X Y and Z position of primary vertices using either SVX+COT or COT only tracks upon user request. We used 30000 events in each run asking SVX+COT tracks. Fitting the X–Z and Y–Z projection of the primary vertex position the beam position at $Z = 0(X^0_{beam}, Y^0_{beam})$ and the slopes $S_x = \frac{dX_{beam}}{dZ_{beam}}$ and $S_y = \frac{dY_{beam}}{dZ_{beam}}$ were measured. The parameters are reported in table 6.6.

In this early Tevatron's runs the beam appeared to be offset with respect to the tracking detector center by a very large amount of 4 mm in Y and 1 in X. Except for run 127844, when the accelerator attempted to deliver a "straight" beam, all the

runs show significant beam slope both in the X and in the Y projection. Naturally this is a very important effect in the following stage of the analysis, especially in the impact parameter cuts since this quantity is referred to the nominal beam position i.e. the interaction point.

6.3.2 Tracking quality checks

Using beam line parameters from table 6.6 the impact parameter and possibly ϕ of each track were to be corrected to express them relative to the measured beam position center. Given the fact that the beam offset is huge compared to the typical impact parameter of tracks from bottom and charm hadrons and that we wanted to extend this analysis to tracks with low P_T we decided to use the complete formulas for a change of reference point of an helix, retaining also the terms that depend on the curvature:

$$\phi_0' = arctg(\frac{sin(\phi^0) - \frac{\Delta_x}{R-\delta}}{cos(\phi^0) + \frac{\Delta_y}{R-\delta}}) \tag{6.3}$$

where $\Delta_{x(y)}$ are the x and y displacement of the new reference point (the beam line) with respect to the CDF origin, R is the radius of curvature of the helix, δ is the impact parameter and ϕ_0 and ϕ_0' are the azimuthal angle of the track at the point of closest approach to (0,0) and to the new reference point respectively. For the i.p. the following transformation have been used:

$$\delta' = \delta + \Delta_x sin(\phi_0) - \Delta_y cos(\phi_0) + (\Delta_x cos(\phi_0) + \Delta_y sin(\phi_0)) \cdot tan(0.5 \cdot (\phi_0' - \phi_0)). \tag{6.4}$$

Note that the term multiplying the tangent of the difference in the ϕ angles is big so that overall effect is of the order of few microns.

We select tracks with at least 4 axial silicon hits in the innermost 4 layer of SVXII and $P_T > 2$(GeV) to reproduce the SVT requirements. Fig. 6.9 shows that the impact parameter distribution is well described by a two gaussian fit with the core resolution of 60 μm and a second gaussian with a 10% area and a σ of 130 μm. This is definitely worse than the SVT figure of $\approx$ 50 μm so that we searched for some clear effect we could correct for. In fig. 6.9 is shown the i.p. mean value for each ϕ

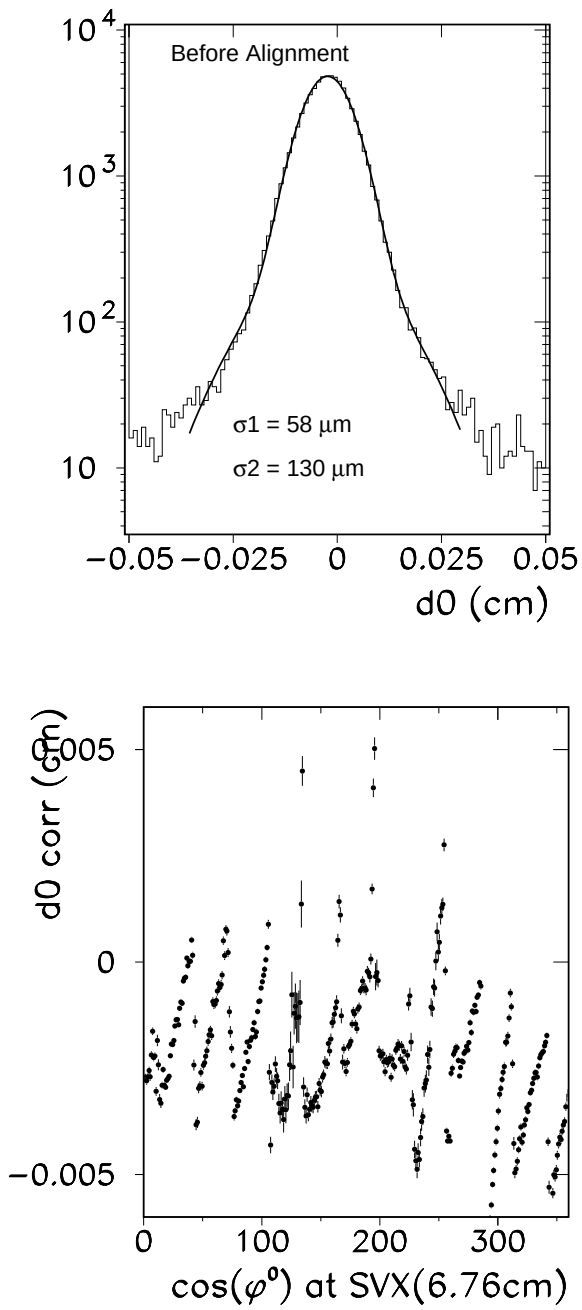

Figure 6.9: Left: raw offline impact parameter distribution for SVX tracks with 4 hit and $P_T > 2$(GeV) Right: $<$ i.p. $>$ vs ϕ.

slice of 1° width. There is some clear structure following the SVX II segmentation in ϕ. Within most of the 12 wedges the dependence of the $<$ i.p. $>$ vs ϕ is linear. This effect turned out to be due to some internal misalignment and/or displacement of the SVX II detector layers. We then simply shift the impact parameter of each track by the deviation of $<$ i.p. $>$ from 0 in each ϕ bin. The resulting i.p. vs ϕ profile histogram is shown in fig. 6.10 as well as the i.p. distribution itself. Now the two gaussian fit gives a core resolution of 51 μm and a tail of 110 μm with a relative normalization at the 10% level. Note that this is not yet as good as one could expect by fitting the same two gaussian function to each ϕ bin where one measure a core sigma of 45 μm, and is an indication of further alignment effect not corrected by the simple procedure here described. In the analysis presented further in this thesis this silicon internal alignments and silicon versus COT global alignments are properly taken into account in the offline reconstruction software through more refined alignment tables.

6.3.3 Data selection and first results

We feed the tracks corrected as explained in the previous section to the "Charm-Mods" module (the official offline software package developped after the montecarlo studies) and apply the cuts described in sec. 6.2. We show in Fig. 6.11 the effect of the various cut on the L_{xy} distribution. The effect of the cut on the impact parameter of the tracks is clearly visible as it enhance the positive tail in the decay length distribution. As expected the $d_0^1 \cdot d_0^2 < 0$ cut mostly affect the peak at 0 decay length.

A clear signal is apparent in the $M_{K\pi}$ distribution when all the cut are applied (Fig.: 6.12). The results of the double gaussian plus linear background fit are reported in table 6.7.

For completeness we report in figure 6.13 both the invariant mass distribution of the candidates selected in the analysis in a wider mass range and the result of the real data study on the reflected peak shown in figure 6.7 for the $b\bar{b}$ montecarlo.

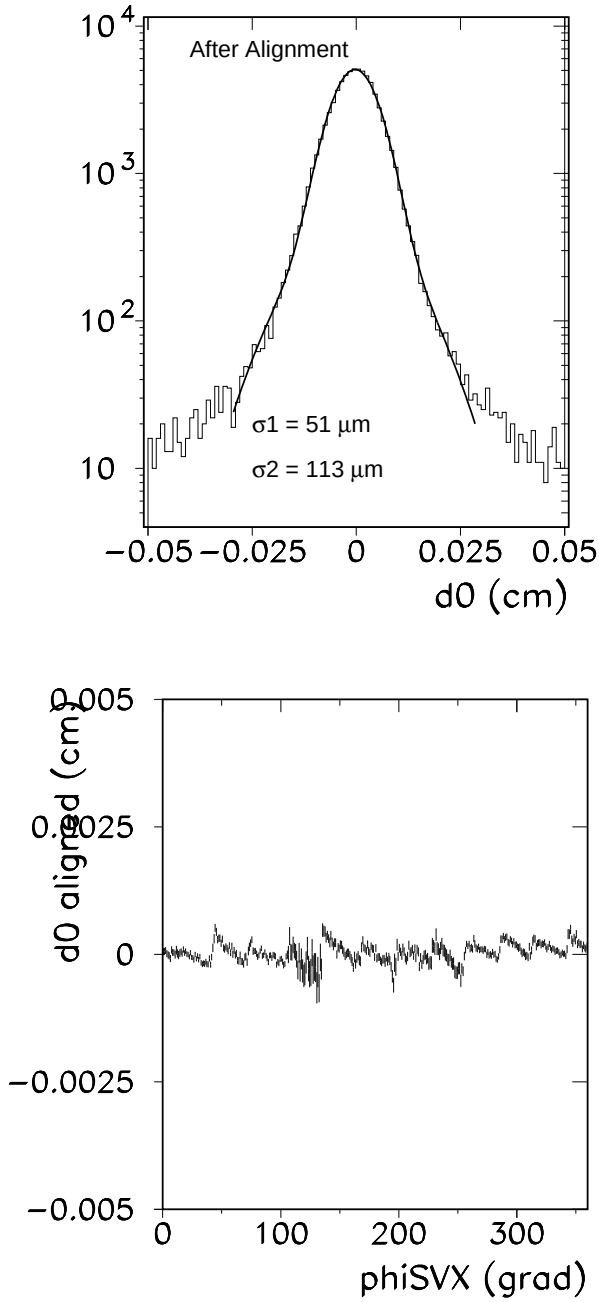

Figure 6.10: Left: impact parameter distribution after "alignment" correction Right: $<$ i.p. $>$ vs ϕ.

Sample	N_{tot}	S	B	R	$\frac{S}{B}$
Real Data	784558	77	112	16	0.7

Table 6.7: Yields for the optimized cuts applied to the real data sample. We report the number of events in the initial sample after trigger selection (N_{tot}), signal (S), background (B) and reflected signal (R).

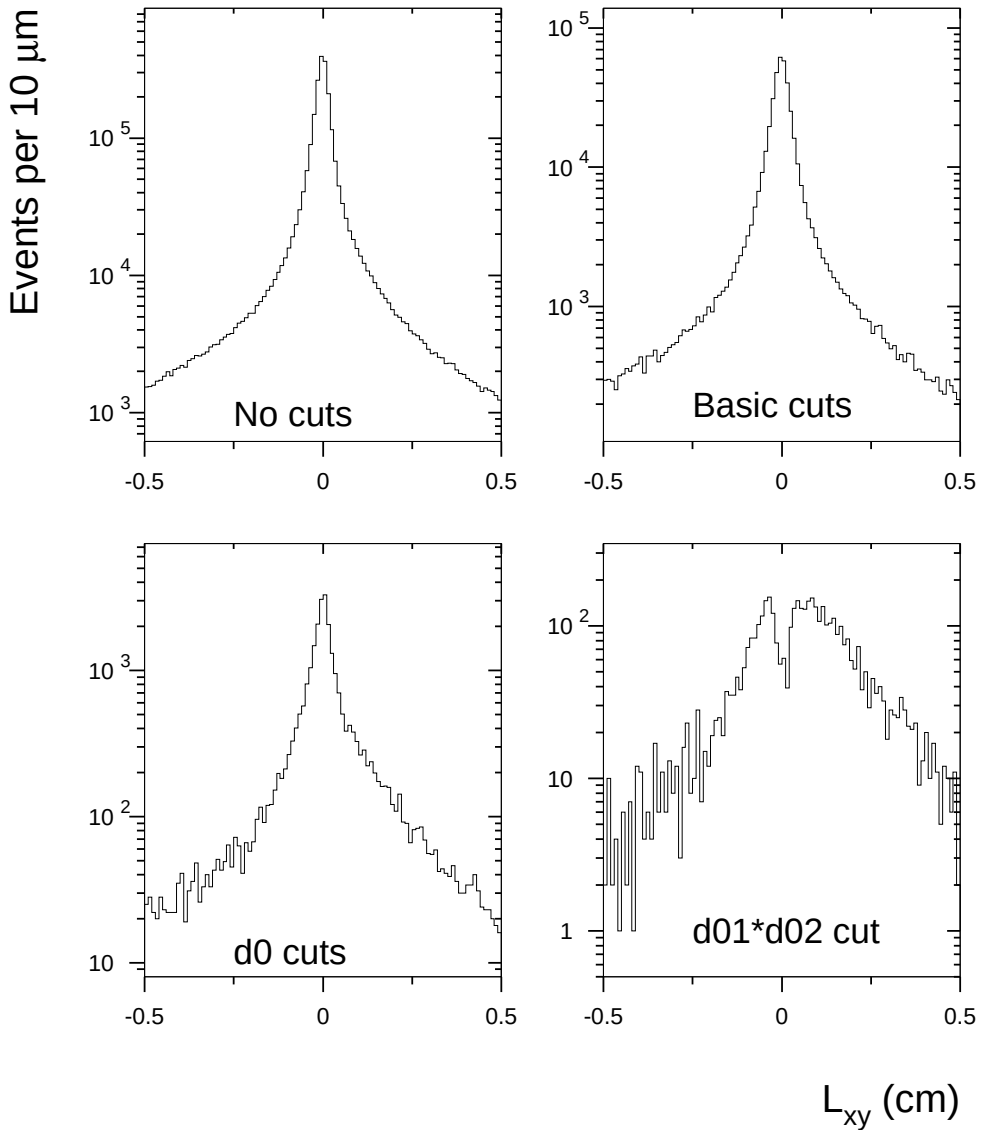

Figure 6.11: L_{xy} distribution at different stage of the analysis. Upper left:all events; Upper right: kinematics cut; Lower left:impact parameter cut;Lower right:$d_0^1 \cdot d_0^2 < 0$

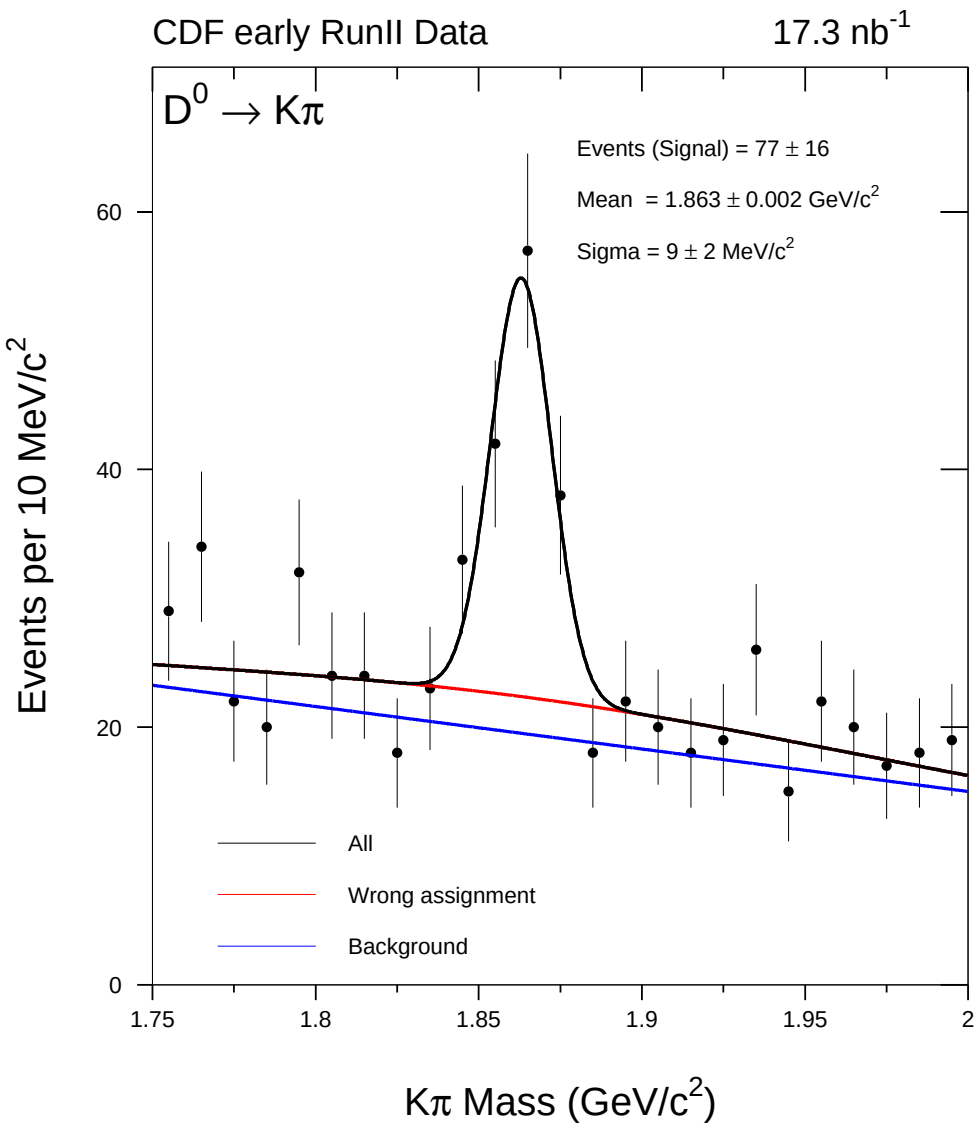

Figure 6.12: Invariant mass distribution for the final selection on real data. The $D^\circ \to K\pi$ resonance contains ≈ 77 events with $S/B \approx 0.7$. The 3 contributions to the fit are reported: in red wrong assignement "reflected peak" broad gaussian, in blue the linear background and in black the sum of those with the tight gaussian signal peak. The results of the double gaussian plus linear background fit are reported in table 6.7

The selection criteria finally applied that have lead to the result plotted in figure 6.12 are the following:

- Offline tracks + n. COT hits > 20 and n. SVX Φ Hits > 2 for K and π
- $|d0| > 100\mu$m and $|d0| < 1$ mm for K and π
- $P_T > 1.5$ GeV/c for K and π
- $P_T(D^0) > 3$ GeV/c
- $\Delta\Phi(K\pi) < 1.5$ rad
- $\Delta R(K\pi) < 2$
- $\Delta z_0(K\pi) < 5$ cm
- $d_0(K) \cdot d_0(\pi) < 0cm^2$
- $L_{xy} > 0$ cm

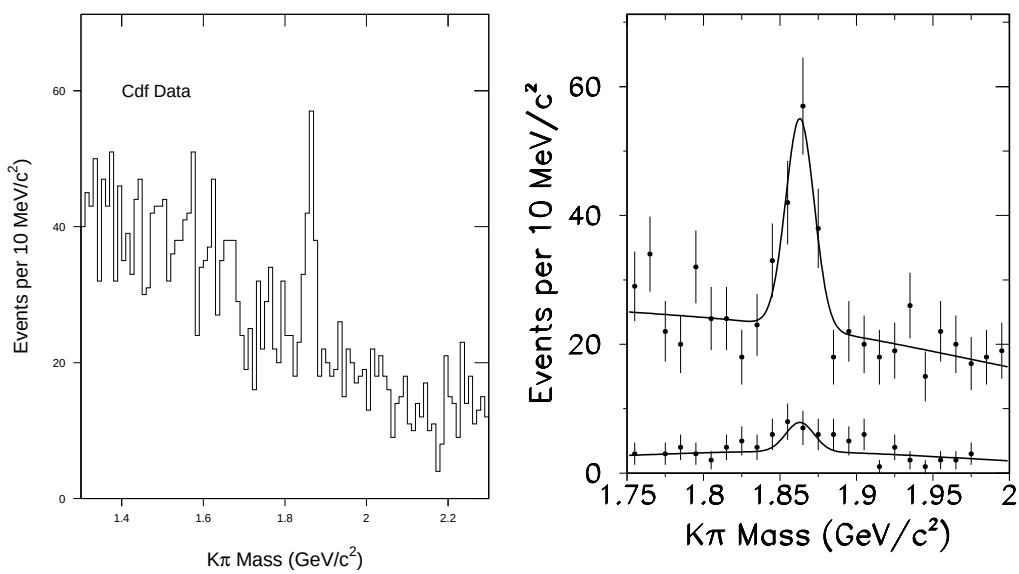

Figure 6.13: Invariant mass distribution of the candidates selected in the analysis in a wider mass range and the result of the real data study on the reflected peak shown in figure 6.7 for the $b\bar{b}$ montecarlo

6.4 Charmed mesons $D^{*\pm}, D^{\pm}, D_s^{\pm}$

After the commissioning period of the detector, started the real data tacking with the SVT trigger in full working conditions. Here are presented some of the analysis of charmed mesons reconstruction in hadronic decays as selected from two track trigger. The methodology is the same of that explained in previous sections with the difference that for charged $D^*, D^{\pm}$ and $D_s^{\pm}$ the more probable decay channels are with three particles in the final state. In those case the request will be that at least one opposite charge track pairs in the final states satisfies the SVT trigger requests.

This means that after basic quality and fiducial volumes cuts for each track:

- number of axial COT hits ≥ 25
- number of stereo COT hits ≥ 25
- number of $r - \Phi$ SVX hits ≥ 3

The specific SVT-like request reproduced at reconstruction level are:

- the two tracks have opposite charge
- each track has $p_T > 2$ GeV
- number of $r - \Phi$ SVX hits ≥ 4 (to match the 4 hits required by SVT)
- $p_{T1} + p_{T2} > 5.5$ GeV/c
- $120\mu m \leq |d_0| \leq 1mm$ for both tracks (multibody trigger path)
- $2^o \leq |\Delta\Phi| \leq 90^o$

Specific analysis cuts will be illustrated for the decays under study as well as results on charmed mesons rates in the two track trigger for a significative fraction of Luminosity integrated by CDF in the first part of year 2002 with the SVT trigger which corresponds to around 5 pb^{-1}.

This section is an introduction to the physics sample on which preliminary estimation of SVT data composition in terms of $b\bar{b}$ vs $c\bar{c}$ has been tempted with the method described in the next section 6.5.

Reconstruction of $D^{*\pm} \to D^0(\bar{D}^0)\pi^{\pm}$ with $D^0(\bar{D}^0) \to K^{-+}\pi^{\pm}$:

Charged D^* reconstruction starts from D^0 decay to $K\pi$ as already done in previous section, adding to it a π of opposite charge to the Kaon from D^0. Given the small Q value of this D^* decay the bachelor pion has low momentum even tacking into account the tipical D^* boost in the laboratory frame $p_T(\pi_b) < 1$ GeV/c approximately. Thus it is not very probable that the π_b track fires the trigger. SVT-like requests are then applied to the two tracks from D^0 and the invariant quantity $\Delta m = M_{K\pi\pi_b} - M_{K\pi}$ is reconstructed. The mass difference Δm between the D^* and the D^0 candidates is peaked at a value corresponding to the sum of π mass and Q value of the decay, in this case ~ 145 MeV. Tipical Δm distribution is shown in figure 6.14.

This property allows a very clean selection of D^0 mesons from D^* decays rejecting most of the combinatorial background. In figure 6.15 D^0 mesons compatible to be the product of a D^* decay is shown after applying the following selection criteria:

- $Q_{\pi_b} \cdot Q_K < 0$
- $|M_{K\pi\pi_b} - M_{K\pi} - 145.42 MeV/c^2| \leq 2 MeV/c^2$
- $d_0(K) \cdot d_0(\pi) < 0$
- $L_{xy}(D^0) > 500 \mu m$
- $p_T(D^*) > 6$ GeV
- No particular request are done on the bachelor pion

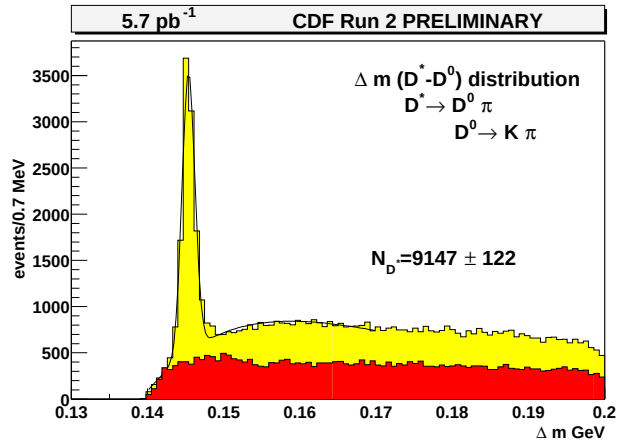

Figure 6.14: $\Delta m = M_{K\pi\pi_b} - M_{K\pi}$ distribution for a total SVT integrated Luminosity of 5.7 pb^{-1}.

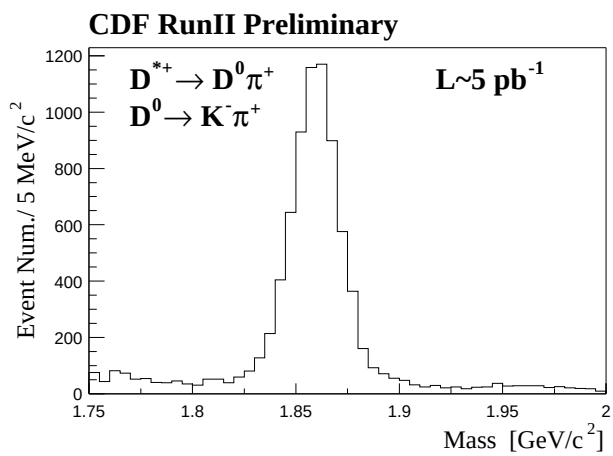

Figure 6.15: D^0 invariant mass distribution after a cut around the tight Δm peak kinematical constraint.

Reconstruction of $D^{\pm} \to K^{-+}\pi^{\pm}\pi^{\pm}$:

For this decay the only difference is the topology which is a three body vertex one. Vertexing fit on the transverse plane is thus applied to the $D^{\pm}$ candidate tracks and a reasonable cut on the fit χ^2 is done. The $D^{\pm}$ inavriant mass is plotted in figure 6.16 after the requirements here listed:

- One SVT-like pair among the 3 tracks.
- $L_{xy}(D^0) > 800\mu m$

- $p_T(D^{\pm}) > 6$ GeV
- $\chi^2 < 40$ for the three track vertex fit

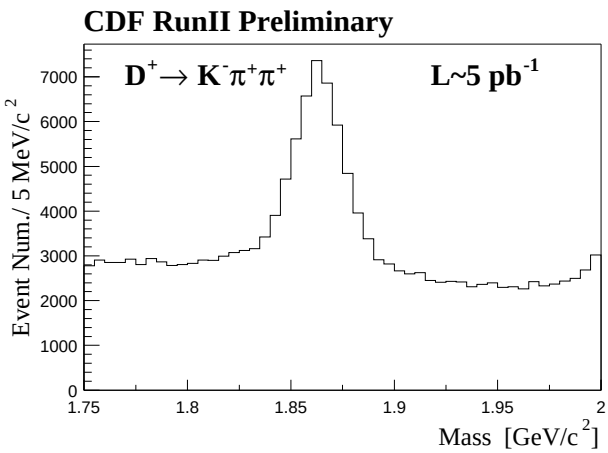

Figure 6.16: The $D^{\pm}$ candidates invariant mass distribution.

Reconstruction of $D_s^{\pm} \to \Phi\pi^{\pm}$ with $\Phi \to K^+K^-$:

In this case the analysis requests are the followings:

- One SVT-like pair among the 3 tracks.
- $L_{xy}(D^0) > 500\mu m$
- $p_T(D_s) > 6$ GeV/c
- $1.01 GeV/c^2 < m_{KK} < 1.03 GeV/c^2$

Result is plotted in figure 6.17. Togheter with the $D_s^{\pm} \to \Phi\pi^{\pm}$ peak there is also a visible signal for the Cabibbo and colour suppressed mode $D^{\pm} \to \Phi\pi^{\pm}$. The comparable relative yield of the two decays is a byproduct of SVT trigger cuts and in particular impact parameter cut, that enhance the $D^{\pm}$ signal due to the longer $D^{\pm}$ lifetime: $\tau(D^{\pm}) \simeq 2 \cdot \tau(D_s)$.

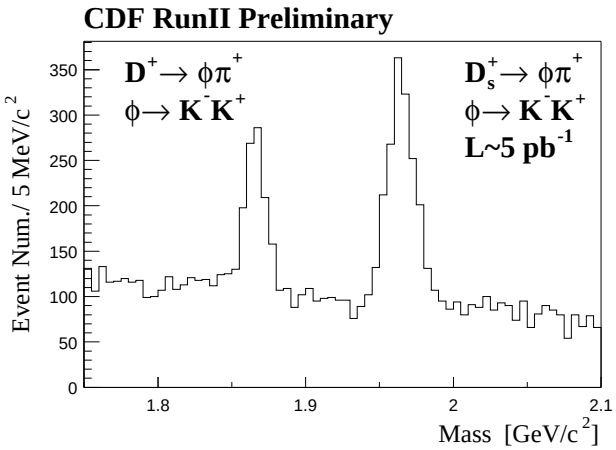

Figure 6.17: $\Phi\pi^{\pm}$ invariant mass after the selection. The D_s and the $D^{\pm}$ decaying to this same state have both clear signals.

6.5 SVT sample $b\bar{b}/c\bar{c}$ composition

Large samples of hadronic D meson decays that have been reconstructed in the data set collected using the Silicon Vertex Tracker trigger of two tracks displaced from the primary vertex as it has been shown in last section 6.4.

These D mesons originate from charm quarks produced directly in the ppbar collision (direct production) and from the decays of hadrons containing b quarks (secondary production). A simplistic method to measure the rate of direct production relative to secondary production using the distance of closest approach (impact parameter) of the D meson with respect to the primary vertex in the plane transverse to the beam axis as been developped.

With perfect tracking resolution, directly produced D's point back to the primary vertex and have a zero impact parameter. Due to the transverse kick in the decay of B hadrons, secondary D's may not follow the line of flight of the B and will not point back to the primary vertex. An illustration of the method is sketched in figure 6.18.

The impact parameter distribution of the reconstructed charm mesons have been fitted with a direct component and a secondary component taking into account the

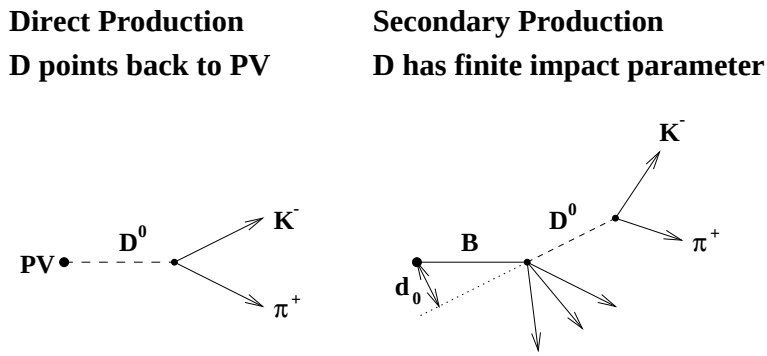

Figure 6.18: Sketch of direct from primary vertex D mesons production and secondary production through B decays different topologies in terms of D meson impact parameter.

resolution on the measured impact parameter.

The detector impact parameter (I.P.) resolution is measured using $K_s \to \pi^+\pi^-$ in the same two-track hadronic data. Since K_s is predominantly produced by direct production at primary vertex it is the best sample to parametrize the I.P. resolution.

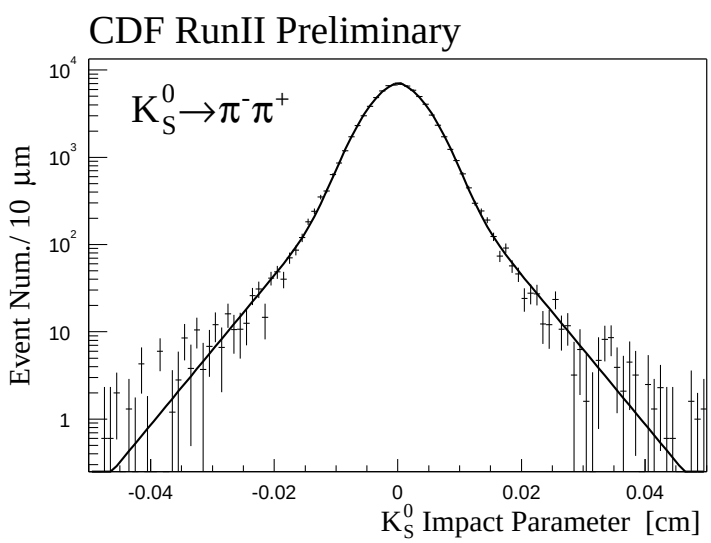

Figure 6.19: Impact parameter distribution of $K_s \to \pi^+\pi^-$.

The parametrization used on I.P.(K_s) distribution is a core gaussian and exponential tails, the distribution and the fit is shown in figure 6.19. The core gaussian which takes into account around 70 % of the K_s sample have a width of about 40 μm, the remaining 30 % is well described as $\sim$ 50 μm lifetime exponential component. Since the long lived D mesons tails are 2 or 3 times longer than the K_s ones,

it is reasonable to use this sample for the I.P. resolution function parametrization.

Nevertheless there is non-negligible contamination from secondary K_s, which results in an extra contribution to the non-Gaussian tail of the detector I.P. resolution. This could be a effect that systematically shifts the measured B fraction towards a lower value.

More refinate studies based on montecarlo are ongoing on this subject. The method exposed here is anyway the strongest lever arm to separate prompt and secondary components in an hadronic inclusive sample and will be used as a baseline towards inclusive charm cross section measurement (see chapter 8 for details).

The preliminary results on the D meson samples, selected as described in section 6.4, in terms of $b\bar{b}/c\bar{c}$ components in the SVT hadronic trigger is reported in the table in figure 6.20.

Mode	f_B	f_B (Gaussian only)
D^0	$16.4 \pm 0.7\%$	$23.1 \pm 0.6\%$
D^{*+}	$11.4 \pm 1.4\%$	$20.0 \pm 1.2\%$
D^+	$11.3 \pm 0.5\%$	$17.3 \pm 0.5\%$
D_s^+	$34.8 \pm 2.8\%$	$37.8 \pm 2.6\%$

Figure 6.20: The measured inclusive B fractions for D mesons from the two-track data. The left hand column corresponds to a resolution function obtained from Ks study. The right hand column corresponds to a resolution function that is a Gaussian only. The fractions in the right hand column are overestimated. The errors are the statistical errors reported by the fit [43]

Results reported in the tables are obtained from the fit to the D mesons impact parameter distributions as it shows up with the selections on tracks described in section 6.4. The fitting function is the sum of the prompt term which has as a template the IP distribution obtained from K_s and the secondary term which is the convolution on the IP resolution function from K_s with the secondary charm impact parameter distribution shape. This shape has been obtained from a montecarlo

study on a sample generated with BGEN (see scetion 6.2) of B mesons inclusive decays to D's $B \to D + X$.

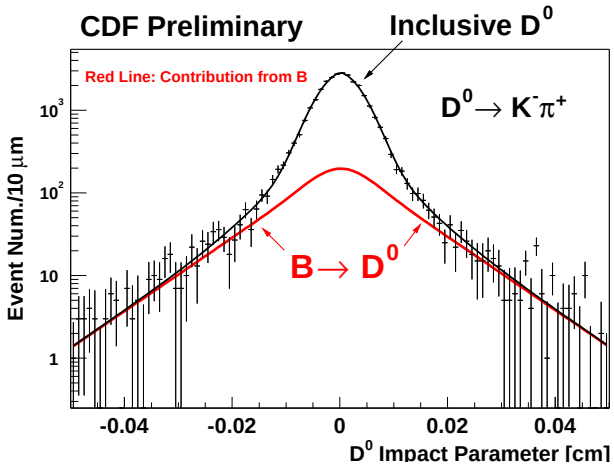

Figure 6.21: The D^0 meson impact parameter distribution is fitted with the detector resolution function obtained from K_s study in black. The red curve is the $B \to D+X$ contribution.

An example of this fit is shown in figure 6.21, for the case of $D^0 \to K\pi$ decay sample. Long lived component is clearly visible in the distribution from which a secondary B fraction in this sample is measured to be around 16 %.

In the table in figure 6.20 the B fractions are also given by parametrizing the impact parameter resolution with a single gaussian model which clearly overstimates those fractions since it doesn't take into account the non gaussian component of IP resolution.

The estimations given here depends on the selection criteria thus the results are not absolute physical numbers. The results are still very interesting on a qualitatively point of view for the understanding of physics the sample delivered from the new CDF SVT trigger, especially in the estimation by data themself of CDF potential in both Charm and Bottom physics.

6.6 Observation of $B^{\pm} \to \bar{D}^0(D^0)\pi^{\pm}$

As a conclusion of this chapter completely dedicated to the reconstruction of hadronic decay modes of heavy mesons from SVT trigger data, we will focus now, on the first attempt to select a fully hadronic exclusive B meson decay.

The data sample is the one that have been collected by CDF from the beginning of the year 2002 till the half of may 2002 which is the sample used by the collaboration for its preliminary results presented this summer.

For the hadronic trigger data on which the work presented in this thesis is based this corresponds to around 10 pb^{-1} of effective integrated Luminosity by SVT, see next chapter, section 7.3 for details on the data sample quality criteria.

The decay $B^{\pm} \to \bar{D}^0(D^0)\pi^{\pm}$ with $D^0 \to K\pi$ has been chosen for his non negligible Branching Ratio ($B.R. = 0.53 \pm 0.05\%$) and most of all because it is the lower multiplicity fully hadronic charged B decay. This choice is related, as underlined in previous chapters, to the SVT trigger momentum cuts efficiency which is suppressed for B mesons decays with high multiplicity of tracks because of the average momentum sharing between them.

Apart from that the optimization study for D^0 meson extraction was in a preliminary phase tought as a first step to $B \to D^0 + X$ analysis and as it has been described in previous sections it has been used here, we summarize now the basic steps of this analysis:

Once the D^0 mesons are selected in and their secondary vertex position reconstructed in the transverse plane, a second vertexing fit is performed constraining the $D^0 \to K\pi$ vertex to point back to the B vertex. To do this the reconstructed D^0 direction is intersected with the track of the pion π_b from the B. All possible π_b in the event are tested exploiting the fact that the charge of the π_b and that of the π from D^0 are opposite. Altough this condition rejects a lot of combinatorial background there will be still a component coming from D^0 autoreflection (see section 6.2) which will be taken into account as a reflection background.

The kinematical cuts between the three particle tracks in the final state have been chosen after a S/B optimization on the generic $b\bar{b}$ sample simulated with parametric simulation of detector and trigger (section 6.2). After the requirement that at least a pair of opposite charge tracks pass the "scenario A" trigger (see 6.4) the complete set of cuts is the following:

- The third track have $p_T > 1$ GeV/c
- $Q_{\pi_b} \cdot Q_{\pi} < 0$
- $\Delta z_0(\pi_b, D^0) < 5$ cm
- $\Delta\Phi(\pi_b, D^0) < 2$ rad
- $200\mu m < L_{xy}(B) < 0.4cm$ and $200\mu m < L_{xy}(D) < 0.4cm$
- $c\tau(B) < 0.2$ cm
- $p_T(B) > 5.5$ GeV/c
- $d_0(B) < 100\mu m$ and $d_0(D) < 0.1cm$
- Distance between B and D vertexices < 0.2 cm
- $d_0(D) \cdot d_0(\pi_B) < 0$
- Vertex fit probability $\mathrm{P}(\chi^2) > 0.5\%$

The results of this selection is plotted in figure 6.22. From the fit to the signal plus backgroud shape parametrized as a gaussian plus second order polinomial, we count $N_B = 56 \pm 12$ in 10 pb^{-1} corresponding to a yield of 5.6 ± 1.2 pb.

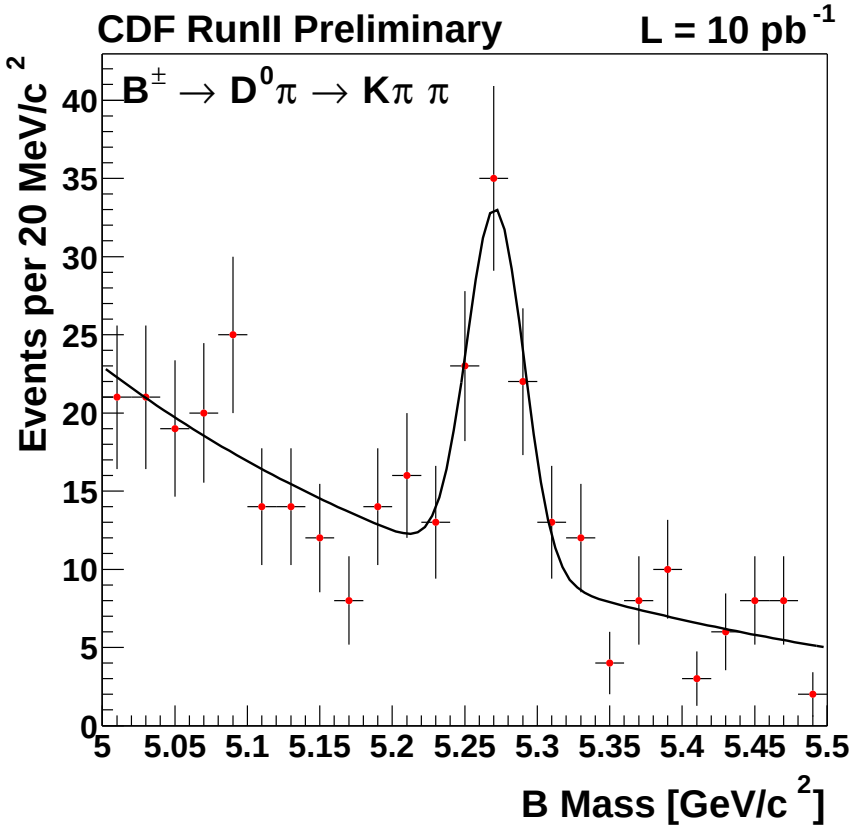

Figure 6.22: The $D^0\pi$ invariant mass after the vertexing and analysis cuts. We extract a number af B decaying to $D^0\pi$ of $N_B = 56 \pm 12$. Mean value of the peak is $M_B = 5.271 GeV/c^2$ and width is $\sigma_M = 19 GeV/c^2$ [**?**].

6.7 Summary

The study on montecarlo samples about charmed meson D^0 selection in the two track trigger has been completed in the period before the real CDF data tacking start. It has succesfully applied on the data since the very early beginning of the run, allowing the first heavy flavour hints in the hadronic trigger.

The $D^0 \to K\pi$ signal extraction analysis in the early runs gave to the collaboration important hints on detector tracking performances in particular for the internal allignments of the silicon, which have been corrected as a consequence.

SVT trigger data commissioning have largely taken advantage of the high statistics physics sample represented by the charmed mesons, just like typical J/Ψ sample for lepton triggers. Charmed meson sample is as a matter of fact now used with J/Ψ's as a physics and offline reconstruction monitor in CDF.

The information extracted from this sample about its relative heavy flavour composition $b\bar{b}/c\bar{c}$ together with first pure hadronic reconstructed B decay like $B \to D^0\pi$ are the first encouraging results to prove that the attempt to select B physics directly on tracks, in a high background environment as an hadronic collider, without relying on lepton trigger, is working.

The large yield of charm in the two track trigger is opening new perspectives for CDF physics measurement opportunities in this sector as will be in part tried to be disigned at the end of this thesis. Simulation and preliminary studies on data, that have been discussed here, are an introduction to one of the first heavy flavour measurements presented by the CDF collaboration in summer 2002. The D^0 BR to Cabibbo suppressed states $KK, \pi\pi$ relative to Cabibbo allowed $K\pi$ discussed in detail in next chapter of this thesis, is actually an excellent hint for both CDF performance on heavy mesons hadronic decays, in terms of precision measurements, and CDF charm physics future perspectives.

Chapter 7

Measurement of the Relative Branching Fractions $\Gamma\left(D^\circ \to K^+K^-\right)/\Gamma\left(D^\circ \to K\pi\right)$ and $\Gamma\left(D^\circ \to \pi^+\pi^-\right)/\Gamma\left(D^\circ \to K\pi\right)$

7.1 Introduction

Given the large charm yield observed in the two track trigger, CDF is in the position to perform statistically competitive measurements of charm production and decays even with little integrated luminosity. The challenge will be then to beat systematic uncertainty to produce interesting measurements. The observation of a $D^\circ(\bar{D}^\circ) \to k^\mp\pi^\pm$ peak has been the first Heavy Flavour signal established in the two track trigger data [34], [35]. Soon after the decays of D° to the CP eigenstates K^+K^- and $\pi^+\pi^-$ were also observed. While these decays are important for measurement of charm meson mixing and possible CP violation effects, in this chapter I will focus on the preliminary measurement of the relative branching ratios of $D^\circ \to K^+K^-$ and $D^\circ \to \pi^+\pi^-$ modes to the more frequent $D^\circ \to K\pi$. Note that throughout this chapter both charge conjugate modes will be implied unless explicitely stated.

In the amplitude ratio many of the systematics associated with trigger and reconstruction efficiency cancel to first order, thus allowing a precise measurment even at such an early stage in Run II data analysis.

We will determine the relative branching ratios as

$$\frac{\Gamma\left(D^\circ \to K^+K^-(\pi^\pm\pi^\mp)\right)}{\Gamma\left(D^\circ \to K\pi\right)} = \frac{N_{KK(\pi\pi)}}{N_{K\pi}} \cdot \frac{\epsilon_{K\pi}}{\epsilon_{KK(\pi\pi)}} = \frac{N_{KK(\pi\pi)}}{N_{K\pi}} \cdot R_{KK(\pi\pi)} \tag{7.1}$$

where $N_{h^\pm h^\mp}$ is the number of D° decaying in the appropriate mode in the data and $\epsilon_{h^\pm h^\mp}$ are the overall acceptance for each of the decay modes. This includes both SVT trigger efficiency and offline reconstruction efficiency.

This chapter is structured as follows: section 7.2.1 describes a study of the most relevant kinematic effects contributing to a non negligeable difference in the relative trigger efficiency of the various modes. This study was performed using a simplified simulation of the trigger and detector; in sections 7.2.2–7.2.5 the more complete simulation of the L1 and L2 trigger is discussed. With this tool the effects of nuclear interactions, decays in flight were taken into account aas well as the more realistic simulation of the SVT processor biases; section 7.3 describes the data sample that has been used; the actual signal extraction is discussed in section 7.4; the result is presented in section 7.4.3; finally follows a discussion on systematics affecting this measurement in section 7.5 and some future perspective in section 7.6.

7.2 Relative collection efficiencies

7.2.1 GenTrig parametric simulation studies

A sample of D mesons generated with BGEN [37] and simulated with the GenTrig [38] package (see chapter 6 section 6.2 for description), in order to illustrate how the different kinematic of the various decay modes affects the relative collection efficiency. Small variations in trigger efficiencies are expected due to the different Q values of the three decays modes arising from the differences in the final state particle masses. This affects the momentum distribution as well as the decay angle of the two particles with respect to the D meson flight direction in the lab frame.

BGEN is used to generate D° mesons that are produced following the same spectra (both P_t and rapidity) as was used in the runI analysis [39] on $D^{*\pm}$ production. These spectra were a result of a theory calculation by M.Cacciari (*et al.)* [40].

This CDF runI measurement on $D^{*\pm}$ was based on semileptonic decays of charmed mesons and looked to an higher momentum spectra for the meson. In particular due to reconstruction momentum threshold for muons in runI, the Pt spectrum of the $D^{*\pm}$ started from 10 GeV. The extrapolation of the calculated spectrum to the present lower bias was done using a smooth function.

Single D° are generated in the transverse momentum and rapidity range $P_t^{D^\circ} > 4$ GeV/c and $|Y_{D^\circ}| < 1.0$. The beam position for this simulation is centered on the nominal CDF origin and the widths of beam are set reasonably to $\sigma_{x,y} = 25$ μm and $\sigma_z = 30$ cm. The events are fed to the GenTrig simulation of the L1 and L2 triggers. This package provides a fast simulation of detector and trigger resolution as well as a fairly detailed description of trigger algorithms. A total of $\approx 3 \cdot 10^6$ events for each decay mode were used for this study.

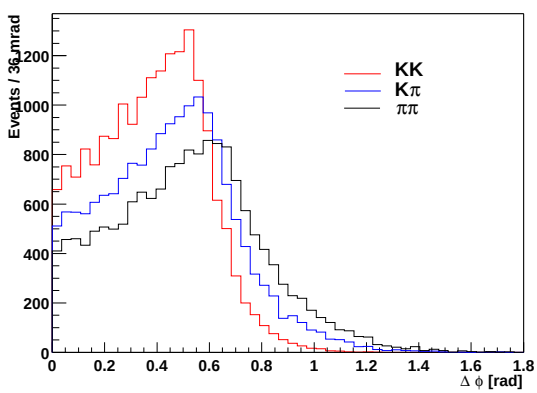

Figure 7.1: Difference in ϕ between the two tracks in the three decay modes before L2 trigger cuts, but requiring two tracks in the XFT acceptance. See text for relative normalization.

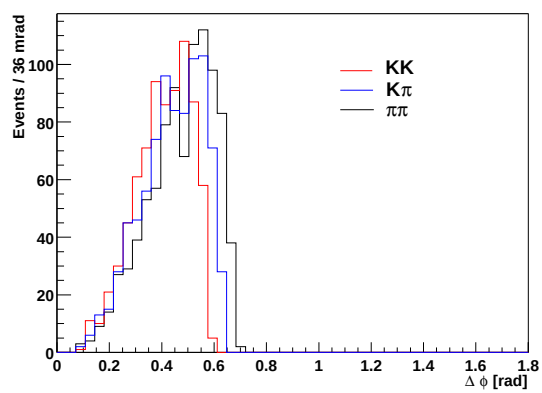

Figure 7.2: Difference in ϕ between the two tracks in the three decay modes after L1 and L2 trigger cuts are applied

The most important effect at the first level trigger arises from the acceptance of the COT and XFT trigger. As it is shown in fig. 7.1 the $D^\circ \to \pi^+\pi^-$ decays tend to have a greater decay angle than the $D^\circ \to K\pi$ and these in turn than the $D^\circ \to K^+K^-$ decays. The opening angle distribution (in the η direction) implies a greater acceptance for KK than $K\pi$ and $\pi\pi$ respectively due to the smaller fraction

of high η tracks missing the outer superlayer (SL6) of COT in the former case. The histograms in both fig. 7.1 and fig. 7.2 have an arbitrary normalization that is the same for all the three decay modes. The greater acceptance at Level 1 for $D^\circ \to K^+K^-$ decays is apparent from the integral of the KK histogram relative to the others in fig. 7.1 in which the differnce in angle ϕ between the two tracks is shown before the L2 biases but requiring that both tracks are in the XFT L1 acceptance.

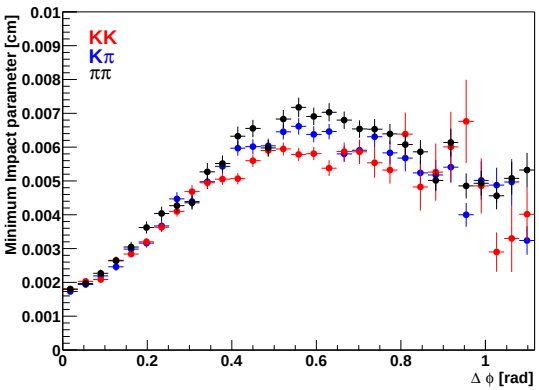

Figure 7.3: Profile of absolute value of the tracks impact parameter $|d_0|$ versus their transvese plane angular separation $\Delta\phi_{hh}$ (for the KK mode).

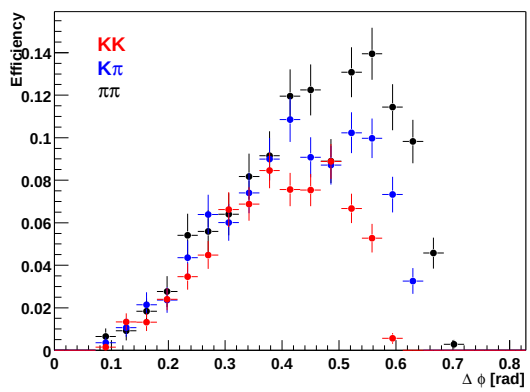

Figure 7.4: L2 trigger efficiency as a function of $\Delta\phi_{hh}$ for the three considered decay modes

At Level 2 impact parameter cuts are applied and we find a reversed situation where $D^\circ \to \pi^+\pi^-$ decays are favoured with respect to the others as the relative sizes of the histograms in fig. 7.2 show. There is, in fact, a trivial dependence ($d_0 \propto tan(\alpha)$) between the daughter track impact parameter (d_0) and its decay angle (α) with respect to the parent long lived particle flight path in the transverse plane. A similar relationship holds between $\Delta\phi_{h^+h^-} = |\phi_0^{h+} - \phi_0^{h-}|$ and $|d_0^{h^+}|$ or $|d_0^{h^-}|$. An additional effect, at high $\Delta\phi_{h^+h^-}$, due to decays with a very asymmetric P_t sharing in the lab frame between the two tracks, causing one track to move very close to the parent meson thus having on average a smaller impact parameter. Fig. 7.3 shows the average $|d_0^{h^\pm}|$, as a function of $\Delta\phi_{h^+h^-}$ for the three different decay modes, suggesting an higher probability for the $D^\circ \to \pi^+\pi^-$ mode to satisfy the trigger

impact parameter requirement. A summary on this effectis given in the graph in fig. 7.4 that shows the L2 trigger efficiency as a function of $\Delta\phi_{h^+h^-}$. As a result the L2 trigger on impact parameter enhances significantly the $D^\circ \to \pi^+\pi^-$ yield and suppress the $D^\circ \to K^+K^-$ with respect to the $D^\circ \to K\pi$ mode. In this way a relative acceptance at the trigger level of $\frac{\epsilon_{K\pi}}{\epsilon_{\pi\pi}} = 0.956 \pm 0.007$ and $\frac{\epsilon_{K\pi}}{\epsilon_{KK}} = 1.078 \pm 0.007$ is determined from the efficiencies reported in table 7.1.

decay mode	$D^\circ \to K^+K^-$	$D^\circ \to K\pi$	$D^\circ \to \pi^+\pi^-$
$P_t^{D^\circ} > 4$ Gev/c, $\lvert Y_{D^\circ}\rvert < 1$	$2716 \cdot 10^3$	$2716 \cdot 10^3$	$2716 \cdot 10^3$
L1 cuts [%]	22.71 ± 0.03	21.11 ± 0.03	19.96 ± 0.02
confirm L1 cuts @ L2 [%]	9.94 ± 0.02	9.19 ± 0.02	8.83 ± 0.02
L2 cuts [%]	1.34 ± 0.007	1.45 ± 0.007	1.51 ± 0.007
offline cuts [%]	68.6 ± 0.2	69.5 ± 0.2	69.5 ± 0.2

Table 7.1: Trigger and reconstruction efficiency for the three decay mode. Offline reconstruction efficiency is calculated with respect to events passing the L1 and L2 trigger cuts. D mesons has been generated with BGEN and trigger and detector simulation used is GenTrig.

The MC events have been reconstructed using the same analysis program that have been used for data (sec. 7.4). The reconstruction efficiency after all cuts have been applied is estimated to be 68.6%,69.5% and 69.5% respectively for the KK,$K\pi$ and $\pi\pi$ modes so that the picture emerging after trigger simulation is in fact confirmed even after final analysis on the fast simulated sample.

In summary, from a sample of signal MC with a fast (parametric) detector and trigger simulation, we derive an overall acceptance correction factor for the relative yields of the $D^\circ \to K^+K^-$ and $D^\circ \to \pi^+\pi^-$ modes with respect to the $D^\circ \to K\pi$ mode of

$$R_{KK} = 1.090 \pm 0.010 \tag{7.2}$$

$$R_{\pi\pi} = 0.956 \pm 0.008 \tag{7.3}$$

7.2.2 A full Geant simulation

The fast simulation described in the previous section does take properly in to account the different acceptance of the detector and of the trigger requirements for the three decay modes considered, but a full GEANT simulation is required to consider other effects that may alter the acceptance ratios as determined from the fast simulation. The most important of these effects are listed in the following:

- Strong interactions of Kaon and pion on the beam pipe and on the material inside the tracking volume have a cross section that depends on the particle species, their charge and their momentum altering the signal yields in a non trivial way.

- $K^\pm$ and $\pi^\pm$ have a different $c\tau$. Assuming that a substantial fraction of decay in flight would not be triggered or reconstructed a difference in the relative yield of the various modes is expected.

- SVT has a P_t dependent tracking efficiency related to the way in which the patterns for the associative memories are derived.

- SVT has P_t and azimuthal angle ϕ biases with respect to the true parameters that depend on the charge of the particles. These biases are a result of the approximation in the SVT track fitting algorithm and of the imperfect alignment of the detector.

- The SVXII detector coverage and hence of the SVT is highly non uniform in ϕ and z due to various detector and trigger problems encountered in the early data taking periods of RUN II.

- The SVXII detector has been moved considerably from its nominal position to partly compensate for a large beam offset and beam slope observed in the early RUN II data. Both the beam offset and the SVXII displacement greatly affect SVT acceptance.

The full simulation program cdfSim, based on GEANT, has been used to model the CDF II detector. The interaction processes with detector material (at the best of its knowledge) were switched on to get the most realistic simulation of the nuclear interaction in the inner volume material, most important contribution to this comes from silicon detector and its support and cooling structures as well as from the inner drift chamber volume separation wall. The SVT processor is emulated using the `svtsim` package, that reproduces the SVT algorithms at the bit level using the same patterns and constants loaded in the real device for normal data taking. The silicon raw data bank (SIXD) is used as input to the simulation. An option was implemented to read a corrected version of the SIXD bank, the latter can be instructed to suppress in a "corrected" version of the SIXD bank all the bad strips and the non functioning detector elements as determined from the online database for any given run. In this way it is in principle possible to simulate on a run by run basis the silicon coverage affecting SVT efficiency, which is then under control from this point of view. For the analysis presented here, emulation of SVT has been performed using real constants and patterns as used in one of the CDF II runs (RUN 142110) included in this analysis. This run was chosen as representative of the setting used in most of the data taking period considered for this work. The number of dead SVT wedge in this simulation is 10, which is very close to the observed mean value of inactive wedges in all the runs (≈ 13).

Differences in the relative acceptance using different SVT configurations will be taken in to account as a systematic and discussed later.

To simulate the effect of the displacement of the SVXII detector relative to the COT (i.e. the nominal CDF frame), the actual alignment tables were used to transform the nominal GEANT geometry in a more realistic one. A particular alignment table have been chosen "`100022 2 TEST`". The same table is also used in the production pass (offline reconstruction) on our MC files in order to properly compensate in the tracking code for the introduced misalignment.

Modeling charge deposition inside the silicon detector elements is a key factor for the simulation of the detector and trigger resolution on the impact parameter measurement. Different charge deposition models are used in CDF, with different level of detail, not all of them being fully developped and validated at the moment. We don't anticipate that using one model or the other will affect in a significantly different way the three decay modes considered, so that a small systematic shift in the acceptance correction factor is expected when switching between different models. For this analysis, then, the simplest geometric charge deposition model is applied, and a systematic will be calculated by comparing this result with the one obtained from the parametric charge deposition model.

7.2.3 Validation of the `svtsim` simulation

The performance of the `svtsim` simulation has been checked with real data. We compared detector and trigger resolutions, known biases in the track impact parameter d_0 measurement of SVT with respect to offline tracking, and the SVT tracking efficiency on a sample of real and simulated J/ψ [41].

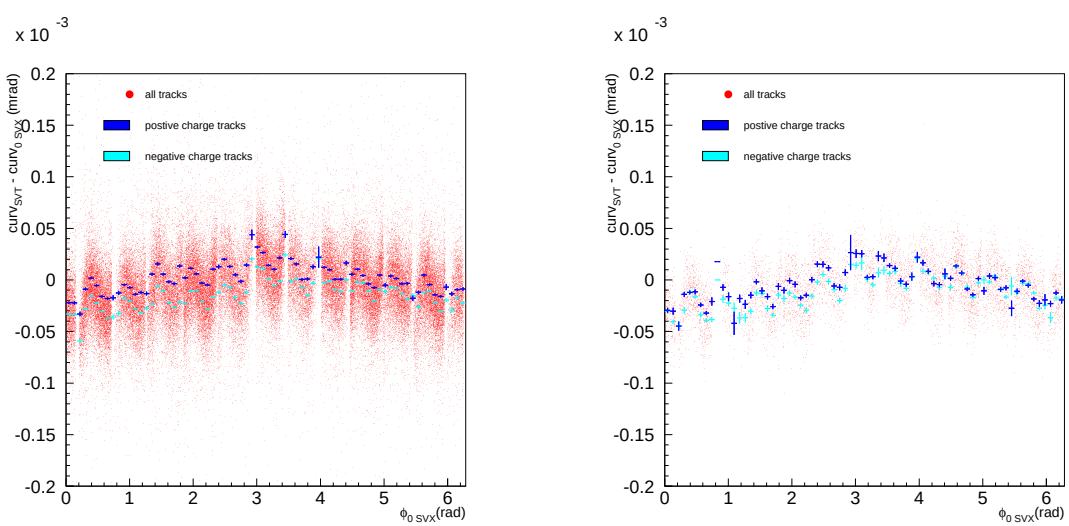

Figure 7.5: Left: Curvature difference between SVT and offline tracks as a function of ϕ for J/ψ data, crosses represents the average difference for tracks with positive (blue) and negative charge (cyan); Right: Same study for simulated J/ψ sample

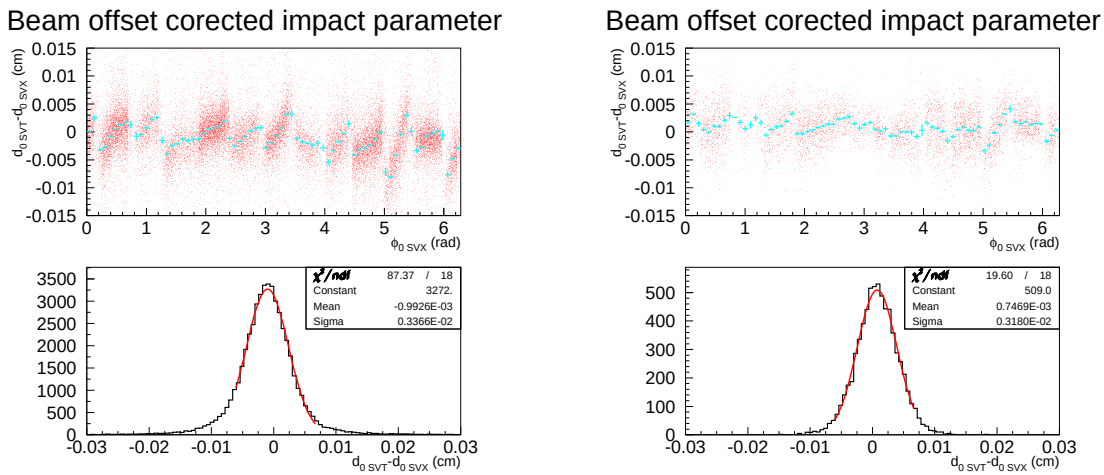

Figure 7.6: Left: Impact parameter difference between SVT level and offline reconstruction level tracks as a function of track angle ϕ for J/ψ data; Right: Same study for simulated J/ψ sample

We analyzed the whole sample of J/ψ from di-muon trigger data. These events were produced with the same version of the reconstruction program we are using on our data (v4.3.1). The run range of this sample matches that of our data so that detector coverage and its effects is guaranteed to be the same. All completely reconstructed tracks associated with muon pairs of opposite charge and whose invariant mass is within 50 MeV/c^2 the J/ψ reconstructed mass are retained for further analysis. Tracks falling within the SVT acceptance are selected looking at the used hits in the silicon detector for the reconstruction. We require 4 R–ϕ hits in 4 different layers within the same ϕ wedge, since the SVT is designed to reconstruct only tracks within a single ϕ wedge of the SVXII detector. Each of these wedges covers approximately a 30° sector. We further match the 4 layers to the exact choice of layers required by the SVT in any given wedge (different wedge by wedge) as determined from the svt configuration retrieved from the database for every considered run. We use for this checks only tracks traversing a single sector in z of the SVXII detector by asking that the z coordinate of the track extrapolated at layer 1 and at layer 5 is

at least 5 mm away from the nominal boundary between electrical halfbarrels, this request restricts the study in a fiducial volume for each SVT sector, avoiding misestimation of SVT efficiency given its working restriction to tracks fully contained in a single sector.

We generated a MC sample composed of a mixture of 20000 prompt J/ψ and 5000 $B^\pm \to J/\psi K^\pm$. The prompt component is obtained by firing with FakeEvent generator single J/ψ in the $P_t > 2$GeV/c and $|\eta| < 1.5$ range with a power law spectrum $\propto P_t^{-2.52}$ derived from a simple fit to the available data. The B component is obtained from BGEN in the same P_t and η range. In both cases no muon trigger simulation is performed at the moment. The beam parameters were chosen to be representative of our data with $x_{beam} = -1.3$ mm,$y_{beam} = 4.0$ mm, $z_{beam} = 3.0$ cm in the CDF reference system and $\sigma_{x,y} = 30\mu$m and $\sigma_z = 30$ cm.

Fig. 7.5 and 7.6 show the ability of the present version of the simulation chain cdfsim/`svtsim` to reproduce the known biases in the track parameters from the SVT device, that are primarily due to detector alignment effects. In particular radial shifts in the nominal wedge positions give the saw-tooth shape of the impact parameter vs ϕ distribution of fig. 7.6, whereas the vertical displacement of SVXII with respect to the COT results in a bow–like shape of the difference between the SVT and SVX curvature as a function of the azimuthal angle as shown in fig. 7.5.

On the track sample selected as above described we are able to measure the SVT tracking efficiency for our data. For each of the track in the sample we look for an associated SVT track with a $\chi^2 \leq 25$ and with a difference in ϕ and curvature with respect to the offline track of respectively 15 mrad and 10^{-4}cm^{-1}. We derive the SVT tracking efficiency as a function of P_t and impact parameter by counting the number of tracks with an SVT match and dividing it by the total number of tracks in each bin. These curves are shown in fig. 7.7. The actual shape of these efficiency functions are determined by the acceptance of the patterns loaded in the SVT associative memory boards. The simulation shows a discrepancy at the few per cent level in the low P_t end of the spectrum. This effect is however much reduced

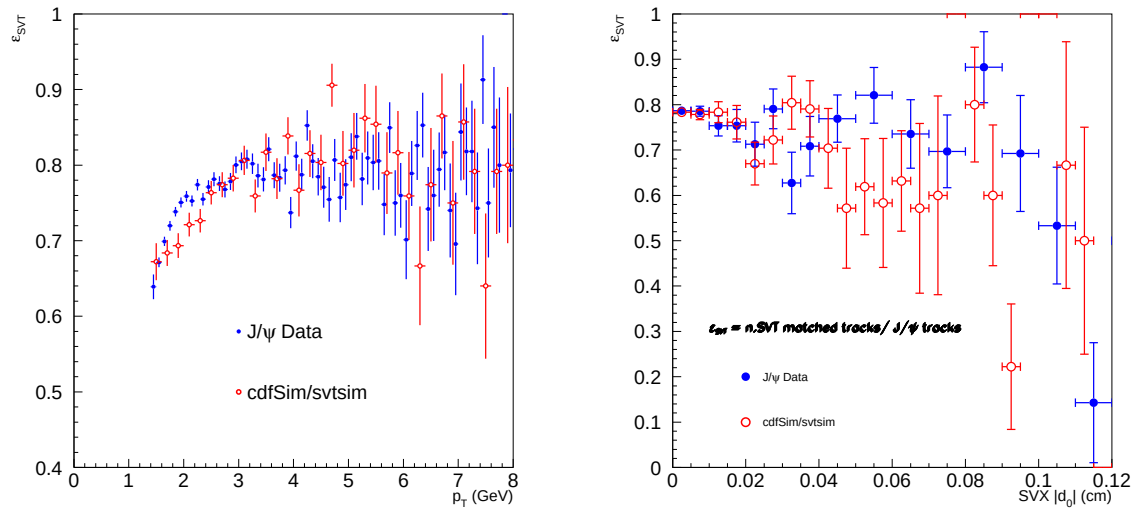

Figure 7.7: Left: SVT tracking efficiency as a function of P_t for J/ψ data (red) and MC (blue); Right: SVT tracking efficiency as a function of track impact parameter d_0.

in the nominal trigger acceptance region of $P_t > 2\text{GeV/c}$ as shown in the efficiency vs impact parameter plot where a further cut $P_t > 2\text{GeV/c}$ has been applied. The average tracking efficiency in the $P_t > 2\text{GeV/c}$ region is $(77.8 \pm 0.2)\%$ for data and $(77.4 \pm 0.5)\%$ in the simulation.

It is important again to note that for the measurement we are describing in this note we are mostly sensitive to the shape of the efficiency vs P_t and impact parameter which seems adequately described by this simulation.

7.2.4 Relative acceptance determination with `svtsim`

For the determination of the ratio of trigger and reconstruction of eq. 7.1 we simulated $\approx 4 \cdot 10^6$ decays for each of the three decay modes. BGEN is used to generate D° mesons following the same spectra (both P_t and rapidity) that was in the RUN I analysis [39] on $D^{*\pm}$ production as was done for the fast simulation. The rapidity spectra were extrapolated to the $|Y_{D^\circ}| < 1.5$ region using a smooth convex curve fitted on each of the P_t bin. Single D° are generated in the transverse momentum range $P_t^{D^\circ} > 4$ Gev/c. The beam parameters were chosen, as in the above men-

tioned J/ψ simulation, to be: $x_{beam} = -1.3$ mm,$y_{beam} = 4.0$ mm,$z_{beam} = 3.0$ cm, $\sigma_{x,y} = 30\mu$m and $\sigma_z = 30$ cm. As a first step we verified using a smaller sample of MC events where the trigger cuts were not applied that the acceptance differences at Level 1 and at Level 2 follow the same pattern as those determined with the parametric simulation (see sec. 7.2.1). Table 7.2 shows that indeed the $D^\circ \to K^+K^-$ mode has the greatest acceptance at Level 1. The L1 cuts confirmation at Level 2 introduces an inefficiency due mostly to the reduced acceptance of SVT relative to the XFT and to the effect or resolution smearing on track parameters between XFT and SVT. Since in this simulation we introduced a further reduction of $\approx 15\%$ in the actual SVT acceptance per track due to inactive wedges we do expect an even greater efficiency loss at L2 with respect to the parametric simulation where we did not take into account this effect. This is in fact confirmed as can be seen comparing tables 7.1 and 7.2.

decay mode	$D^\circ \to K^+K^-$	$D^\circ \to K\pi$	$D^\circ \to \pi^+\pi^-$
input (N_{events})	60000	60000	60000
L1 cuts (%)	7.9 ± 0.1	7.6 ± 0.1	7.2 ± 0.1
confirm L1 cuts @ L2 (%)	1.18 ± 0.04	1.02 ± 0.04	0.89 ± 0.04

Table 7.2: Trigger efficiency at L1 and L2 with `svtsim`

To extract from MC the relative acceptance of trigger and analysis cuts we implemented a module to select only events passing L2 multibody hadronic trigger cutting on the SVTD quantities. The trigger cuts are:

- $P_t^1 \geq 2$ GeV/c, $P_t^2 \geq 2$ GeV/c
- ${\chi^2}^1 \leq 25$, ${\chi^2}^2 \leq 25$
- $120 \leq |d_0^1| \leq 1000\mu$m, $120 \leq |d_0^2| \leq 1000\mu$m
- $2^\circ \leq |\phi_0^1 - \phi_0^2| \leq 90^\circ$
- $P_t^1 + P_t^2 \geq 5.5$ GeV/c
- $L_{xy} \geq 200\mu$m

In order to cut on impact parameter in the simulation an ad-hoc beam offset subtraction has to be performed mimicking the online beam fitter. The latter perform beam position fits every few seconds during data taking and subtract the beam offset in real time on the tracks found by SVT. In our MC data we fitted the d_0 vs ϕ correlation plot for each SVXII electrical barrel using the actual list of track from `svtsim`, and subtracted from all the tracks in our signal sample the resulting beam offset.

Decay mode	$D^\circ \to K^+K^-$	$D^\circ \to K\pi$	$D^\circ \to \pi^+\pi^-$	R_{kk}	$R_{\pi\pi}$
generated N_{events}	3833860	3884670	3616109		
L2 cuts	6438	7300	7454		
$\epsilon_{h^+h^-}$ [%]	0.168 ± 0.002	0.188 ± 0.002	0.206 ± 0.002	1.12 ± 0.03	0.91 ± 0.02
offline cuts [%]	73.7 ± 0.4	73.0 ± 0.4	71.2 ± 0.4	1.11 ± 0.03	0.94 ± 0.02

Table 7.3: Trigger and reconstruction efficiencies with `svtsim`

We predict trigger efficiency in the 0.2 % range for our sample of D° with $P_t > 4$ GeV/c and $|Y_{D^\circ}| \leq 1.5$ as reported in table 7.3. The ratio of trigger efficiency is determined to be $\frac{\epsilon_{k\pi}}{\epsilon_{kk}} = 1.12 \pm 0.03$ and $\frac{\epsilon_{k\pi}}{\epsilon_{\pi\pi}} = 0.91 \pm 0.02$. The MC events have been reconstructed using the same analysis program that have been used for data (sec. 7.4). The reconstruction efficiency after all cuts is estimated to be $73.7 \pm 0.4\%$, $73.0 \pm 0.4\%$, $71.2 \pm 0.4\%$, respectively for the $D^\circ \to K^+K^-$,$D^\circ \to K\pi$ and $D^\circ \to \pi^+\pi^-$ modes. Taking into account both trigger and reconstruction efficiency we calculate the acceptance correction factor as:

$$R_{KK} = 1.11 \pm 0.03 \tag{7.4}$$

$$R_{\pi\pi} = 0.94 \pm 0.02 \tag{7.5}$$

where the errors come just from the available MC statistic.

7.2.5 Effect of decay in flight and hadronic interaction

To understand how the difference in lifetime between kaons and pions as well as the different nuclear interaction cross section between kaons and pions and from kaons of different charge affect the relative yield of the three decay modes, we followed two approaches.

1. switching off decays in flight and nuclear interaction effects in GEANT and performing the complete `svtsim` simulation.

2. using single $K^\pm$ and $\pi^\pm$ from FakeEvent generator and getting the size of the correction with which we should correct the parametric simulation result.

Following the first approach we simulated $\approx 3 \cdot 10^6 D^\circ$ decays for each mode switching off the DCAY and HADR option in GEANT. Moreover to compare to what have been done with the parametric simulation we set the mean z position of the beam to 0 and restricted the generation to the $|Y_{D^\circ}| < 1$ range. Table 7.4 reports the measured efficiency and ratio of acceptance from this simulation. As expected we find an increased efficiency due to lack of the decay in flight and hadronic interaction. The ratio of acceptance, though, varies less significantly.

decay mode	$D^\circ \to K^+K^-$	$D^\circ \to K\pi$	$D^\circ \to \pi^+\pi^-$	R_{kk}	$R_{\pi\pi}$
generated	2817627	2820000	2900000		
L2 cuts	5331	5612	6117		
$\epsilon_{h^+h^-}$ [%]	0.189 ± 0.003	0.199 ± 0.003	0.211 ± 0.003	1.05 ± 0.03	0.94 ± 0.03
offline cuts [%]	75.0 ± 1.0	76.0 ± 1.0	73.0 ± 1.0	1.07 ± 0.03	0.98 ± 0.03

Table 7.4: Trigger efficiency with `svtsim` and GEANT decay in flight and hadronic interaction switched off. $|Y_{D^\circ}| < 1$ and $z_{beam} = 0.0$ cm

As an alternative we estimated the effect of decays and interactions by generating 10000 each of K^+,K^-,π^+,π^-, with FakeEvent with a P_t^{-3} spectrum between 2.0 and 20 GeV/c and $|\eta| < 1$. The P_t spectrum approximately reflects that of D° daughters in our data. By looking at the MC information we determined the probability for a particle of a given species to undergo a decay or a strong interaction. Since no trigger simulation and no reconstruction is performed on these samples in this case, we assign as an uncertainty on this determination the difference of the result obtained by considering that the event would be lost if any secondary vertex is found or if none of the secondary tracks has $P_t > 2$ and impact parameter smaller than 1 mm.

The interaction and decay probability (P_h) averaged over our P_t spectra are reported in table 7.5. These probabilities agree well with simple estimates at fixed

	$K^+(\%)$	$K^-(\%)$	$\pi^+(\%)$	$\pi^-(\%)$
DCAY(1)	6.0 ± 0.2	6.0 ± 0.2	0.66 ± 0.08	0.96 ± 0.10
DCAY(2)	3.7 ± 0.02	3.7 ± 0.2	0.28 ± 0.05	0.39 ± 0.06
HADR(1)	2.8 ± 0.1	4.5 ± 0.2	4.9 ± 0.2	4.6 ± 0.2
HADR(2)	2.5 ± 0.2	4.1 ± 0.2	4.4 ± 0.2	4.1 ± 0.2
DCAY+HADR(1)	8.5 ± 0.3	9.7 ± 0.3	5.5 ± 0.2	5.5 ± 0.2
DCAY+HADR(2)	5.9 ± 0.2	7.0 ± 0.3	4.6 ± 0.2	4.5 ± 0.2

Table 7.5: Probability P_h of hadronic interactions (HADR) and decay in flight (DCAY) in GEANT on single Kaons and pions. Rows marked with (1) refer to the probability to produce any secondary vertex. Rows with (2) give probability to have a vertex from which no particle satisfying trigger requirements emerge. Errors are statistical only.

momentum from the published $K^{\pm}/\pi^{\pm}$ cross section on deuterium [44]. From those numbers we derive an hadronic interaction and decay in flight correction factor ($F^{corr}_{hh'}$) for the parametric trigger simulation of sec. 7.2.1 as:

$$\epsilon^{corr}_{hh'} = \epsilon_{hh'} \cdot (1 - P_h) \cdot (1 - P_{h'}) = \epsilon_{hh'} \cdot F^{corr}_{hh'} \tag{7.6}$$

where $\epsilon_{hh'}$ are the uncorrected efficiencies for the three decay modes from table 7.1 and we averaged over the two charge combinations in the case of $D^\circ \to K\pi$ decay. The resulting efficiency ratios corrected with the above F factors are reported

description	R_{kk}	$R_{\pi\pi}$
svtsim	1.11 ± 0.03	0.94 ± 0.02
quicksim+corr.	1.11 ± 0.02	0.94 ± 0.02
svtsim -decay -hadr	1.07 ± 0.03	0.98 ± 0.03
quicksim	1.09 ± 0.01	0.956 ± 0.008

Table 7.6: Comparison of the overall acceptance corrections for the $D^\circ \to K^+K^-$ and $D^\circ \to \pi^+\pi^-$ mode using different detector and trigger simulations; svtsim is the complete simulation to be compared with quicksim+corr where hadr. interaction and decay in flight correction where applied to quicksim; "svtsim -decay -hadr" refers to the complete simulation where the decays in flight and hadronic interactions are switched off to be compared to the raw quicksim result.

in table 7.6 along with results from previous paragraphs. Within the statistical accuracy of the present study the two approaches give consistent results. We use conservatively the residual difference as an estimate of the accuracy of our detector and trigger simulation.

7.3 The data sample

The analysis is based on the data collected by CDF with the SVT two track trigger since February 2002 up to early May 2002. The data are recorded in a dedicated stream named B_CHARM that has been produced with version 4.3.1 of the CDF offline reconstruction program, this was the state of the art version on wich the CDF relied on its summer 2002 results. This data correspond to a total of $\approx$ 19pb^{-1} of integrated luminosity (online luminosity measurement). A substantial fraction of this luminosity corresponds to periods in which the SVX II detector was not operational for different reasons. The list of bad runs was excluded from this analysis. This runs were marked bad for either known detector problems (e.g. COT High Voltage) or trigger problems. The latter include the first few nb^{-1} were the two track trigger was prescaled, and runs where the online beam position fitter for SVT was not reporting a valid fit.

The total integrated luminosities of the sample are listed in table 7.7.

	Luminosity (pb^{-1})
Total	19.0
No SVX	7.5
Bad Runs	1.9
Used	9.6

Table 7.7: Data sample: Total luminosity and actual luminosity used in the analysis (summer 2002).

7.4 Signal reconstruction

Signal reconstruction is performed relying on the official version of the D° finder in the CharmMods package developped as a result of the montecarlo study discussed in section 6.2.

Two tracks candidates are picked requiring the combinations to be neutral in charge. Since particle identification is not yet available, for $D^\circ \to K\pi$ both possible mass assignments are performed. The resulting autoreflection background has been

Variable	Cut
$\lvert\Delta\phi_{(SVT-COT)}\rvert$	$< 0.015\ rad$
$\lvert\Delta curv_{(SVT-COT)}\rvert$	$< 0.00015\ cm^{-1}$
χ^2_{SVT}	< 25

Table 7.8: SVT-offline tracks matching criteria.

Variable	Cut
N axial COT	≥ 25
N stereo COT	≥ 25
N R_ϕ SVX	≥ 3
Algorithm	OIZ
$\lvert\eta\rvert$	≤ 2

Table 7.9: Tracks selection.

studied in detail in section 7.4.1. The track selection match offline tracks to SVT tracks, in order to select only candidate vertices that were firing the two track multi-body trigger. Two track candidates are required to satisfy the *scenario A* (see section 7.2.4) trigger requirements, applied both on the offline reconstructed quantities and on the SVT quantities with the same matching criteria used in L3 and listed in table 7.8.

The detailed list of tracks quality requirements is reported in table 7.9. The invariant mass of the pair is then measured applying CTVMFT, with the only constraint that the two tracks originate from the same vertex. No pointing constraint to the primary vertex is applied.

Final discriminants are selected studying qualitatively the distributions of several candidate observables for the $D^\circ \to K\pi, D^\circ \to K^+K^-$ and $D^\circ \to \pi^+\pi^-$ Montecarlo signals and on generic Montecarlo $c\bar{c}$ and $b\bar{b}$ background, after the trigger selection. Same selection criteria are used for the three signals ($K\pi$, KK and $D^\circ \to \pi^+\pi^-$), with cuts optimized maximizing the $S^2/S+B$ ratio. The detailed list of used cuts is reported in table 7.10.

The reconstructed two track invariant mass for the three signals selections are shown in figure 7.8 and 7.9. In the distribution corresponding to the two kaon

Variable	Cut
$\left\|P_t^i\right\|, \left\|P_t^j\right\|$	$\geq 2.0\,GeV/c$
$\left\|d_0^i\right\|, \left\|d_0^j\right\|$	$120\,\mu m \leq x \leq 1\,mm$
$d_0^i \cdot d_0^j$	$\leq 0\,cm^2$
$\Delta z_0^{i,j}$	$< 5\,cm$
$P_t^i + P_t^j$	$> 5.5\,GeV/c$
$P_t^{D^\circ}$	$> 5.5\,GeV/c$
$L_{xy}^{D^\circ} = \vec{X}_v \cdot \hat{P}_t$	$> 500\mu m$

Table 7.10: D° candidate selection $(i(j) = K, \pi)$

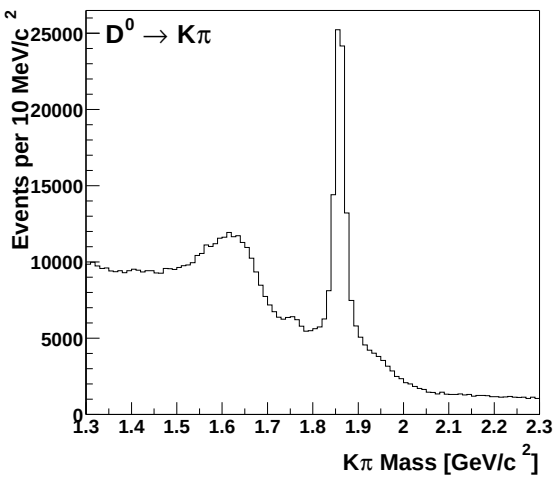

Figure 7.8: $M_{k\pi}$ distribution after final selection $D^\circ \to K\pi$.

and two pion mass hypothesis several peak are visible due to reflections of the $D^\circ \to K\pi$,$D^\circ \to K^+K^-$,$D^\circ \to \pi^+\pi^-$.

The large bump on the low mass side in the $D^\circ \to K\pi$ and $D^\circ \to K^+K^-$ plots is instead originated by partially reconstructed D° where one or more particles are lost, the dominant contribution being the $D^\circ \to K\pi\pi^\circ$ decay with the π° not reconstructed. We note instead that the $K\pi$ reflections do not contribute significantly in the KK and $\pi\pi$ signal regions.

The superimposed fits in 7.9 shows that is possible to describe the reflection peaks using combination of Breit–Wigner and Gaussian shapes. The fit function for the $D^\circ \to K^+K^-$ case includes a Breit–Wigner for the low mass bump, a Gaussian for the signal and a function that is Gaussian below its peak value and a Breit-Wigner

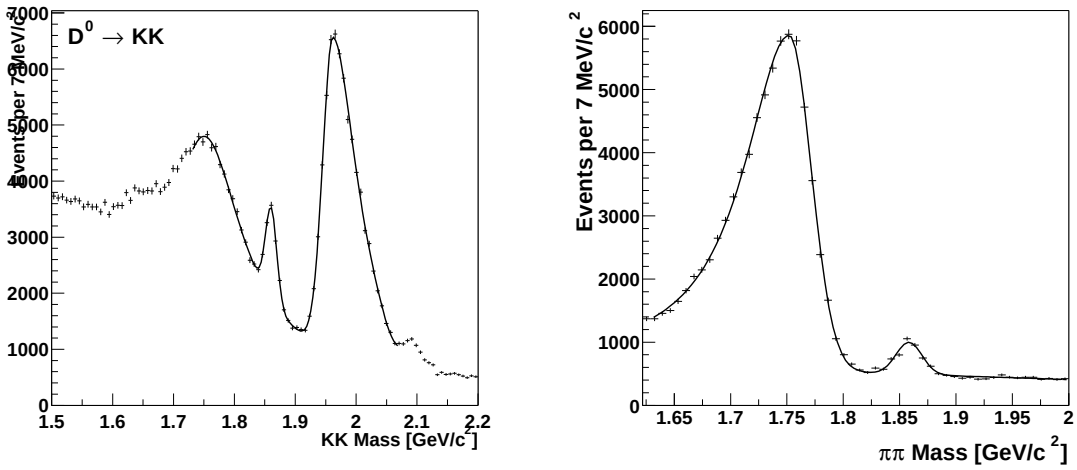

Figure 7.9: Left: $M_{k^+k^-}$ distribution after final selection $D^\circ \to K^+K^-$. (See text for fitting function description). Right: $M_{\pi^+\pi^-}$ distribution after final selection $D^\circ \to \pi^+\pi^-$

for masses greater than the peak value to describe the $D^\circ \to K\pi$ decays peak where the kaon mass is assigned to a pion. The remaining background is parametrized with a first order polynomial. In the same way for the $D^\circ \to \pi^+\pi^-$ decay the large $D^\circ \to K\pi$ peak is fitted with a Gaussian and a Breit–Wigner and a polynomial is added for background as well. Fitting in the same invariant mass plot the KK and $K\pi$ signals (or $\pi\pi$ and $K\pi$ signals) my prove in the future as an alternative way to measure the yield ratio, that is independent of the autoreflection peak systematics described in 7.4.1. However this method require further studies of the model for the fitting functions for the different peaks, so for the time being we choose to extract signals from the individual reconstructed peak with the "correct" mass hypothesis, as described in the following sections.

7.4.1 Effect of K–π swap in the $D^\circ \to K\pi$ peak

Charged particle identification in CDF is based on the specific ionization energy loss, measured in the central drift chamber, and on the Time of Flight as measured by the new TOF detector. Both methods require further optimization and are not completely ready to use at the time of this analysis. Moreover, since the L2 trigger requires two tracks with a transverse momentum of more than 2 GeV/c, the TOF

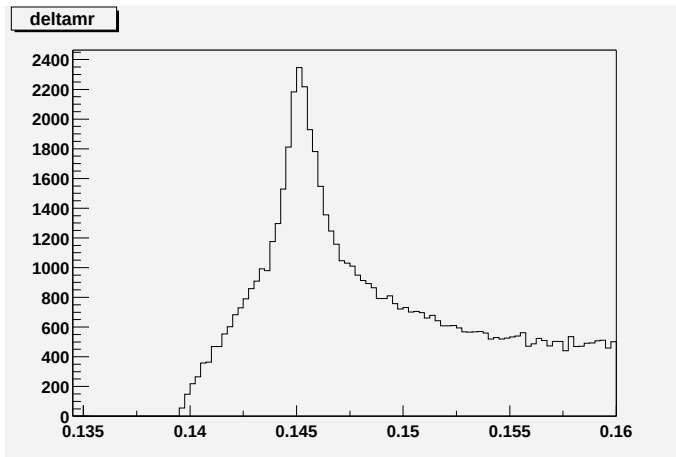

Figure 7.10: ΔM distribution of $D^{*\pm}$ sample selected with a $\pm$ 2 σ cut around the D° mass. The two superimposed histograms are obtained requiring or not requiring an explicit cut of more than two $R-\phi$ hits in SVX-II for the bachelor pion.

will be anyhow of limited use for the K–π separation for D° triggered by the SVT, then a model for this autoreflection background is needed in order to statistically subtract this contribution from the observed signal events.

The effect of the K–π swap on the $D^\circ \to K\pi$ peak has been already studied on Montecarlo [34], 6.2. It can be shown that the the wrong mass assignment peak is centered on the same mass as the correct one and that has an approximately Gaussian shape, with a width that is almost an order of magnitude larger, giving an autoreflection background in a 3 σ window of the $D^\circ \to K\pi$ peak of about 35%. This behavior has been confirmed on data studying the effect of the K–π swap on the D° peak from $D^{*\pm} \to \pi^\pm D^\circ$ decays where the anti-correlation of the charge of the bachelor (or "slow") pion with that of the Kaon from D° gives a powerful discrimination between true signal and the autoreflected D°. The shapes of correct and wrong assigned mass peaks, ignoring the effect of doubly Cabibbo suppressed decays (DCS), an $O(0.1\%)$ effect, can be determined directly on the data, as well as their behavior as a function of kinematic variables of the parent D°. To select $D^{*\pm} \to \pi^\pm D^\circ$ decays, we add to the D° candidates selected as described in previous section a soft pion track with $p_T > 400MeV$ and 3 or more R–Φ hits in SVX, in order to reconstruct the $D^{*\pm}$ invariant mass. The $\Delta M = M(k\pi\pi_S) - M(k\pi)$ mass difference

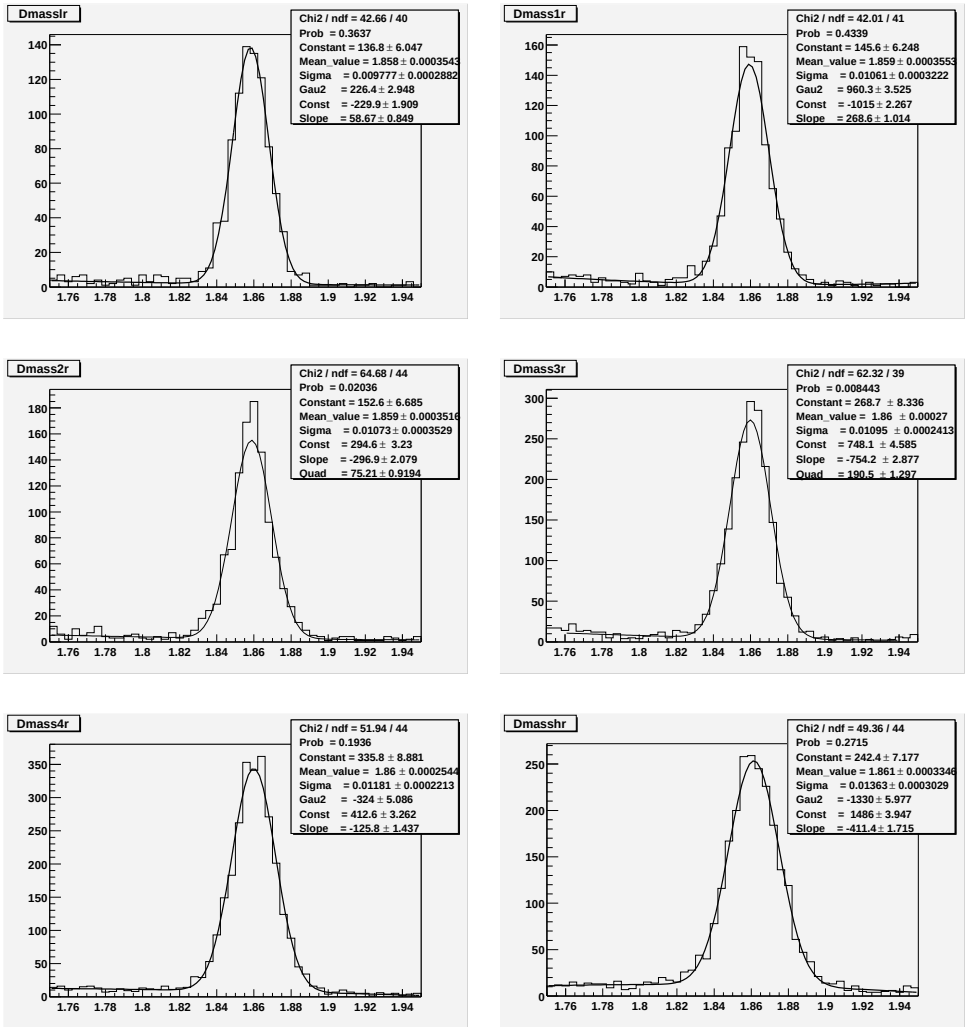

Figure 7.11: $M_{k\pi}$ invariant mass distribution for the 6 P_t ranges, for correct charge correlation with the bachelor pion from $D^{*\pm}$.

(shown in figure 7.10) is then selected to be between $0.143.4 \div 0.147.3$ MeV/c^2, corresponding to an interval of $\pm$ 2 σ around the ΔM peak of 145.3 MeV/c^2.

In order to unfold the D° momentum dependence we fitted the right and wrong assignement peaks in 6 P_t bins, from 5.5 to 20. GeV/c. Both the right and wrong sign peaks are fitted using a single Gaussian plus a polynomial function for the background. In Fig. 7.11 and 7.12 the fitted $M_{k\pi}$ mass distribution for the right and wrong sign are shown.

The χ^2 probabilities of the fits range from 0.2% to 90%. Mean values in the right and wrong distributions are consistent with each other in all the P_t bins, and

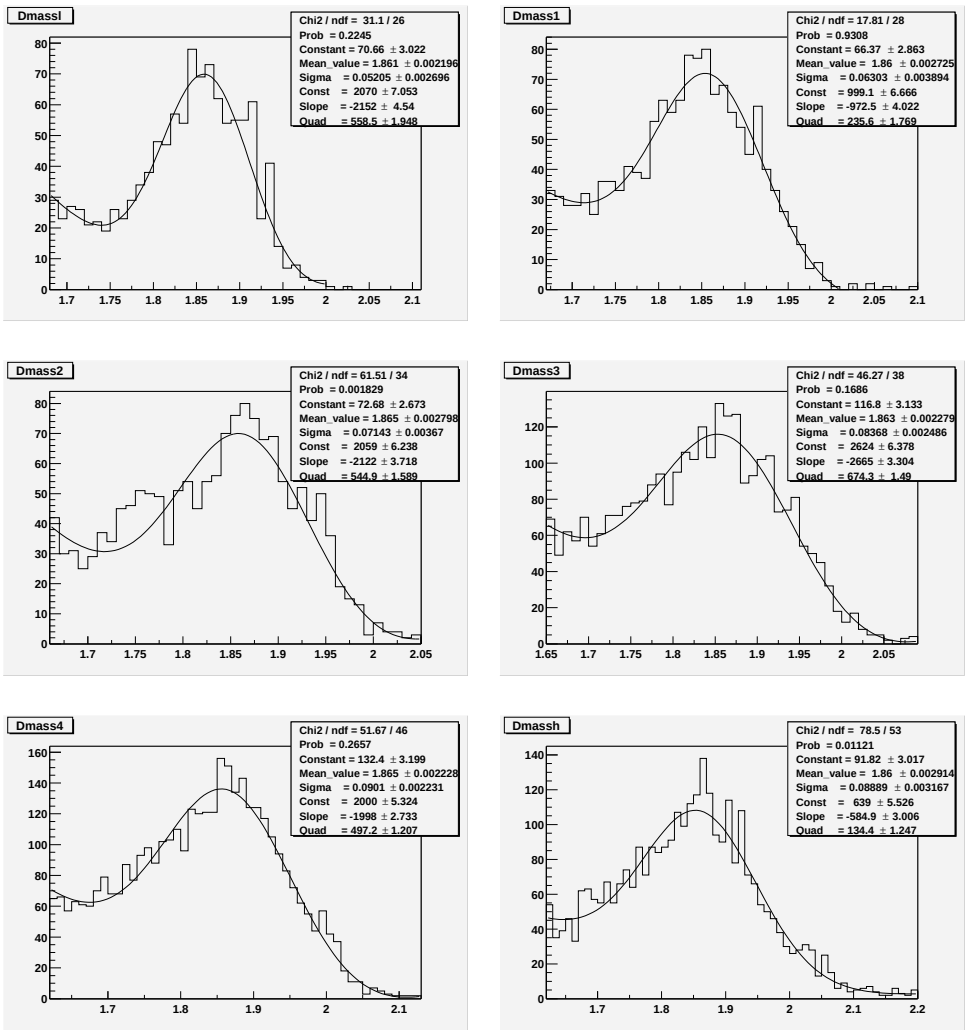

Figure 7.12: $M_{k\pi}$ invariant mass distribution for the 6 P_t ranges, for wrong charge correlation with the bachelor pion from $D^{*\pm}$.

$P_t^{D^\circ}$ range (GeV/c)	M_{Right} (MeV/c^2)	M_{Wrong} (MeV/c^2)	σ_{Right} (MeV/c^2)	σ_{Wrong} (MeV/c^2)	F_R
5.5–6.0	1858.0 ± 0.4	1861 ± 2	9.78 ± 0.30	52.05 ± 2.7	5.32 ± 0.32
6.0–7.0	1859.0 ± 0.4	1860 ± 3	10.61 ± 0.32	63.03 ± 3.9	5.94 ± 0.41
7.0–8.0	1859.0 ± 0.4	1865 ± 3	10.73 ± 0.35	71.43 ± 3.7	6.66 ± 0.41
8.0–9.0	1860.0 ± 0.3	1863 ± 2	10.95 ± 0.24	83.68 ± 2.5	7.64 ± 0.23
9.0–10.0	1860.0 ± 0.3	1865 ± 2	11.81 ± 0.22	90.10 ± 2.2	7.63 ± 0.23
10.0–20.0	1860.0 ± 0.3	1860 ± 3	13.63 ± 0.30	88.89 ± 3.2	6.52 ± 0.28

Table 7.11: Fit results for the right and wrong mass asignements distributions on $D^\circ \to K\pi$ events tagged with $D^{*\pm}$. In the last column $F_R(i) = \frac{\sigma_{Wrong}}{\sigma_{Right}}$ is shown.

the observed dependence with the $P_t^{D^\circ}$ is consistent with what we observe in the simulation. The fitted widths together the measured sigma ratio $(F_R(i)) = \frac{\sigma_{Wrong}}{\sigma_{Right}}$, with i indicating the given P_t bin) are listed in table 7.11.

7.4.2 Signal extraction and background estimates

Applying the selection described in section. 7.4 we obtain the distributions shown in fig. 7.14–7.15. As in $D^{*\pm}$ to unfold the D° momentum dependence, we fit the $D^\circ \to K\pi$ sample in 7 P_t bins starting from 5.5 GeV/c. The superimposed fit from which the number of events in each decay mode is determined, was performed using the following functions and minimizing the χ^2 of the binned histograms:

$$M_{\pi\pi} = N_B \cdot P1_B(m) + N_S \cdot P_{G(m,\mu,\sigma)} \tag{7.7}$$

$$M_{KK} = N_B \cdot P2_B(m) + N_S \cdot P_{G(m,\mu,\sigma)} \tag{7.8}$$

$$M_{K\pi} = N_B \cdot P1_B(m) + N_S \cdot (P_{G(m,\mu,\sigma)} + P_{G(m,\mu,\sigma \cdot F_R(i))}) \tag{7.9}$$

where:

$$
\begin{aligned}
P1_B &= \frac{a0 + a1 \cdot m}{\int_{M_{min}}^{M_{max}} (a0 + a1 \cdot m) dm} \\
P2_B &= \frac{a0 + a1 \cdot m + a2 \cdot m^2}{\int_{M_{min}}^{M_{max}} (a0 + a1 \cdot m + a2 \cdot m^2) dm} \\
P_{G(m,\mu,\sigma)} &= \frac{G(m,\mu,\sigma)}{\int_{M_{min}}^{M_{max}} G(s,\mu,\sigma) ds} \\
G(m,\mu,\sigma) &= \frac{1}{\sqrt{2\pi} \cdot \sigma} e^{-\frac{1}{2}(\frac{m-\mu}{\sigma})^2}
\end{aligned}
$$

where N_S and N_B are the number of signal and background events (in the fitting mass window), $G(x, \mu, \sigma)$ are Gaussian distributions of mean μ and width σ, $F_R(i)$ are the wrong mass assignment over correct mass assignment width ratios for P_t bin i in the $K\pi$ mode as determined from the observation of the D° peak from $D^{*\pm}$ (see table 7.11), M_{min} and M_{max} rapresent the boundary of the fit range.

Since no particle identification is used the areas of the signal peak and the autoreflection peak are constrained to be equal in the whole invariant mass physical range. The fitting method is tested using toy Montecarlo events to check possible bias and if the obtained statistical error on N_S is consistent with the expectations.

5000 Montecarlo experiments, each one with the same statistic of the $D^\circ \to K\pi$ observed signal, are generated according to the $K\pi$ invariant mass distributions in each P_t bin as observed in data. For each experiment we perform the same fit procedure used in data and compare the results to the input parameters used to generate the spectrum. The pull distributions are consistent with unit gaussians, indicating that both fit results and errors are consistent with expectations. The pull distribution for the parameter N_S is shown in figure 7.13, similar distributions holds for the other pulls.

The χ^2 probability for the various fits range from 10% to 80% for the $D^\circ \to K\pi$, and is 3% and 10% for the $D^\circ \to K^+K^-$ and $D^\circ \to \pi^+\pi^-$ fit respectively.
In figure 7.16 the full P_t range $K\pi$ invariant mass distributions is shown with superimposed the sum of the seven fitting functions obtained in the individual P_t

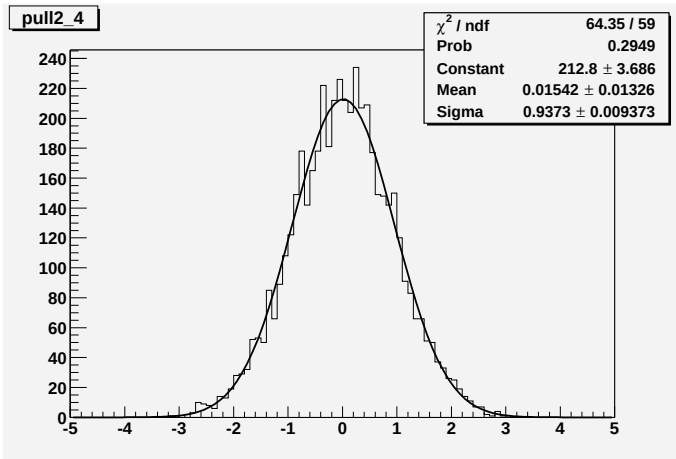

Figure 7.13: Pull distribution for the fitting procedure (paramter N_S). The pull distribution is fitted to a gaussian. Similar plots hold for the other parameters.

Channel	$N_{D^\circ} \pm \sigma_{N_{D^\circ}}$
$D^\circ \to K\pi : P_t \in [5.5 \div 5.75]\ GeV/c$	5380 ± 110
$D^\circ \to K\pi : P_t \in [5.75 \div 6.]\ GeV/c$	5140 ± 100
$D^\circ \to K\pi : P_t \in [6. \div 6.5]\ GeV/c$	8490 ± 130
$D^\circ \to K\pi : P_t \in [6.5 \div 7.]\ GeV/c$	7120 ± 120
$D^\circ \to K\pi : P_t \in [7. \div 8.]\ GeV/c$	10490 ± 140
$D^\circ \to K\pi : P_t \in [8. \div 10.]\ GeV/c$	11000 ± 150
$D^\circ \to K\pi : P_t > 10.\ GeV/c$	8700 ± 150
$D^\circ \to K\pi$ All	56320 ± 340
$D^\circ \to K^+K^-$	5670 ± 180
$D^\circ \to \pi^+\pi^-$	2020 ± 110

Table 7.12: $D^\circ \to K\pi$ results.

bins.

From the fit we derive the total number of observed decays in each mode as reported in table 7.12, where the errors include the correlated background statistical uncertainty.

In the reconstruction of $D^\circ \to K\pi$ candidates both possible mass assignments are kept, so for each P_t bin, the actual number of entries in the histogram does not reflect the real statistical power of the sample due to the presence of duplicate candidates.

For this reason the obtained statistical uncertainties listed in table 7.12 are un-

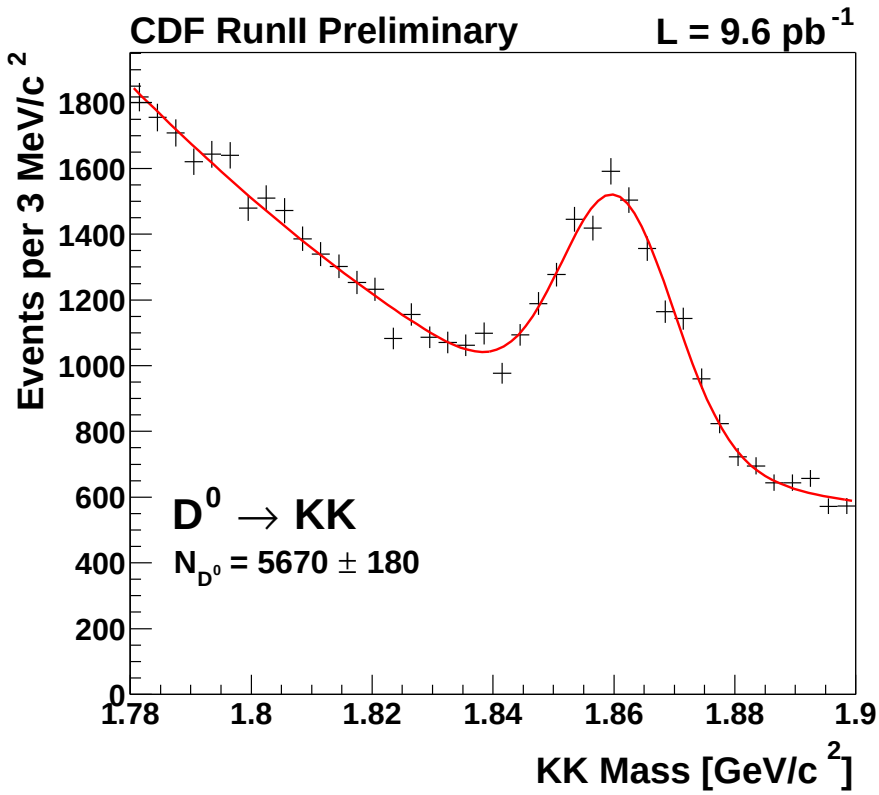

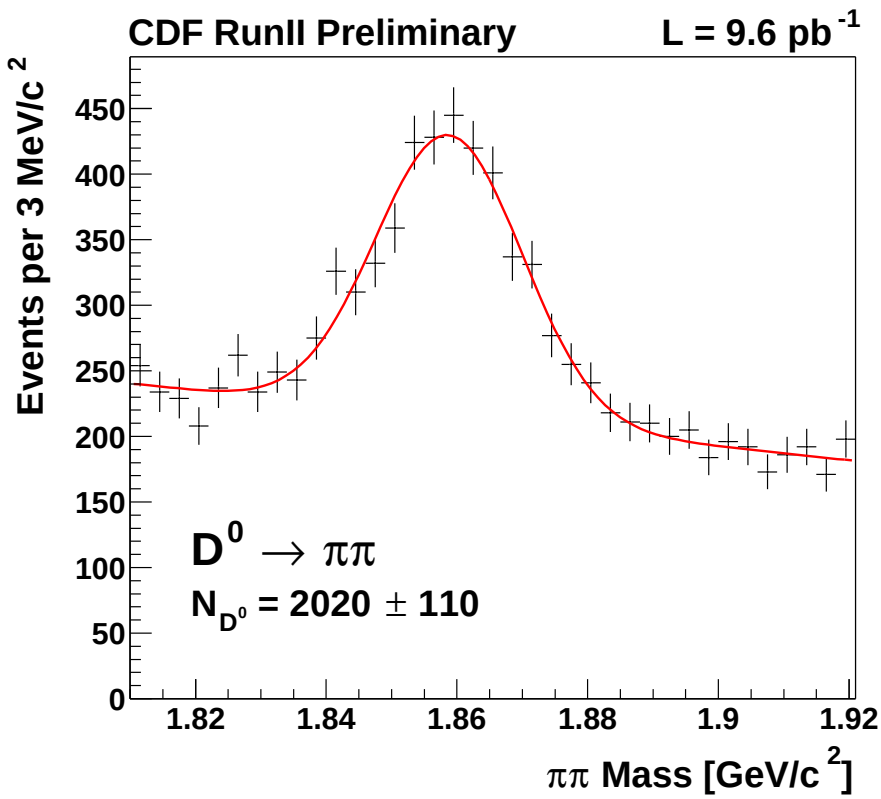

Figure 7.14: Left: $M_{k^+k^-}$ distribution after final selection $D^\circ \to K^+K^-$. See text for fitting function description. Right: $M_{\pi^+\pi^-}$ distribution after final selection $D^\circ \to \pi^+\pi^-$

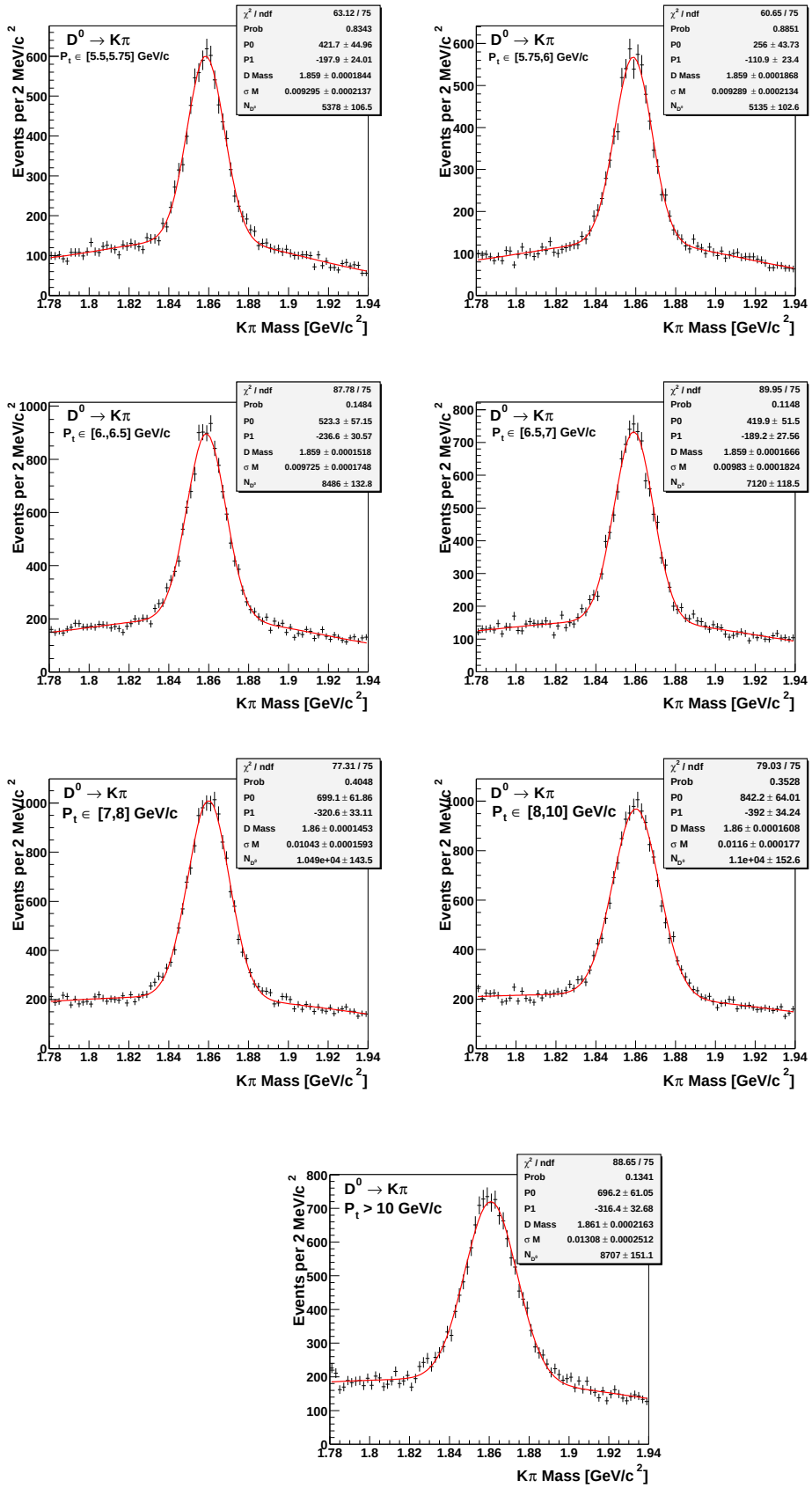

Figure 7.15: $M_{k\pi}$ invariant mass distributions in the 7 P_t bins after final selection for $D^\circ \to K\pi$ (See text for fitting function description).

$P_t(GeV/c)$	$N_{D^\circ} \pm \sigma_{N_{D^\circ}}$	$2 * (N_{D^\circ} \pm \sigma_{N_{D^\circ}})$
$5.50 \div 5.75$	2702 ± 61	5400 ± 120
$5.75 \div 6.00$	2532 ± 73	5060 ± 150
$6.00 \div 6.50$	4264 ± 95	8530 ± 190
$6.50 \div 7.00$	3575 ± 83	7150 ± 170
$7.00 \div 8.00$	5150 ± 100	10300 ± 200
$8.00 \div 10.00$	5560 ± 110	11120 ± 220
> 10.00	4470 ± 110	8940 ± 220
Sum	28250 ± 240	56500 ± 490

Table 7.13: Fit results for the $D^\circ \to K\pi$ signal when the duplicate candidates are removed.

derestimate.

To correct for this problem we perform again the same binned χ^2 fit on a new set of the $D^\circ \to K\pi$ histograms, obtained with the same selection cuts, but choosing randomly only one of the two possible mass assignment ($K^+\pi^-$ or $K^-\pi^+$). We expect then to have half of the previous $D^\circ \to K\pi$ candidates in each histogram, but without double entries in it. In table 7.13 the obtained results are shown. They are compatible with being half of what previously measured. We choose then to correct the statistical uncertainty on the measured $D^\circ \to K\pi$ yield as in table 7.12 using the relative error obtained from this fit. We estimate then the number of $D^\circ \to K\pi$ events to be: $N_{D^\circ \to K\pi} = 56320 \pm 490$ events.

7.4.3 Results

Combining the observed event yield from previous paragraph and the relative acceptance determination from eq. 7.5 and using the expression (7.1) we derive the following partial width ratios:

$$\frac{\Gamma(D^\circ \to K^+K^-)}{\Gamma(D^\circ \to K\pi)} = (11.17 \pm 0.48) \quad \% \tag{7.10}$$

$$\frac{\Gamma(D^\circ \to \pi^+\pi^-)}{\Gamma(D^\circ \to K\pi)} = (3.37 \pm 0.20) \quad \% \tag{7.11}$$

where the errors are statistical only.

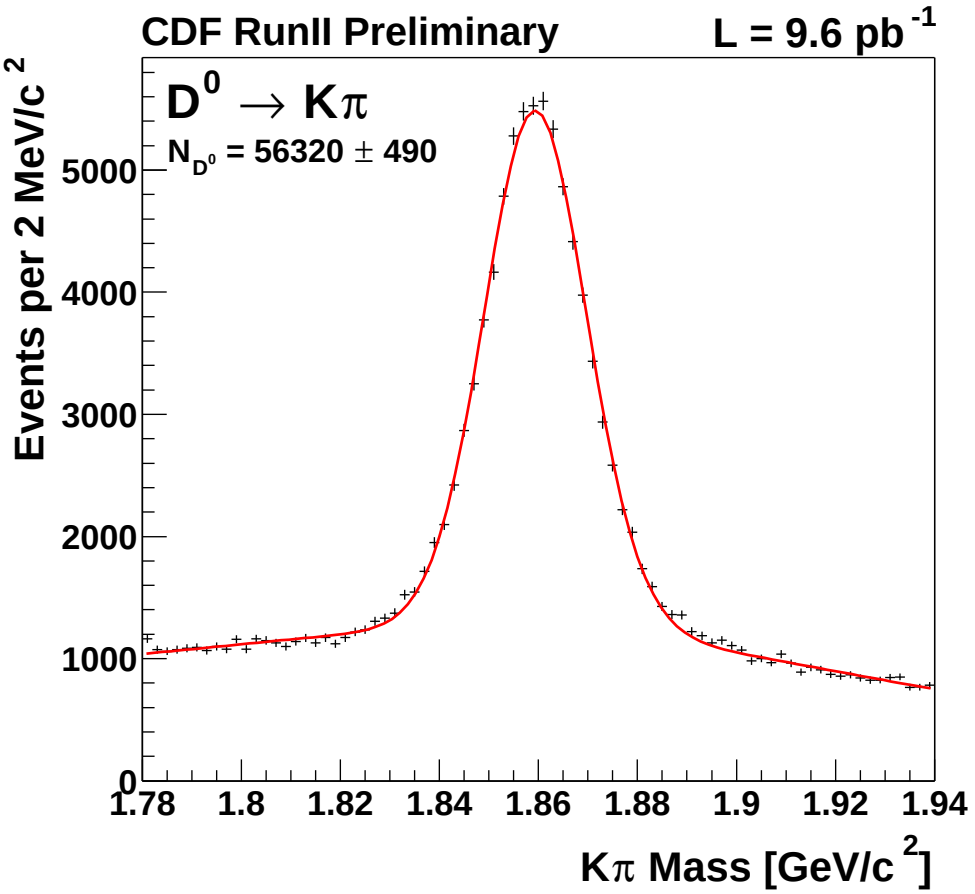

Figure 7.16: $M_{k\pi}$ distribution after final selection. (See text for description of the superimposed function).

7.5 Systematics

In this section we discuss the estimate of systematic uncertainties on the measurement. The final quoted systematic errors are the quadrature sums of systematic uncertainties from the following sources:

- Background fitting functions.
- Model of the autoreflection peak shape.
- Relative acceptance correction, including:
  - Dependence on the production model
  - Parameters of the trigger simulation
  - Effect of nuclear interactions
- Lifetime differences.
- DCS decays contamination.
- Detector alignment and tracking algorithm.

For every effect listed above we estimated associated systematic uncertainty either varying, within reasonable ranges, one or more relevant parameters or comparing the results obtained using different tools. The effects on the measured ratios from charm physics sources like lifetime differences and Double Cabibbo Suppressed decay, were estimated conservatively from the updated 2002 PDG averages. For each source of systematic we express the uncertainty as the maximum variation of the measurement given by each effects.

7.5.1 Background fitting functions

To estimate sources of systematic due to the background model, we tried to vary the forms for the fitting functions used to model the background below the D° peaks. For each channel we considered different fitting functions giving comparable

χ^2 probability for the fit. In particular we changed the order of the polynomial functions or use an exponential function or a combination of the two. The actual maximum variations obtained with this procedure are listed in table 7.14.

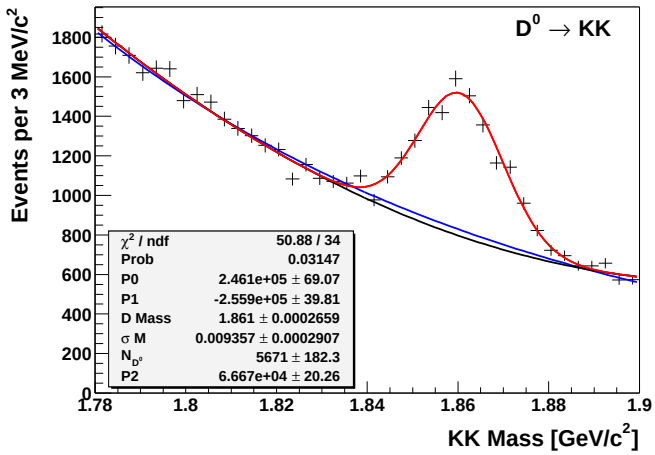

Figure 7.17: M_{KK} distribution with superimposed fitting functions for the polynomial and exponential model of the background.

While we observe small effects, ($O(1.0\ \%)$), for the $K\pi$ and $\pi\pi$ signals, for the KK instead changing the background fitting function from a second order polynomial to an exponential gives a maximum variation of the event yield of about 8 %. In figure 7.17 the KK invariant mass distribution is shown with superimposed the results of the two background fitting functions. This big variation is the result of the lower S/B ratio in the KK signal, the rapidly falling background shape, dominated by misreconstructed $D^\circ \to K\pi\pi^\circ$ and other charm mesons decays, and the impossibility to extend the fitting range on the high mass side due to difficulties in modeling the reflection peak of $D^\circ \to K\pi$ decays. In picture 7.18 the different charm and non charm backgrounds shapes under the D^0 peak in the KK invariant mass plot, are shown.

7.5.2 Autoreflection model

Systematic uncertainties related to the parameterization of the autoreflection peak shape under the $K\pi$ channel was studied in different ways :

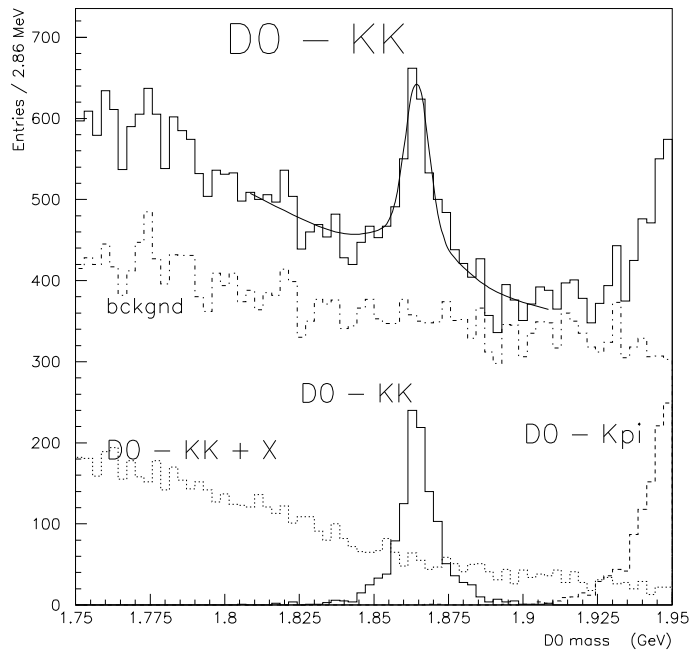

Figure 7.18: M_{KK} distribution with non complete reconstructed $D^0 \to KK + X$, $D^0 \to K\pi$ and combinatorial background contributions. From $b\bar{b}$ montecarlo information.

Function	$D^\circ \to K\pi$	$D^\circ \to \pi^+\pi^-$	$D^\circ \to K^+K^-$
$P1 \to P2$	+0.39%	+0.1%	
$P1 \to EXP$	−0.46%	−1.0%	
$P2 \to P3$			+0.1%
$P2 \to EXP$			+7.8%
Total:	0.85%	1.1%	7.9%

Table 7.14: Maximum variations on the number of D° events obtained changing the background fitting functions.

- Repeating the fitting procedure on $D^\circ \to K\pi$ channel, varying the ratio between wrong and right sign widths measured on the $D^{*\pm}$ sample within $\pm 1\sigma$ (see table 7.11).

  This gives a maximum variation on the measured $D^\circ \to K\pi$ yield of 1.3%.

- Fitting the reflected peak in the $D^\circ \to K\pi$ data, in the same two Gaussian model where the reflected peak width is now a free parameter. This gives a negligible effect on the measured $D^\circ \to K\pi$ yield of 0.036%.

As a further cross-check of the robustness of the reflected peak parameterization, we use the $F_R(i)$ ratio measured on the D° data to fit the D° reconstructed mass from D^* without using the charge correlation with the bachelor pion. The resulting fit is very good, as shown in figure 7.5.2, with a χ^2 probability for the fit of 36 %.

We assign as a systematic uncertainty on our measurement from the reflected peak model the maximum variation observed on our result by changing the fitting procedure as explained above. This turns out to be $\pm 1.3\%$.

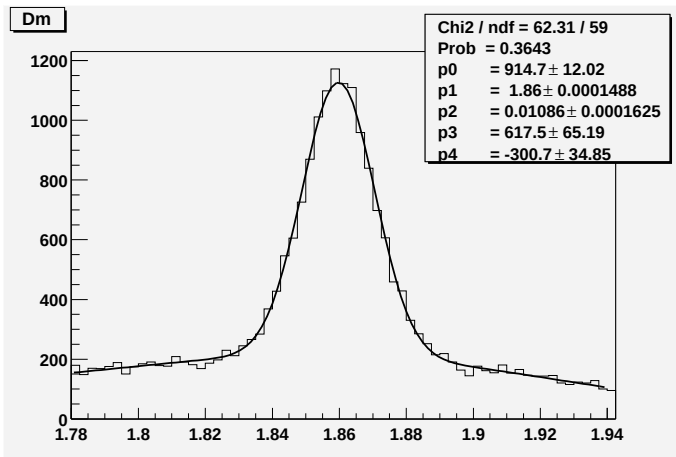

Figure 7.19: Direct and reflected peak D° from D^* events fitted using model parameters measured on D° data.

7.5.3 Lifetime difference and DCS decays

Since we collect our data with a trigger based on the long lifetime of charm mesons the relative collection efficiency could be altered if a different lifetime is assumed for the D_1° and D_2° (the D° mass eigenstates), which would show up as a difference in lifetime for decays into CP eigenstates as K^+K^- or $\pi^+\pi^-$ relative to a mixed CP state as $K^\pm\pi^\mp$. The PDG [44] quote an error on the world average for the observable $2y = \frac{\Gamma_{D_1^\circ} - \Gamma_{D_2^\circ}}{\Gamma}$ of 2.2%. This is indeed measured exactly by comparing lifetime for decays in K^+K^- or $\pi^+\pi^-$ versus $K^\pm\pi^\mp$. We then assign a systematic of 2.2 % on the relative branching ratio measurement assuming a difference in lifetime would propagate linearly in the collection efficiency.

We are ignoring in our calculation the contributions of the doubly Cabibbo sup-

pressed decays of D° mesons (i.e. $D^\circ \to k^+\pi^-$ instead of $D^\circ \to k^-\pi+$). The size of this effect is equal to the ratio of DCS to Cabibbo allowed branching ratios. From the PDG published values we derive a ratio of $0.38 \pm 0.06\%$ and assign as a consequence a systematic error on our measurement for this effect of $\pm 0.4\%$.

7.5.4 Relative acceptance correction

As explained in section 7.2, we used two methods to measure the relative acceptances based on a parametric and full trigger simulation respectively. To the parametric simulation we added the effects of the hadronic interactions in the material and decay in flight, and we switched off as well those effect from the GEANT simulation. The acceptance correction results summary is given in table 7.6 for the two ratios. First two rows refer to svtsim and GenTrig results in which both material and decay effects are taken into account, third and fourth rows refer to svtsim and GenTrig in which both these effects are deconvoluted. As an estimation of systematic on the relative acceptance correction we consider the largest spread between the two simulation approaches in any of the two configurations. In this way we assign a 1.9 % and 2.5 % systematic error for KK and $\pi\pi$ respectively.

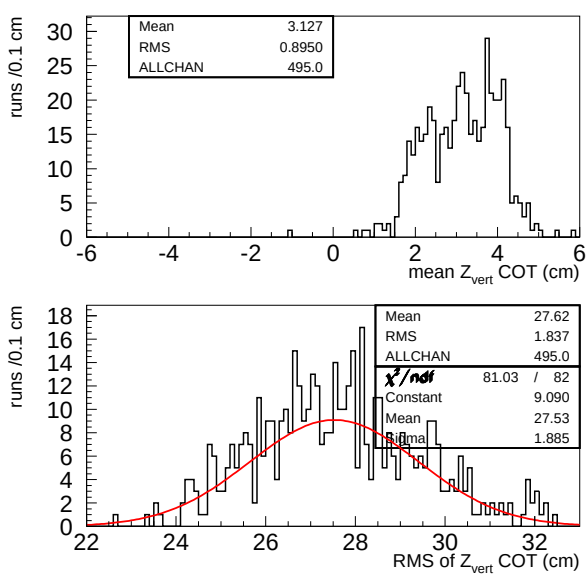

Figure 7.20: Average COT vertex z position for all the runs in the sample and distribution of the RMS of the COT z vertex distribution

We have checked also the dependence of the relative acceptance correction on the mean z position of the luminous beam spot. We averaged over the entire data sample the mean z value of the COT tracks vertices for each run, and this number gives the 3 cm we used in our simulation. The distribution around this value is approximately flat with a 0.9 cm RMS as shown in fig. 7.5.4. We checked that the correction factor has an approximately linear dependence on the assumed mean z value, and quote a systematic from the variation of the mean z of $\pm 1.5cm$. This translates in an additional systematic error of $\pm 0.7\%$ for the $D^\circ \to K^+K^-$ channel and $\pm 0.5\%$ for the $D^\circ \to \pi^+\pi^-$ mode. In the same way we found that uncertainty on the actual beam spot length in z has negligeable effect on the measurement.

As a crosscheck on the accuracy of the material description in GEANT we measured the actual number of D° and $\bar{D}^\circ$ decaying into $K\pi$ in our data. Since the interaction probability is expected to be significantly higher for K^- than for K^+ we anticipate a slightly lower number of D° than $\bar{D}^\circ$. This is in fact confirmed since in our sample we find $N_{D^\circ} = 27790 \pm 250$ and $N_{\bar{D}^\circ} = 28560 \pm 250$, corresponding to a relative difference of $(2.7 \pm 1.2)\%$. From the single particle interaction probabilities of table 7.5 we predict this difference to be $(2.2 \pm 0.3)\%$. Despite this number agree within errors, we conservatively assign a systematics on the material description in GEANT of 0.5%.

7.5.5 Production model

In order to evaluate the effect of the production model for charmed mesons, we changed the P_T spectra at the input of the parametric simulation of the trigger (GenTrig). We evaluated again the relative acceptance on the three decay modes and its effect on the relative BR. We tested the hypotesys of a flat P_T distribution between 4 and 20 GeV, and uniform in $|\eta| < 1.2$, using FakeEvent.

The difference on the relative BR is 1.8 % for both KK and $\pi\pi$. We expect uncertainty on the P_T spectra used for the relative acceptance correction to be significantly smaller than its difference with a flat distribution as it can be seen in

figure 7.5.5 in which $p_T(D^0)$ spectra after trigger in montecarlo and data. In the data the clean D^0 mesons selection from D^* decays was used. Plot in figure 7.5.5 shows discrepancies of the order of 10 %, the value of systematic estimated for this effect at the time beeing is then quite conservative.

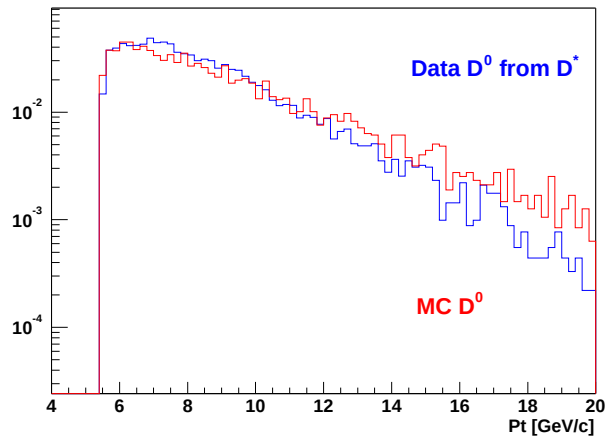

Figure 7.21: Transverse momentum for D^0 meson after trigger in the data in blue where D^0 are selected from the decay chain $D^* \to D^0\pi$. In red the spectrum from MC after trigger simulation with the production model adopted.

Charm mesons are produced at Tevatron both directly ("prompt") and from secondary decays of b hadrons. The relative yield of secondary to prompt D° (f_B) in the Two Track Trigger has been estimated in [43] (see section 6.5), where a range of $15\% < f_B < 24\%$ is quoted. In order to estimate the effect on the relative collection efficiency from seconday D° from secondary decays we simulated $B_u \to D^\circ\pi\pi\pi$ and $B_u \to D^\circ\pi$ letting the D° decay in one of the three modes under consideration. We verified that in this case the trigger and reconstruction efficiency ratios are 1.02 for the kk case and 0.96 for $\pi\pi$. We thus assign as a systematic the full size of the expected effect assuming a 15% b fraction in our sample.

7.5.6 Tracking

Most of the tracking uncertainties are expected to cancel in the ratios. We nevertheless tried to estimate residual effects changing alignment and tracking algorithm. In particular we retracked the whole sample using OutsideIn tracks with the latest

alignment table that was not available at the time of production. OutsideIn algorithm doesn't take into account stereo coordinates points in pattern recognition. The effect on the ratios is found to be well within the statistical fluctuations, and we assign conservatively the residual difference, 0.4% and 1.7% for the $D^\circ \to K\pi$ and $D^\circ \to \pi^+\pi^-$ mode respectively, as an additional systematics.

7.5.7 Systematics Summary

Table 7.15 summarizes individual systematic uncertainties, and the overall systematic we assign to our measurement taken as the as the quadrature sum of the each contribution. Other effects are expected to be of minor importance because of expected cancellation in the ratio.

Systematic source	$\frac{\Gamma(D^\circ \to K^+K^-)}{\Gamma(D^\circ \to K\pi)}$	$\frac{\Gamma(D^\circ \to \pi^+\pi^-)}{\Gamma(D^\circ \to K\pi)}$
Background Subtraction	7.9%	1.4%
Reflected peak model	1.3%	1.3%
Trigger Simulation	1.9%	2.5%
beam spot mean z	0.7%	0.5%
material description	0.5%	0.5%
Lifetime Difference	2.2%	2.2%
DCS Decays	0.4%	0.4%
Input D° spectra	1.8%	1.8%
b/c ratios	1.1%	–
Tracking	0.4%	1.7%
TOTAL:	8.8%	4.6%

Table 7.15: Systematic errors in %.

7.6 Summary

Even with limited integrated luminosity CDF is able to measure this ratio of branching ratios with accuracy comparable to the best experiments. Considering the esti-

mate of systematics reported earlier, we obtain:

$$\frac{\Gamma(D^\circ \to K^+K^-)}{\Gamma(D^\circ \to K\pi)} = 11.17 \pm 0.48(stat) \pm 0.98(syst)\ \%$$
$$\frac{\Gamma(D^\circ \to \pi^+\pi^-)}{\Gamma(D^\circ \to K\pi)} = 3.37 \pm 0.20(stat) \pm 0.16(syst)\ \%$$

This measurement compare favourably with the best single experiment existing up to now. The published CLEO II [50] measurement is in fact:

$$\frac{\Gamma(D^\circ \to K^+K^-)}{\Gamma(D^\circ \to K\pi)} = 10.40 \pm 0.33(stat) \pm 0.27(syst)\ \%$$
$$\frac{\Gamma(D^\circ \to \pi^+\pi^-)}{\Gamma(D^\circ \to K\pi)} = 3.51 \pm 0.16(stat) \pm 0.17(syst)\ \%$$

obtained with a similar technique at the Υ_{4S} with $\approx\ 10\ fb^{-1}$ integrated luminosity. This measurement is already limited at least in the KK mode by systematics related to background modeling. With more data we will be able to use more effectively the sample of D° tagged from $D^{*\pm}$ where a better S/N is reachable. Other development may include particle identification with dE/dX, a more detailed study of the background shape from MC including physical models for the $K\pi\pi^0$ and $K\pi$ reflections, and more careful examination of some of the systematics that were for the time being very conservatively assigned.

Chapter 8

Perspectives for HF physics and CPV in the hadronic sample

8.1 Introduction

As a consequence of the studies based on the two track hadronic trigger data sample, presented in this thesis, here we want to give some HF physics potential for CDF in the next future. As already poited out in introductory chapter 2, the selection of topics that are presented here is faraway to be exhaustive of the full charm and beauty physics CDF plans. Complete presentations of CDF preliminary results on HF physics at summer 2002 conferences, can be found in [45] [46] [47]. For a detailed review on CDF B physics perspectives consult [48].

Lepton trigger sample based measurements are not threated as well as other HF topics that can be addressed in the hadronic trigger itself. This choice has been done in relation to the D mesons reconstruction in the SVT sample, and in particular to the relative branching fraction measurement for Cabibbo suppressed $D^0 \to KK, \pi\pi$ decays, as seen in chapter 7.

The CDF charm physics potentials, presented in section 8.2 in terms of charmed mesons yields, are as promising as unexpected. The proposals for $D^0 - \bar{D}^0$ mixing measurement via lifetime difference, and for the direct CP violation search in $D^0 \to KK, \pi\pi$ decays, see sections 8.3 and 8.4, has been directly suggested from encouraging preliminary results on relative BR for these channels presented in previous chapter. The CDF collaboration expects to have preliminary results on these

CPV measurements very soon.

The off-line reconstruction techniques developped for D mesons have been used as first step for $B \to DX$ decays analisys as described in section 6.6 for the $B^{\pm} \to D^0\pi^{\pm}$.

The $B_s - \bar{B}_s$ mixing measurement perspectives, in section 8.5, which are based on fully hadronic B_s decays to $D_s\pi$, $D_s\pi\pi\pi$ will benefit from the D_s selection criteria optimization as well as from the SVT trigger simulation studies commissioned with charm physics sample.

The method to extract CKM angle γ from $B \to hh$ decays presented in section 8.6 has its experimentally crucial issue in the $B \to K\pi, \pi\pi$ components possibly desentangled through particle identification with dE/dx. At this purpose high statistics $D^0 \to hh$ sample will be a unique test ground for the experimental technique necessary to perform this measurement.

8.2 CDF charm physics potential

As illustrated in chapter 2, Charm sector offers many chances to study heavy mesons physics, CP violation and new physics searches. In particular since charm is an up-type quark, loop diagrams do not involve heavy top quark like in the B sector, resulting in small SM amplitudes for mixing and CP violation. New physics contribution may enhance this amplitudes and leave distinct signatures in the charm sector.

From the experimental point of view charmed mesons fully reconstructuble decays present BR of the order of 10 % with respect to order 10^{-5}% in the B sector, moreover about one third of D^0 mesons comes from a $D^{*+} \to D^0\pi^+$ strong interaction decay thus allowing the tag of D^0 flavour at production with an efficiency close to 100 %. This is a major lever arm for mixing and CP studies in the charm sector.

In the past charm physics has been done at fixed target experiments whereas, in recent years, at the B factories running at $Y(4s)$ getting free charm from continuum or off-resonance runs. In the near future CLEO experiment will dedicate a special 3 year run for charm physics putting CESR accelerator at Ψ resonances over D meson pairs production thresholds. This will allow the exploitation of the coerence of initial state for tagging and an excellent way to measure absolute BR from precise knowledge of production process.

In CDF run II, the Silicon Vertex Tracker designed to trigger on displaced vertices, can collect high statistic B samples in fully hadronic final states. As it is evident from measurements and SVT studies presented in this thesis, this trigger contains also a large sample of fully reconstructable charm hadrons. Charm physics has not yet been done at hadron $p\bar{p}$ colliders but we think that the huge statistic now accessible at CDF, give the opportunity to CDF to make first class measurements in several intersting channels in this sector.

Relying on the charmed mesons yelds observed up to know and on very recent optimization of SVT trigger we give, in the following section, a rough estimates of

the charm event yield prospects for run II.

A selection of charm physics topics, previously introduced in the firsts chapters, are then reviewed.

8.2.1 Charm yields

Following exactly the selection of events used in chapters 6 and 7, we require one of the opposite charge track pairs in the D meson decay final state to match an SVT-like track pair. This allows to rely on precise way to measure trigger efficiency for such events, as demonstrated for example in the measure of chapter 7. The charmed mesons fully reconstructed decays in the SVT trigger are shown in the plots of figure 8.1. The yields measured on this data sample on an integrated luminosity of around 10 pb^{-1} together with extrapolations to 100 pb^{-1} which CDF foresee to collect by spring 2003 and to 2 fb^{-1} the total run IIa integrated luminosity, are in table 8.1.

	$1pb^{-1}$	$100pb^{-1}$	$2fb^{-1}$
$D^0 \to K\pi$	5867	586700	11.74 M
$D^* \to D^0\pi$	1605	160500	3.21 M
$D^0 \to KK$	590	59000	1.18 M
$D^0 \to \pi\pi$	210	21000	0.42 M
$D^\pm \to K\pi\pi$	4485	448500	8.97 M
$D_s \to \Phi\pi$	204	20400	0.41 M

Table 8.1: Charmed yields in the SVT trigger at present conditions per pb^{-1} in the first column. Extrapolations for 100 pb^{-1} and 2 fb^{-1} in the last two columns.

We can remark large yields also in suppressed channels like $\pi\pi$, moreover around one third of the D^0 mesons comes from a D^* thus allowing flavour tag. The event yelds in table 8.1 are measured on data from SVT running conditions corresponding to february-may 2002 data tacking period on which the analysis presented in this thesis are based. As shown in section 7.2, on this data, SVT efficiency per track ϵ_{SVT} was $\sim 80\%$, measured on indipendent sample of J/Ψ. Very recent optimizations of SVT patterns, rise this value up to $\sim 90\%$; this have the effect of an enhancement of trigger efficiency to those channels. If we consider a D^0 decay to

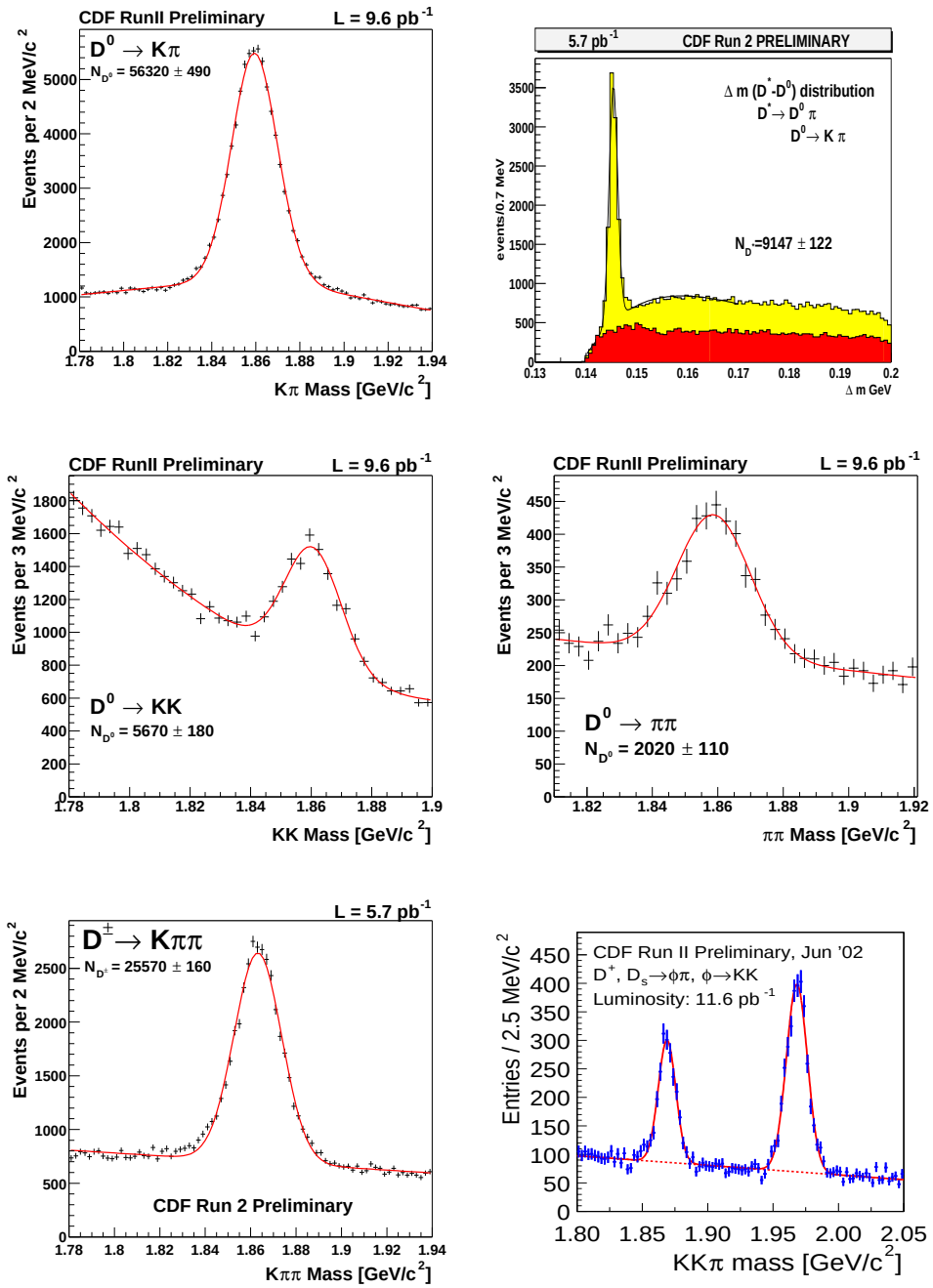

Figure 8.1: Charmed mesons yields in the SVT trigger. The used integrated luminosity is reported in each plot as well as the number of signal events extracted from fits. For the lower right plot the results are: $N_{D_s} = 2360 \pm 70$ and $N_{D^+} = 1350 \pm 60$.

two charged particles we can roughly estimate the enhancement factor for ϵ_{SVT} to be $(0.9)^2/(0.8)^2 \simeq 1.5$ if we assume the two tracks being uncorrelated. The yield of D^0 decays to $K\pi$ has been measured on few runs after this recent SVT optimization and it is consistent to be a factor 1.5 higher than that reported in table 8.1. We assume that the yields reported here are then quite conservatives as well as the reach for charm measurement discussed in the following.

With the first few tenths of pb^{-1} it will be possible to measure the charm production cross section in $p\bar{p}$ collisions at $\sqrt{s} = 1.96$ TeV, exploiting the channels in figure 8.1 from SVT trigger selection. This will be the first time that charm cross section is measured down to low p_T, in analogous way of $b\bar{b}$ (see 1) cross section measurement it is of secure interest for QCD calculations power in heavy flavour production processes. It is also possible, even if with lower efficiency, to reconstruct the two charmed mesons or hadrons in the event from the hadronization of $c\bar{c}$ pair. Intersting studies of angular correlations between c and $\bar{c}$ will then be performed.

8.2.2 Limits in charm physics for CDF

What essentially limits the charm physics potential of CDF is the knowledge of production processes for charm at $p\bar{p}$ interactions. Moreover, initial $c\bar{c}$ state is not coherent one as in e^+e^- $c\bar{c}$ resonances, thus it doesn't allow flavour tag at production; there is also the fact that a fraction of charm production comes from B physics as described in section 6.5. Secondary charm, produced from B decays, will be produced at a significative distance from primary vertex giving a bias to proper time measurement. This will limit charm lifetime measurements.

The production processes limited knowledge, instead, turn on to the impossibility for CDF to perform absolute Branching fractions measurements for charmed mesons and hadrons.

By the way as it is demonstrated by the measurement of relative D^0 Branching fractions presented in 7, relative measurements in which production processes drop out can be done with high accuracy with the CDF detector.

Another limitation is constituted by the particle identification not excellent at CDF; at high $p_T > 2$ GeV the K/π separation power, based on dE/dx, will be of 1.3 σ, see 5 for details. For $p_T < 1.6$ GeV particle identification will rely on both TOF and dE/dx. Using this particle identification power on a statistical basis, one can anyway have a significative background reduction as shown in the case of the TOF PID in the $\Phi \to KK$ analysis discussed in chapter 5. In all charm analyses, backgrounds from charmed reflections in the final state which is under study, can be important like in the $D^0 \to KK$ seen in section 7.5.

Despite that, all measurements involving D^0 production from D^* are very possible for CDF, they present, as already underlined, the advantage of initial flavour tag and also the advantage of being very clean channels as a consequence of the thight kinematical cut on the Q value of D^* decay, which powerfully rejects background.

8.3 $D^0 - \bar{D}^0$ mixing

In section2.3 we defined the quantities x, y and r in the $D^0 - \bar{D}^0$ system, which are relevant parameters to describe the D^0 mesons mixing. There are essentially three ways to measure D^0 mixing:

- Measure the lifetime difference between CP-mixed state like $D^0 \to K^-\pi^+$ and CP eigenstates like $D^0 \to KK, \pi\pi$. This is a measure of $y = \Delta\Gamma/2\Gamma$.

- Measure wrong sign (WS) hadronic decays like $D^0 \to K^+\pi^-$. In this case we will have contamination by doubly cabibbo suppressed decays without mixing.

- Measure wrong sign semileptonic decays such as $D^0 \to K^+\mu^-\bar{\nu_\mu}$. This is sensitive to $r = \frac{1}{2}(x^2 + y^2)$.

We will focus on the first method in which hadronic D^0 decays are involved and on which it is possible to exploit SVT trigger capabilities to have large yields of those channels.

8.3.1 Mixing through lifetime difference

The decay of D^0 to CP eigenstates may be used to measure the quantity:

$$y = \frac{\Delta\Gamma}{\Gamma} = \frac{\Gamma_{CP+} - \Gamma_{CP-}}{\Gamma_{CP+} + \Gamma_{CP-}} \tag{8.1}$$

In the limit that CP is conserved in charm decays, and considering that even CP eigenstates like KK or $\pi\pi$ are experimentally more accessible, we can write 8.1 in term of lifetimes as:

$$y = \frac{\bar{\tau}}{\tau_{CP+}} - 1 \tag{8.2}$$

where $\bar{\tau}$ is the lifetime of a CP neutral state like $K\pi$ and τ_{CP+} that of KK or $\pi\pi$ states; thus to measure y we simply need the ratio of $D^0 \to K\pi$ to $D^0 \to KK, \pi\pi$ lifetimes. So far, this strategy has been applied by several experiments, the present world mean value for the quantity $2y = \Delta\Gamma/\Gamma$ is $(-0.003 \pm 0.022)\%$ [44]. All measurements are at few percent level of accuracy and still consistent with zero. As an example the best measure up to now has been performed by the Belle experiment, the result is $y = (-0.5 \pm 1.0 \pm 0.8)\%$ [49]. This measure rely on a sample of around 18k $D^0 \to KK$ and 214k $D^0 \to K\pi$ decays reconstructed on a sample of 23 fb^{-1} of integrated luminosity at a center of mass energy 60 MeV below th $Y(4s)$ resonance. If we focus on the statistical error on y, which is 1 % for Belle and compare with CDF yield for $D^0 \to KK$ decays evaluated in table 8.1 which gives for 100 pb^{-1} of integrated luminosity by CDF at least 3 times larger statistic, thus reducing statistical error by a factor near to 2. The trend of collected D^0, between CDF and the B factories as a function of Luminosity will be in the future even better for CDF. Actually only a small fraction of total luminosity integrated by the B factories experiments ($\sim 200 fb^{-1}/exp.$) will be taken off-resonance.

Among the possible systematic errors sources in the measurement, the SVT trigger bias on lifetimes and the particle identification capabilities could limit the precision on y. While first order systematic effects cancel in the lifetime ratio in 8.2, improvements to the SVT trigger simulation consequences of the study presented in chapter 7 suggest that it will be in principle possible to control higher order effects

under the desired precision. Particle identification applied on the final state particles of the D^0 decays, used by Belle in order to minimize background and reflections, can be by-passed by requiring that the D^0 under study comes from a $D^* \to D^0\pi_b$ decay. This condition on the D^0 production, gives the correct particle assignement in the $K\pi$ final state of the D^0 meson through the correlation between the charges of the bachelor pion π_b and that of the pion from D^0 decays. This correlation has been exploited in chapter 7. The request of the decay chain from D^* will also have the advantage of reducing significantly the long lived background in lifetime distributions from D^0 mesons coming from B. This can be obtained by requiring that the reconstructed D^* meson is produced at primary interaction vertex.

The price will be payed in terms of statistics: we recall that around one third of D^0 mesons comes from D^*. Nevertheless in 100 pb^{-1} integrated luminosity by CDF, a sample of $D^0 \to KK$ (see 8.1) comparable in statistics with the Belle one, can be exploited at CDF. In 2 fb^{-1} CDF could measure y at the permille level.

8.4 CP violation in $D^0 \to hh$ decays

Given the size of the CKM matrix elements involved CP violation in D^0 mixing is of order $\eta\lambda^5 \sim 10^{-4}$, while direct CP violation in charm decays is of order $\eta\lambda^4 \sim 10^{-3}$. Direct CP violation can be observed as an asymmetry A_{CP} in the partial widths between $D \to f$ and its CP conjugate mode $\bar{D} \to \bar{f}$:

$$A_{CP} = \frac{\Gamma(D \to f) - \Gamma(\bar{D} \to \bar{f})}{\Gamma(D \to f) + \Gamma(\bar{D} \to \bar{f})} \tag{8.3}$$

Non zero values of A_{CP} occur when there are at least two contributions with different weak and strong phases to the decay amplitude. For the CP conjugate process, the weak phase change sign, but the strong phase does not. Relative weak phases can only be obtained in Cabibbo suppressed decays, via the interference between spectator and penguin amplitudes. In addition, D decays are known to be affected by significant strong final state interactions (FSI), which can enhance certain transition amplitudes and suppress others, thus modifying the magnitude of observable CP

asymmetries. A_{CP} are expected to be $< 10^{-3}$ in Cabibbo suppressed decays like $D^0 \to KK, \pi\pi$.

Chosing KK or $\pi\pi$ to be the D^0 final state, the experimental strategy to measure A_{CP} in those modes, rely on the $D^0(\bar{D}^0)$ flavour tag at production by requiring that it comes from the decay of a charged D^* to $D^{*\pm} \to D^0\pi^\pm$.

In this case a complication to the measurement of A_{CP} can come from a possible production asymmetry between D and anti-D mesons, so CP asymmetry can be measured relative to a Cabibbo favored mode (on which A_{CP} is expected to be zero) to get rid of this effect.

At CDF the total charm production is expected to be symmetric ($p\bar{p}$) interactions, nevertheless the relative measure with respect to favored modes can help in controlling detector acceptance asymmetries. In particular the most delicate point is the significative charge asymmetry in the CDF tracking system, particularly for low p_T of the tracks. In the $D^{*\pm} \to D^0\pi^\pm$ decay the bachelor π from the D^* have relatively slow momentum and will be affected by tracking charge asymmetries thus turning in a systematic for A_{CP}. The selection of D^0 mesons to KK and $\pi\pi$ will be performed exactly in the same way exposed in chapter 7, requiring for the two tracks to match SVT requirements.

The best measurement up to now of A_{CP} in $D^0 \to KK, \pi\pi$ decays comes from CLEO experiment, the results are consistent with zero in both channels and are respectively: $A_{CP}(KK) = (0.0 \pm 2.2 \pm 0.8)\%$ [50] and $A_{CP}(\pi\pi) = (1.9 \pm 3.2 \pm 0.8)\%$[50]. This numbers are based on around 3k $D^0 \to KK$ and 1.1k $D^0 \to \pi\pi$ decays tagged with D^*. Results from Babar and Belle based on significatively bigger sample are expected soon.

The CDF sample in those D^0 decays with D^* tag, can be conservatively prospected from table 8.1 for an integrated luminosity of 100 pb^{-1}, probably availiable in summer 2003, to be around 16k events for KK and 6k events for $\pi\pi$. With this sample we expect to have measurements of $A_{CP}(KK, \pi\pi)$ with factor of 2 better statistical error than CLEO result. It is important to notice, as a proof of CDF potential on

this measurement, that on the same $D^0 \to KK, \pi\pi$ reported above CLEO measures relative BR between these decays and the Cabibbo favored $D^0 \to K\pi$ with the same level of precision reached in the measurement presented in this thesis, see chapter 7 for details.

8.5 B_s^0 oscillations, Δm_s

The probability that a B_s meson decays at proper time t in the same state, or has mixed to the $\bar{B}_s$ state is given by:

$$P_{unmix}(t) = \frac{1}{2}(1 + cos\Delta m_s t) \tag{8.4}$$
$$P_{mix}(t) = \frac{1}{2}(1 - cos\Delta m_s t)$$

where the mixing frequency, Δm_s, is the mass difference between the heavy and light CP eigenstates (see chapter 2). The canonical B_s mixing analysis, in which oscillations are observed and the mixing frequency Δm_s is measured, proceeds as follows. The B_s meson flavour at the time of its decay is determined by reconstructing a flavour specific final state. The proper time, $t = m_{B_s}L/pc$, at which the decay occurred is determined by measuring the decay length L and the B_s momentum p. Finally, the production flavour must be tagged in order to classify the event as being mixed or unmixed at the time of its decay. Oscillations manifest in a time dependence of the mixed asymmetry:

$$A_{mix}(t) = \frac{N_{mix}(t) - N_{unmix}(t)}{N_{mix}(t) + N_{unmix}(t)} \tag{8.5}$$

In practice, the production flavour will be correctly tagged with a probability P_{tag} which is significantly smaller than unity. The form of the measurable mixed asymmetry is then:

$$A_{mix}(t) = -Dcos\Delta m_s t \tag{8.6}$$

with the dilution D related to P_{tag} by $D = 2P_{tag}$. The mixing frequency is determined for example by fitting the measured asymmetry to a function of this form. So far, Bs oscillations have not been observed experimentally, and the lower limit on $x_s = \Delta m_s \tau_{B_s}$ is above 15. This means that B_s mesons oscillate much more rapidly than B_d mesons. The rapidity of the B_s oscillation implies a significant difference in the experimental requirements for the two analyses. The limiting factor in B_d mixing analyses is solely the effective tagging efficiency, which is equivalent to the

effective statistics. In Bs mixing measurements the resolution of the proper time becomes another very critical issue. To determine the proper time, not only the positions of primary and secondary vertices have to be measured precisely, but also the measurement of the B_s momentum is crucial.

Therefore, it is desirable to have fully exclusive final states such as $B_s \to D_s\pi$ with $D_s \to \Phi\pi, \Phi \to KK$. Semileptonic B_s decays have the intrinsic disadvantage that the neutrino momentum is undetected. In Run I CDF reconstructed 220 and 125 B_s semileptonic decay events with fully reconstructed $D_s \to \Phi\pi$ and $D_s \to K^*K$ channels, respectively, in low p_T ($> 8GeV/c$) inclusive lepton (e and μ) trigger samples. An additional 600 semileptonic B_s decays were used, reconstructed in the $D_s \to \Phi X+$ track channel. Those events were part of the dilepton ($\mu\mu$ and $e\mu$) trigger samples, where the second lepton was used for the B flavour tag. The best limit on x_s was given by the dilepton trigger dataset.

In Run II much more statistics will be available using the lepton trigger, the lepton trigger plus one secondary vertex track and the all hadronic SVT trigger. From the event yield estimates we expect 40k events in the lepton plus displaced track and 75k events in the all hadronic trigger. In the following, the measurement of B_s mixing using hadronic decays is discussed.

Sensitivity to Δm_s

The mixing frequency can be determined by calculating, for example, a maximum likelihood function derived from the measured and expected asymmetries and minimizing this function with respect to Δm_s. The significance of an observation of mixing is quantified in terms of the depth of this minimum compared with the second deepest minimum or some asymptotic value at large Δm_s. To a good approximation, the average significance is given as:

$$Sig(\Delta m_s) = \sqrt{N\epsilon D^2} e^{-(\Delta m_s \sigma_t)^2/2} \sqrt{\frac{S}{S+B}} \tag{8.7}$$

where $N = S$ is the number of reconstructed B_s signal events, S/B is the signal-to-background ratio, ϵ is the efficiency for applying the flavour tag with associated

dilution D, and σ_t is the average resolution with which the proper time is measured. This definition is essentially the same as what would be used to define $n\sigma$ confidence intervals for a Gaussian probability density function. Given estimates for these parameters, the limit of sensitivity is defined as the maximal value of Δm_s for which the significance is above a specified value.

Flavour tagging

In Run II, a Time-of-Flight detector will provide CDF with the ability to distinguish kaons from pions at the 2σ level below a momentum of about 1.6 GeV/c as described in detail in chapter 5. This allows two new flavour tags to be implemented which rely on the charge of kaons identified in the event to tag the production flavour of the B_s. The total effective dilution ϵD^2 expected in Run II will be 11.3 % (for details see chapter 5).

B_s Mixing with Hadronic Decays

The fully hadronic event sample is particularly important for B_s mixing analyses since the fully reconstructed decays $B_s \to D_s\pi, D_s\pi\pi\pi$ have excellent proper time resolution, much smaller than the expected period of oscillation. The proper time of a B_s decay is calculated from the measured decay length, and the reconstructed B_s momentum. The uncertainty on the proper time is then simply given by:

$$\sigma_t = t\sqrt{(\frac{\sigma_L}{L})^2 + (\frac{\sigma_P}{P})^2} \tag{8.8}$$

To resolve the rapid oscillations of the B_s it is generally required that this resolution not be significantly larger than the period of oscillation.

For partially reconstructed semileptonic Bs decays, the uncertainty in the momentum is the limiting factor in the mixing analyses. However, for the fully reconstructed Bs decays obtained using the $XFT + SVT$ triggers, the momentum uncertainty will be less than 0.4 %.

This does not contribute significantly to the overall proper time resolution and has been ignored in the projections described below.

Background

Till now, no hadron collider experiment has operated with a displaced track based trigger. Hence before data tacking the level of backgrounds to be expected in the B_s sample was uncertain. With the integrated Luminosity collected up to now in the SVT trigger ($\sim 10pb^{-1}$), the level of baackground in a full reconstructed hadroic decay of B_S meson can be guessed from $B^{\pm} \to D^0\pi^{\pm}$ decay reconstructed in the same trigger sample, presented in section 6.6. Even if the topology of this $B^{\pm}$ decay is slightly different, a S/B ratio of more than 1 seems to be achievable.

Since S/B ratio is one of the parameters that affects Δm_s measurement in the projection given in the following, performed before CDF data tacking start, S/B is allowed to range between pessimistic $1:2$ and $2:1$.

Projection

For the projected sensitivity to x_s a detector and trigger simulation has been used with the same tools described in section 6.2. This simulation of trigger gives a combined L1 and L2 trigger efficiencies for B_s decays to $D_s\pi$ and $D_s\pi\pi\pi$ with the above indicated D_s decay channel, are respectively 0.27 % and 0.11 %. The BR for the B_s to this channels have been extrapolated from similar B_d^0 decays. $BR(B_s \to D_s\pi) = (3.0 \pm 0.4)10^{-3}$ and $BR(B_s \to D_s\pi\pi\pi) = (8.0 \pm 2.5)10^{-3}$ have been used. For the D_s BR we used PDG 2000 values. In this two modes around 38000/channel (total of 7500) B_s decays are expected to be collected in total run II integrated Luminosity of 2 fb^{-1}.

The proper time resolution estimated from 8.8 gives $\sigma_t = 0.045ps$ exploiting the presence of near to the beam pipe silicon layer $L00$ (without $L00$ $\sigma_t = 0.060ps$). Effective dilution ϵD^2 is taken to be 11.3 % as explained above and in chapter 5.

The results of this projection are shown in figure 8.2; the sensitivity to B_s oscillation is expressed in terms of that to the adimensional mixing parameter $x_s = \Delta m_s \tau_{B_s}$, as a function of number of signal events collected (left) and of S/B ratio (right). From figure 8.2 it is clear that even with a little fraction of total inte-

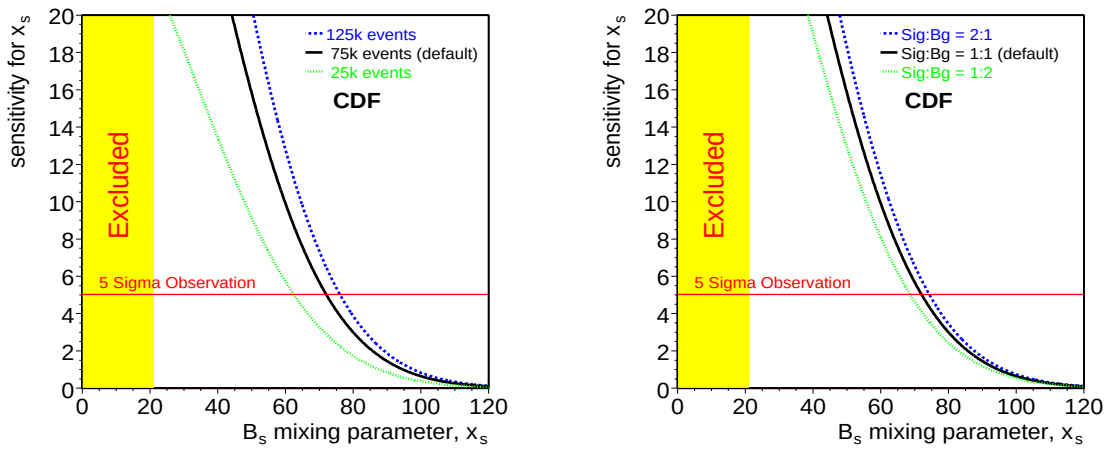

Figure 8.2: Sensitivity for x_s as a function of B_s signal events (left) and of S/B ratio (right). Shaded area is the combined world limit at summer 2000.

grated luminosity of run II, CDF will achieve a precision measurement of B_s mixing frequency with a 5 σ significance up to x_s value of 60 in the worst scenario given in figure 8.2. Translating into Δm_s, precedent value correspond to $\Delta m_s < 40ps^{-1}$ (up to 50 in the best case). If we take into account that very recent combined LEP limits on B_s oscillation frequency are $\Delta m_s > 19ps^{-1}$ at 95 % CL ($x_s > 29$) and that analysis of the unitarity triangle bound x_s to be in the range between 22 and 30.8 at 95 % CL [51], hence the CDF reach for Δm_s is well above expected Standard Model and experimental fits bounds.

8.6 $B_d, B_s \to hh$ decays

Two body charmless decays of B mesons are of particular interest for the CDF B physics program. Recalling what described in detail in chapters 1 and 4, the SVT displaced vertex trigger selection is based on two L2 trigger paths, the multibody path and the 2 body path. This last has been especially designed and implemented in order to select in an optimized way $B_d, B_s \to hh$ decays. This decays are actually an excellent system to study many interesting physics topics related to CKM elements determination, we think in particular to α and γ.

We breefly discuss here the two-body B decays in terms of first signals in the SVT

trigger and of physics perspectives, essentially to underline the tight experimental connection from the trigger and the reconstruction points of view, with the charmed mesons decays threated in this thesis.

The decay $B^0 \to \pi\pi$ has been in the recent years at the center of several approaches to extract CKM angle α. It is now clear that this is limited by the so-called "penguin pollution". These B decays can infact proceed through both "tree" and "penguin" diagrams and experimental BR amplitudes for $B^0 \to \pi\pi$ and $B^0 \to K\pi$ demonstrates that penguin contribution is non negligible. Methods to desentangle penguin and tree contributions, for example that proposed by Gronau and London [52], has been proposed. This method makes use of Isospin relations between 2-pions modes for B mesons at this purpose, but it relies on very small and experimentally difficult BR determination like BR($B^0 \to \pi^0\pi^0$) which is of the order of 10^{-6}. The B factories are doing several attempts in this field.

At CDF we will exploit the fact that at $p\bar{p}$ interaction we will have access in the same time to B_d and B_s mesons decays. In particular using $B^0 \to K\pi$, $B^0 \to \pi\pi$, the corresponding modes $B_s \to KK$, $B_s \to K\pi$ and the $SU(3)$ flavour symmetry it is possible, as proposed by Fleisher [53], to extract information on CKM angle γ.

Based on measured B^0 BR and the production fractions $f_d(f_s)$ for $B_d(B_s)$, and tacking into account $SU(3)$ breaking factors, we expect an event ratio of:

$$(B^0 \to K\pi) : (B^0 \to \pi\pi) : (B_s \to KK) : (B_s \to \pi K) = 4 : 1 : 2 : 0.5 \qquad (8.9)$$

Using the latest measurement of the B cross section $\sigma_B = (3.35 \pm 0.46 \pm 0.50)\mu$b, CDF expects between 5000 and 9000 fully reconstructed $B^0 \to \pi^+\pi^-$ decays collected with the SVT trigger in 2 fb^{-1} total integrated luminosity of run IIa. To study the reach in γ we assume 5000 $B^0 \to \pi\pi$, 20000 $B^0 \to K\pi$, 10000 $B_s \to KK$ and 2500 $B_s \to \pi K$. Following Fleisher the CKM angle γ can be extracted from the measured time dependent asymmetries in $B^0 \to \pi^+\pi^-$ and in $B_s \to KK$ which are of the form:

$$A_{CP} = A_{CP}^{dir} cos\Delta mt + A_{CP}^{mix} sin\Delta mt \qquad (8.10)$$

Supposing that U-spin symmetry subgroup of $SU(3)_F$ is valid, it directly relates $B^0 \to \pi\pi$ with $B_s \to KK$ and the strong phase $\theta(\theta')$ and the penguin to tree ratio $d(d')$ are related by:

$$\theta' = \theta; \;\; d' = d\frac{1-\lambda^2}{\lambda^2} \tag{8.11}$$

where λ is the sine of the Cabibbo angle. Hence the two time dependent A_{CP} can be expressed in terms of 4 variables: γ, β, d and θ. Using the high precision measurement of β from $B \to J/PsiK_s^0$ it is then possible to extract γ, see [48] for details on the assumptions.

From the experimental point of view, a crucial point in this measurement will be desentangling of $\pi\pi$, πK, $K\pi$ and KK final states in the two-body invariant mass distribution obtained after kinematical selections on the tracks. In the B flavour tagged sample that will be used, the big difference in oscillation frequencies between B_d and B_s systems will be of great help in separating this two components. The $B^0 \to \pi\pi$ peak will anyway be covered by the 4 times bigger background from $B^0 \to K\pi$. Given the fact that tracks are selected to be SVT tracks they will have $p_T > 2$ GeV, thus only particle identification information will come from dE/dx measurement performed by COT drift chamber as discussed in chapter 5. A separation of 1.3 σ between kaons and pions in this momentum range is expected from dE/dx.

At this purpose the dE/dx statistical separation power will be measured and studied in detail with the $D^* \to D^0\pi, D^0 \to K\pi$ sample. Actually D^0 meson sample used all through this thesis, have very similar kinematic characteristics to those expected in $B \to hh$, and being a very high statistics sample, it will be the ideal system to test dE/dx separation power. The D^* tag will be used as highly efficient apriori K vs π mass assignement knowledge. $B \to hh$ analysis will then benefit of SVT trigger simulation studies and optimizations that have been performed for charm, see chapters 6 and 7.

Conclusions

The analysis presented in this thesis are first strong evidences for both the new SVT trigger ability in the on-line selection of heavy flavour hadronic decays in $p\bar{p}$ interactions, and for the CDF potentials, in particular on charm physics.

The result of the relative BR measurements for D^0 mesons two-body decays presented in chapter 7 is already at this stage competitive with best single measurement obtained so far by the CLEO experiment [50]. Analysis and reconstruction tools developed for charm mesons are tuned and validated at a very refined level and constitute the framework for B mesons analysis in hadronic final states like $B_s \to D_s\pi$. SVT simulation has been tested on data and will be a fundamental tool for the analysis based on HF hadronic decays from this trigger sample.

As prospected in sections 8.3 and 8.4, competitive measurements and limits on D^0 mixing and direct CP violation in D^0 mesons decays will be possible with the luminosity integrated in the next few months of CDF operations. This measurements, proposed as consequence of the encouraging results given in this thesis, are main goals for CDF collaboration in a short time schedule, I am thus involved in this analysis at present.

The on-going validation study of particle identification with dE/dx on the D^*-tagged D^0 mesons sample will have strong impact on the $B \to hh$ components deconvolution, as seen in section 8.6. The matching of PID with dE/dx with the PID at low p_T given by the Time-of-Flight, studied on the high statistic sample of charmed mesons will allow a precise knowledge of CDF PID global performance in terms of statistical power and efficiency; flavour tagging techniques and especially

those based on Kaon tagging will benefit of this study. This point is crucial, as underlined in section 8.5 for B_s mixing frequency measurement at CDF in the next period.

Bibliography

[1] The CDF Collaboration, F. Abe et al., Phys. Rev. D 50, 5550 (1994).

[2] M. Mangano, P. Nason and G. Ridolfi , Nucl. Phys. B373, 295 (1992).

[3] H. U. Bengtsson and T. Sjostrand, Comp. Phys. Comm. 46, 43 (1987).

[4] G. Marchesini and B.R Webber, Nucl. Phys. B310, 461 (1988); Nucl. Phys. B330, 261 (1988);
I. G. Knowles, Nucl. Phys. B310, 571 (1988);
G. Abbiendi, et al., Comp. Phys. Comm. 67, 465 (1992).

[5] The CDF Collaboration, T. Affolder et al., Phys. Rev. Lett. 84, 1663 (2000).

[6] D. Abbaneo et al., Combined results on b hadron production rates, lifetimes, oscillations and semileptonic decays, hep-ex/0009052.

[7] R.D. Field, The Sources of b quarks at the Tevatron and their correlations, Phys.Rev.D65:094006,2002, hep-ph/0201112

[8] N. Cabibbo, Phys. Rev. Lett. 10, 1963 (531).
M.Kobayashi and K.Maskawa, Prog. Theor. Phys. 49, 1973 (652).

[9] L.Wolfenstein, Phys. Rev. Lett. 51, 1983 (1945).

[10] Belle Collaboration, An improved measurement of mixing induced CP violation in the neutral B meson system, ICHEP 2002, contributed talk.
Babar Collaboration, Measurement of the CP violating asymmetry amplitude $\sin 2\beta$ with the Babar detector, FPCP 2002, contributed talk.

[11] C. Bernard, Nucl. Phys. Proc. Suppl. 94, 159 (2001).

[12] A. A. Petrov, Phys. Rev. D 56, 1685 (1997).

[13] A. Datta and M. Khambakhar, Z. Phys. C, 27 (1985) 515.

[14] J. F. Donoghue, E. Golowich, B. Holstein and J. Trampetic, Phys. Rev. D 33, 179 (1986).

[15] H. Georgi, Phys. Lett. B, 297 (1992) 353; T. Ohl et al, Nucl. Phys. B 403, 605 (1993);
I. I. Bigi and N. G. Uraltsev, hep-ph/0005089;
E. Golowich and A. A. Petrov, Phys. Lett. B 427, 172 (1998) [hep-ph/9802291].

[16] S. Bergmann, Y. Grossman, Z. Ligeti, Y. Nir and A. A. Petrov, Phys. Lett. B 486, 418 (2000) [hep-ph/0005181].

[17] A. F. Falk, Y. Nir and A. A. Petrov, J. High Energy Phys. 9912, 019 (1999) [hep- ph/9911369].

[18] F. Buccella, M. Lusignoli and A. Pugliese, Phys. Lett. B 379, 249 (1996).

[19] E. Golowich and A. A. Petrov, Phys. Lett. B 427, 172 (1998) [hep-ph/9802291];
E. Golowich, Phys. Rev. D 24, 676 (1981).

[20] M. Golden and B. Grinstein, Phys. Lett. B 222, 501 (1989).

[21] A. B. Smith for the CLEO Collaboration in Proceedings of the Fourth International Conference on B Physics CP Violation, hep-ex/0104008.

[22] FOCUS Collaboration, J. M. Link et al., Phys. Lett. B 491, 232 (2000) [hep-ex/0005037];
CLEO Collaboration, G. Bonvicini et al., Phys. Rev. D 63, 071101 (2001) [hep-ex/0012054].

[23] F. Buccella et al., hep-ph/9212253 (1992).

[24] Run II Handbook, Fermilab Beam Division

[25] CDF Run II, Technical Design Report, CDF Collaboration, FERMILAB-PUB-96/390-E, Nov 1996

[26] Beyond the Baseline, Proposal for October 1998 PAC meeting, the CDF II collaboration.

[27] S.R.Amendolia et al., IEEE Trans. Nucl. Sci. 39, 795-797 (1992).

[28] W.Ashmanskas et al., Performance of the CDF Online Silicon Vertex Tracker, IEEE Nucl. Sci. 2001, FERMILAB-CONF-02/035-E

[29] C.Paus et al., Design and performances test of the CDF Time-of-Flight system, NIM A461 (2001) 579-581.

[30] C.Grozis et al., The time of flight detector at CDF, Nucl.Phys.Proc.Suppl., 47 (2001) 344-347.

[31] C.Chen et al., Front end electronics for the CDFII time of flight system, IEEE NSS Symposium 2001.

[32] G.Gomez et al., On-line calibration of the CDF II Time-of-Flight detector, CDF Note 6050

[33] M.Jones, Initial performance studies of the CDF II Time-of-Flight detector, CDF Note 5930

[34] A.Cerri, S. De Cecco, S.Giagu, M.Rescigno, S.Vallecorsa, D0 Studies Using SVT Special Runs, CDF Note 5771.

[35] A. Belloni, R. Carosi, S. Donati, I. Fiori, G. Punzi, First look at Two-Track trigger data, CDF Note 5758.

[36] S.Giagu et al., CDF Note in preparation.

[37] P.Sphicas, A B-BBAR MONTE CARLO GENERATOR, CDF Note 2655; K.Anikeev et al., Description of Bgenerator II, CDF Note 5092

[38] I.Furic, Ch.Paus, J.Seely, Track Trigger Simulation at the Generator Level in RunII, CDF Note 5348

[39] T.Nakaya, Measurement of the $D^{*+}(2010)$ production cross section in p pbar collisions at $\sqrt{s} = 1.8$ TeV, CDF Note 5025.

[40] M.Cacciari,M.Greco,S.Rolli,A.Tanzini, Charmed Mesons Fragmentations Functions, hep-ph/9608213

[41] A.Cerri,M.Rescigno CDF Note in preparation.

[42] S.Giagu et al., CDF Note in preparation.

[43] C. Chen, R. Oldeman, J. Kroll, A Method to Measure the Direct and Secondary Charm Fraction in Two Track Data, CDF Note 5996.

[44] Particle Data Group, The European Physical Journal D66 (2002).

[45] S. De Cecco for the CDF Coll., Beauty and Charm physics at CDF, first results and perspectives, Pub. Proc. HCP 2002, Karlsruhe Germany.

[46] A.Cerri for the CDF Coll., First CDF II Heavy Flavor Physics Results with the Silicon Vertex Trigger, Pub. Proc. ICHEP 2002, Amsterdam, The Netherlands.

[47] C.Paus for the CDF Coll., Heavy Quark Production at CDF, Pub. Proc. ICHEP 2002, Amsterdam, The Netherlands.

[48] K. Anikeev, B PHYSICS AT THE TEVATRON: RUN II AND BEYOND, hep-ph/0201071

[49] K.Abe et al., A measurement of lifetime difference in D^0 meson decays. hep-ex/0111026, 2001.

[50] E.Csorna et al., lifetime differences, direct CP violation and partial widths in D^0 meson decays to KK and $\pi\pi$, hep-ex/0111024, 2001

[51] F.Parodi, P.Roudeau, A Stocchi, Nuovo Cimento 112, 833 (1999).

[52] M.Gronau, D.London, Phys. Rev. Lett. 65 3381 (1990)

[53] R.Fleisher, Phys. Lett. B 459 306 (1999)